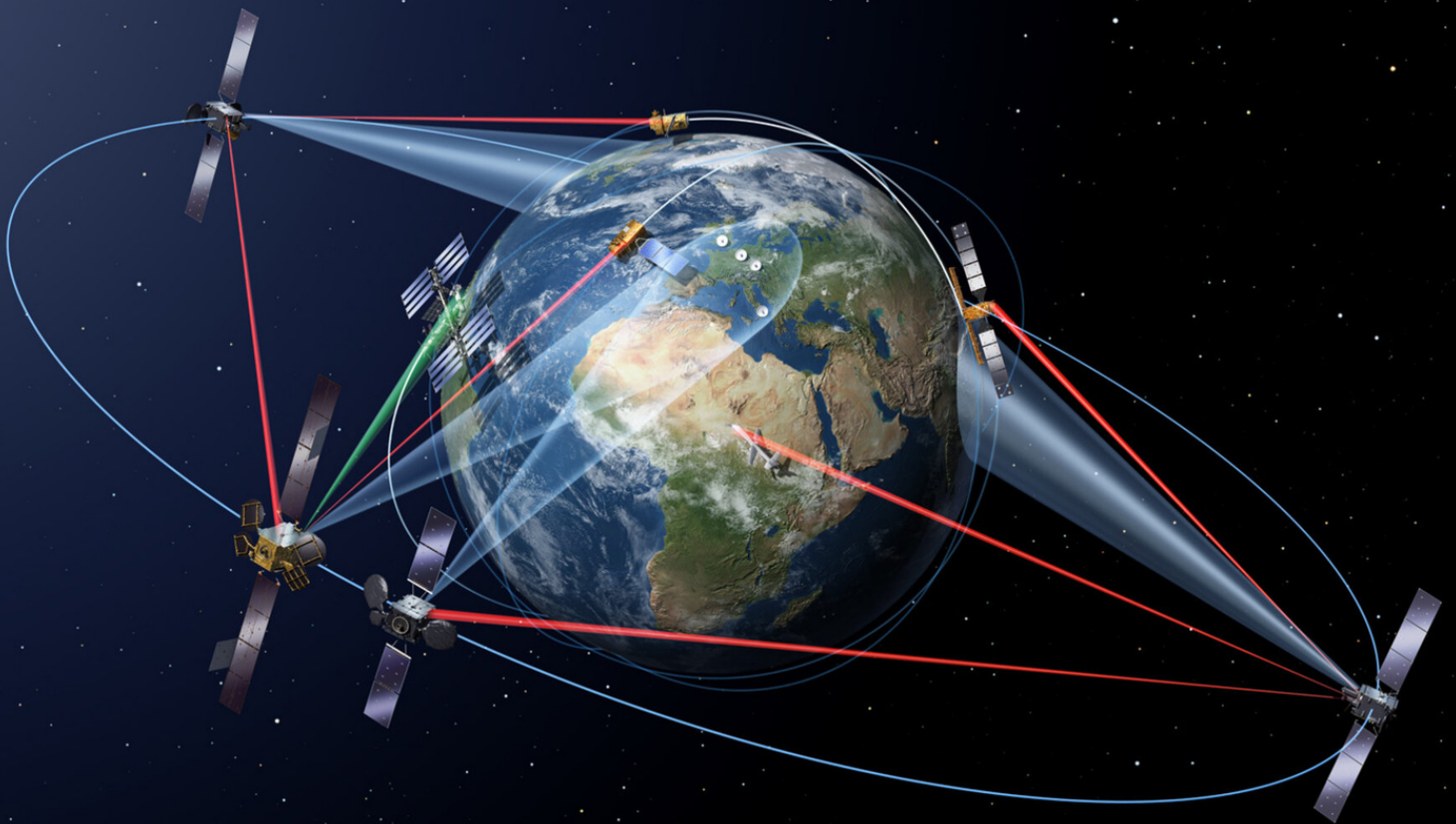


# Precise Relative Navigation in Medium Earth Orbits with Global Navigation Satellite Systems and Intersatellite Links for Black Hole Imaging

María Salas Lasala



# Precise Relative Navigation in Medium Earth Orbits with Global Navigation Satellite Systems and Intersatellite Links for Black Hole Imaging

by

María Salas Lasala

in partial fulfillment of the requirements for the degree of

**Master of Sciences**  
in Aerospace Engineering

at Delft University of Technology,  
to be defended publicly on Monday July 10, 2023 at 10:00 AM

Supervisor: Dr. Ir. J.A.A. van den IJssel

Thesis committee: Dr. Ir. J.A.A. van den IJssel TU Delft  
Dr. Ir. P.N.A.M. Visser TU Delft  
Dr. Ir. A.A. Verhagen TU Delft  
Dr. J. Fernández Sánchez GMV

Student: María Salas Lasala (5146496)

Cover image: Property of the European Space Agency (ESA)



# Acknowledgements

Approximately two years ago, I received the news of my acceptance into Delft University of Technology to pursue the Spaceflight Track of the Master's programme in Aerospace Engineering. These past two years have been an incredible journey, one that unfolded across two cities: Delft and Madrid. Along the way, I have been fortunate to learn invaluable lessons and share wonderful moments with incredible people. This thesis represents the culmination of this two-year journey.

As I look back, I am filled with gratitude for the countless people who have offered their unwavering help and support throughout this journey. Firstly, I would like to express my deepest appreciation to Jaime Fernández Sánchez, my supervisor at GMV, for entrusting me with the topic of this thesis. Without his guidance and support, none of this would have been possible. Secondly, I extend my profound gratitude to Jose van den IJssel, my supervisor at TU Delft, for embarking on this project with me. Her continuous support has been crucial for my success, and her kind words have provided me with constant encouragement.

I am truly grateful for the opportunity to conduct my thesis at GMV, in the Precise Orbit Determination department. From the moment I joined, I was warmly welcomed and supported by the entire team. I want to give my sincere thanks to Javier, Carlos, Marc, Miguel, Luning, Sonia, Eva, and Olek for making me grow professionally and personally. I would like to express my special appreciation to Javier Berzosa for his patience and assistance.

To all my friends, I am forever grateful for your presence in my life. To the 'Monte Carlo Fan Club' — Isabel, Juan, Héctor, Mateo, and Jorge — thank you for being by my side during this journey. We have almost made it. I am incredibly proud of all of you. I would also like to thank the rest of the Spanish gang for being like my family during this time. In particular, I want to extend a special thanks to Isabel for being an essential source of support throughout these past two years. Delft would not have been the same without you. Moreover, I cannot forget about my friends from Madrid. To Blanca, for always being there to listen and cheer me up. To Marina, for being my partner in crime. To Gianfranco, because his belief in me has been a constant source of motivation. And to Merche, thank you for your unconditional friendship throughout all these years.

Finally, to my family. To my parents, Antonio and Pilar, for your unlimited support, encouragement, and love. You have always been there to remind me that life is much more than a university degree. To my sister Lucía, for being the light of my life. And to my grandmother, for always taking care of me, *eres mi ángel de la guarda*.

*María Salas Lasala  
Madrid, June 2023*

# Abstract

The Event Horizon Telescope (EHT) is a global array of telescopes that employs Very Long Baseline Interferometry (VLBI) techniques to image the event horizon of black holes. To overcome the limitations of ground-based telescopes, this thesis explores the mission concept involving a two-satellite constellation of space-borne telescopes deployed in Medium Earth Orbit (MEO). The attainment of high-resolution black hole images requires extremely precise baseline determination at the few millimetre level. To address this challenge, each satellite within the constellation is equipped with two hemispherical Global Navigation Satellite System (GNSS) receivers and an optical Intersatellite Link (ISL) for relative navigation. This study aims to assess the feasibility of achieving highly accurate relative positioning within the constellation, particularly considering the large intersatellite distances involved.

The methodology employed in this simulation study encompasses several steps. Initially, the satellite orbits are estimated independently for each satellite using GNSS observations. Following this, the orbit of one of the satellites is held fixed as a reference, while the orbit of the other satellite is re-estimated by incorporating the ISL observations. To enhance the accuracy of the orbit estimation, integer GNSS ambiguity resolution is implemented in the precise orbit determination process. The simulated data incorporates an extensive set of realistic error sources, including thermal noise, instrumental delays, clock biases, errors in the GNSS ephemerides and clocks, uncertainties in the geopotential and solar radiation pressure models, and white noise in the ISL observations.

The results highlight the importance of integer ambiguity resolution in meeting the stringent relative navigation requirements of the mission. The analysis also reveals that the ISL observations primarily improve the baseline estimation along the direction of the link itself. However, in the direction of the black hole, the impact of ISL observations is minimal, indicating that the ISL does not significantly contribute to meeting the specific relative navigation requirements. Furthermore, the study identifies that large intersatellite distances lead to degraded relative orbit accuracy due to fewer shared errors between the two satellites. As a consequence, the objective of achieving a 3.5 mm (3-sigma) one-dimensional relative position accuracy along the black hole direction is not met, with the obtained results showing a 3-sigma of 8.29 mm. To tackle this, it is recommended to focus on mitigating the most prominent error sources, namely uncertainties in the dynamical model and errors in the GNSS orbits and clocks. Other alternatives, such as a network processing scheme, could also be investigated in the future to overcome this challenge.

# Contents

<b>Acknowledgements</b>	<b>i</b>
<b>Abstract</b>	<b>ii</b>
<b>List of Acronyms</b>	<b>vi</b>
<b>List of Symbols</b>	<b>ix</b>
<b>1 Introduction</b>	<b>1</b>
1.1 Problem Description	2
1.2 EHI Constellation Properties	3
1.2.1 Orbital Configuration and Pointing Strategy	3
1.2.2 Satellite Macro-Modeling	4
1.2.3 Sensor Suite	6
1.2.4 Baseline Dynamics	7
1.2.5 Mission Time Frame	7
1.3 Review of Previous Studies	8
1.3.1 Key Outcomes of Previous Studies	8
1.3.2 Revisiting Assumptions of Previous Studies	9
1.4 Research Proposal	10
1.4.1 Research Objective	10
1.4.2 Research Questions	10
1.5 Thesis Outline	11
<b>2 Global Navigation Satellite Systems</b>	<b>12</b>
2.1 GNSS Constellations	12
2.1.1 GPS	12
2.1.2 Galileo	13
2.1.3 GLONASS	13
2.1.4 BeiDou	13
2.2 GNSS Observables	13
2.2.1 Pseudorange	13
2.2.2 Carrier Phase	14
2.3 GNSS Signal Delays	15
2.3.1 Relativistic Effects	15
2.3.2 Tropospheric Delay	15
2.3.3 Ionospheric Delay	15
2.3.4 Carrier Phase Wind-Up	16
2.3.5 Antenna Phase Centre Offset and Variation	16
2.3.6 Instrumental Delays	16
2.3.7 Multipath Errors	16
2.3.8 Receiver Thermal Noise	17
2.4 Combinations of Observations	17
2.4.1 Narrow- and Wide-Lane Combinations	17
2.4.2 Ionospheric-Free Combination	18
2.4.3 Single Differences	18
2.5 Relative Navigation with GNSS	19
2.5.1 Swarm Constellation	19
2.5.2 CHAMP/GRACE Constellation	20
<b>3 Intersatellite Links</b>	<b>21</b>
3.1 ISL Technology Description	21
3.1.1 Radio Frequency or Optical Intersatellite Links	21
3.1.2 Optical ISL Ranging Techniques	22
3.1.3 One-Way or Two-Way Ranging	22
3.1.4 Optical ISL Architecture	23

3.2	ISL Observation Model . . . . .	23
3.2.1	ISL Observable . . . . .	24
3.2.2	ISL Error Sources . . . . .	24
3.3	Relative Navigation with ISL . . . . .	25
3.3.1	GRACE-FO . . . . .	26
3.3.2	LISA and LISA Pathfinder . . . . .	26
3.3.3	BeiDou-3 . . . . .	27
3.3.4	Kepler System . . . . .	27
<b>4</b>	<b>Precise Orbit Determination</b>	<b>29</b>
4.1	Reference Frames . . . . .	29
4.1.1	GCRF Reference Frame . . . . .	29
4.1.2	QSW Reference Frame . . . . .	30
4.1.3	ISL-SGRA Reference Frame . . . . .	30
4.2	Dynamic Model . . . . .	31
4.2.1	Gravity of the Earth . . . . .	32
4.2.2	Third-Body Forces . . . . .	32
4.2.3	Solid, Ocean and Pole Tides . . . . .	33
4.2.4	Solar Radiation Pressure . . . . .	33
4.2.4.1	Box-Wing Model . . . . .	33
4.2.4.2	ECOM . . . . .	34
4.2.4.3	Modified ECOM: ECOM-SGRA . . . . .	35
4.2.5	Earth Albedo and Infrared Radiation . . . . .	36
4.2.6	Relativistic Effects . . . . .	36
4.2.7	Dynamical Model Uncertainties . . . . .	36
4.3	Integer Ambiguity Resolution . . . . .	37
4.3.1	Integer Ambiguity Resolution Strategies . . . . .	37
4.3.2	Integer Ambiguity Resolution Algorithm . . . . .	38
4.4	POD Software . . . . .	39
<b>5</b>	<b>Methodology</b>	<b>41</b>
5.1	Generation of Reference Orbits and Clocks . . . . .	42
5.1.1	Generation of Reference Orbits . . . . .	42
5.1.1.1	Generation of Reference GNSS Orbits . . . . .	42
5.1.1.2	Generation of Reference EHI Orbits . . . . .	43
5.1.2	Generation of Reference Clocks . . . . .	43
5.2	Generation of Observations . . . . .	44
5.2.1	Generation of GNSS Observations . . . . .	44
5.2.1.1	Generation of GNSS Ambiguity . . . . .	45
5.2.1.2	Generation of GNSS Instrumental Delays . . . . .	45
5.2.2	Generation of ISL Observations . . . . .	46
5.3	Generation of Error Sources . . . . .	46
5.3.1	Clock Biases . . . . .	46
5.3.1.1	GNSS Clock Biases . . . . .	47
5.3.1.2	EHI Clock Biases . . . . .	47
5.3.2	Thermal Noise . . . . .	48
5.3.3	Instrumental Delays . . . . .	52
5.3.4	Errors in the GNSS Orbits and Clocks . . . . .	53
5.3.5	Laser Noise . . . . .	57
5.3.6	Uncertainties in the Geopotential Model . . . . .	57
5.3.7	Uncertainties in the Solar Radiation Pressure Model . . . . .	58
5.4	Precise Orbit Determination Process . . . . .	58
5.4.1	GNSS-only POD . . . . .	58
5.4.2	GNSS+ISL POD . . . . .	59
<b>6</b>	<b>Results: Perfect Modeling</b>	<b>61</b>
6.1	Selection of Reference Scenarios . . . . .	61
6.2	Reference Orbits . . . . .	62

6.3	Results Perfect GNSS-only POD . . . . .	62
6.4	Results Perfect GNSS+ISL POD . . . . .	64
6.5	Ambiguity Fixing . . . . .	65
<b>7</b>	<b>Results: Individual Error Sources</b>	<b>67</b>
7.1	Clock Biases . . . . .	67
7.2	Thermal Noise . . . . .	68
7.3	Instrumental Delays . . . . .	70
7.4	Errors in the GNSS Orbits and Clocks . . . . .	71
7.5	Laser Noise . . . . .	73
7.6	Uncertainties in the Geopotential Model . . . . .	73
7.7	Uncertainties in the Solar Radiation Pressure Model . . . . .	75
7.8	Summary of Impact of Individual Error Sources . . . . .	77
<b>8</b>	<b>Results: Combined Error Sources</b>	<b>79</b>
8.1	List of Error Sources . . . . .	79
8.2	Results of Absolute Orbit Estimation . . . . .	80
8.2.1	Analysis of Empirical Accelerations . . . . .	80
8.2.2	Analysis of Absolute Orbit Accuracy . . . . .	81
8.3	Results of Relative Orbit Estimation . . . . .	82
8.3.1	Analysis of Relative Orbit Accuracy . . . . .	82
8.3.2	Achievement of Accuracy Requirement . . . . .	85
8.4	Result Consistency with Multiple Seeds . . . . .	85
8.5	Sensitivity to Errors in the GNSS Orbits and Clocks . . . . .	87
8.6	Sensitivity to Uncertainties in the Dynamical Model . . . . .	88
<b>9</b>	<b>Conclusions and Future Work</b>	<b>91</b>
9.1	Conclusions . . . . .	91
9.2	Future Work . . . . .	93
9.2.1	Assumptions Reconsideration . . . . .	93
9.2.2	Exploring Alternative Approaches . . . . .	94
	<b>References</b>	<b>95</b>
<b>A</b>	<b>Least Squares Algorithm</b>	<b>100</b>
A.1	Linearization . . . . .	100
A.2	Decomposition of the Jacobian . . . . .	101
A.3	Weighting . . . . .	102
A.4	A priori Information . . . . .	102

# List of Acronyms

<b>Acronym</b>	<b>Definition</b>
1D	One-Dimensional
3B	Three-Body
3D	Three-Dimensional
AGGA	Advanced GPS-Galileo ASIC
ANTEX	Antenna Exchange Format
ASIC	Application Specific Integrated Circuit
ATP	Acquisition, Tracking and Pointing
BDS	BeiDou Navigation Satellite System
BPSK	Binary Phase Shift Keying
C/A	Coarse/Acquisition (code)
CDMA	Code Division Multiple Access
CHAMP	Challenging Minisatellite Payload
CLO	Close scenario
CODE	Center for Orbit Determination in Europe
COST-G	Combination Service for Time-variable Gravity fields
CPOD	Copernicus Precise Orbit Determination
CPR	Cycle-Per-Revolution
DD	Double Difference
E1Q1	Q1 antenna of EHI-1
E1Q2	Q2 antenna of EHI-1
E2Q1	Q1 antenna of EHI-2
E2Q2	Q2 antenna of EHI-2
ECOM	Empirical CODE Orbit Model
ECOM-SGRA	Empirical CODE Orbit Model-Sagittarius A*
EDRS	European Data Relay System
EHI	Event Horizon Imager
EHT	Event Horizon Telescope
EIGEN	European Improved Gravity model of the Earth by New techniques
EIRP	Effective Isotropically Radiated Power
ESA	European Space Agency
ESOC	European Space Operations Centre
FAR	Far scenario
FDMA	Frequency Division Multiple Access
FOV	Field-Of-View
FPSSL	Free Space Path Losses
GAL	Galileo
GCRF	Geocentric Celestial Reference Frame
GEO	Geostationary Earth Orbit
GFZ	German Research Centre for Geosciences
GLONASS	Globalnaya Navigazionnaya Sputnikovaya Sistema
GNSS	Global Navigation Satellite System
GOCE	Gravity field and steady-state Ocean Circulation Explorer
GPS	Global Positioning System
GRACE	Gravity Recovery and Climate Experiment
GRACE-FO	Gravity Recovery and Climate Experiment Follow-On
HOI	High-Order Ionospheric
HWL	Hardware Losses
IAR	Integer Ambiguity Resolution
IF	Ionospheric-Free
IGS	International GNSS Service
IGSO	Inclined Geo-Synchronous Orbit

<b>Acronym</b>	<b>Definition</b>
IR	Infrared Radiation
ISL	Intersatellite Link
ISL-SGRA	Intersatellite Link - Sagittarius A* reference frame
LEO	Low Earth Orbit
LEOP	Launch and Earth Orbit Phase
LISA	Laser Interferometer Space Antenna
LTP	LISA Technology Package
M87*	Messier 87*
MAORI	Multi-purpose Advanced Orbit Restitution Infrastructure
MEO	Medium Earth Orbit
MID	Mid scenario
MW	Melbourne-Wübbena
NAPEOS	Navigation Package for Earth Orbiting Satellites
NavIC	Navigation Indian Constellation
NL	Narrow-Lane
OCXO	Oven-Controlled Crystal Oscillator
OD	Orbit Determination
OISL	Optical Intersatellite Link
ON	Orbital-Normal attitude mode
P	Precision code
PAA	Point Ahead Angle
PBD	Precise Baseline Determination
PCO	Phase Centre Offset
PCV	Phase Centre Variation
PEC	Patch Excited Cup
PNT	Positioning, Navigation and Timing
POD	Precise Orbit Determination
PODRIX	Precise Orbit Determination Receiver
PPS	Precise Positioning Service
PRISMA	PRecursore IperSpettrale della Missione Applicativa
PROBA-3	Project for On-Board Autonomy-3
PRP-MEO	Precise Relative Positioning in MEO to Support Science Missions
QZSS	Quasi-Zenith Satellite System
RAAN	Right Ascension of the Ascending Node
RF	Radio-Frequency
RMS	Root-Mean-Square
RUAG	Rüstungs Unternehmen Aktiengesellschaft
S3-A	Sentinel-3A
S3-B	Sentinel-3B
S6-A	Sentinel-6A
SD	Single Difference
Sgr A*	Sagittarius A*
SGRA	Sagittarius A*
SIM	Simulation
SINEX	Solution INdependent EXchange
SNR	Signal-to-Noise Ratio
SP	Solar Panel
SPP	Single Point Positioning
SR	Single-Receiver
SRP	Solar Radiation Pressure
SVLBI	Space Very Long Baseline Interferometry
TanDEM-X	TerraSAR-X add-on for Digital Elevation Measurement
TCXO	Temperature Compensated Crystal Oscillator
TERM	Terminator frame

---

<b>Acronym</b>	<b>Definition</b>
USO	Ultra-Stable Oscillator
VLBI	Very Long Baseline Interferometry
WL	Wide-Lane
WLS	Weighted Least Squares

---

# List of Symbols

Symbol	Definition
$c$	Speed of light
$b_0$	Initial bias
$b_{\text{clk}}$	Clock bias
$d$	Correlation spacing
$d_0$	Initial drift
$d_{\text{clk}}$	Clock drift
$dt_r$	Receiver clock offset
$dt^s$	Emitter clock offset
$f$	Frequency
$k_B$	Boltzmann constant
$m$	Carrier phase multipath error
$m_{\text{sat}}$	Satellite's mass
$p$	Pseudorange
$r$	Geocentric orbital radius
$r_r$	Receiver geocentric distance
$r^s$	Emitter geocentric distance
$t_r$	Receiving time
$t_t$	Transmission time
$v$	Orbital uncorrelated Gauss-Markov error
$w$	Clock uncorrelated Gauss-Markov error
$A$	Cross-sectional area
$A_m$	Amplitude of orbital error
$B$	Loop bandwidth
$B_{r,CP}$	Receiver phase instrumental bias
$B_{r,PR}$	Receiver code instrumental bias
$B_{CP}^s$	Emitter phase instrumental bias
$B_{PR}^s$	Emitter code instrumental bias
$B_0$	Constant coefficient in B direction
$B_c$	Cosine coefficient in B direction
$B_s$	Sine coefficient in B direction
$C_R$	Radiation pressure coefficient
$C/N_0$	Carrier-to-noise ratio
$D_0$	Constant coefficient in D direction
$D_c$	Cosine coefficient in D direction
$D_s$	Sine coefficient in D direction
$G_{RX}$	Receiver antenna gain
$G_{TX}$	Transmitter antenna gain
$G/T$	Gain-to-noise temperature ratio of the receiver antenna
$HWL_{RX}$	Receiver hardware losses
$HWL_{TX}$	Transmitter hardware losses
$I$	Ionospheric delay
$J$	Cost function of the least-squares algorithm
$M$	Pseudorange multipath error
$N$	Carrier phase ambiguity
$N_{WL}$	Wide-lane carrier phase ambiguity
$N_{IF}^{SD}$	Single-differenced ionospheric-free carrier phase ambiguity
$N_{NL}^{SD}$	Single-differenced narrow-lane carrier phase ambiguity
$N_{WL}^{SD}$	Single-differenced wide-lane carrier phase ambiguity
$P_{nm}$	Legendre polynomials of degree $n$ and order $m$
$P_{TX}$	Transmitted power
$P_{\odot}$	Solar radiation pressure at 1 AU

Symbol	Definition
$R$	Earth radius
$SD$	Standard deviation of instrumental biases
$SD_{CP}^s$	Standard deviation of emitter phase instrumental biases
$SD_{PR}^s$	Standard deviation of emitter code instrumental biases
$T$	Tropospheric delay
$T_c$	Coherent integration time
$T_{sys}$	System noise temperature
$U$	Earth's gravity potential
$Y_0$	Constant coefficient in Y direction
$Y_c$	Cosine coefficient in Y direction
$Y_s$	Sine coefficient in Y direction
$N(\mu, \sigma)$	Normal distribution with mean $\mu$ and standard deviation $\sigma$
$U(a_{\min}, a_{\max})$	Uniform distribution between $a_{\min}$ and $a_{\max}$
$\alpha$	Right ascension
$\alpha_{IR}$	Infrared absorptance
$\alpha_{VIS}$	Visible absorptance
$\delta$	Declination
$\delta^{rel}$	Relativistic range correction
$\epsilon$	Observation residuals
$\epsilon_r$	Carrier phase receiver noise
$\varepsilon$	Surface reflectivity
$\varepsilon_r$	Pseudorange receiver noise
$\zeta^s$	Carrier phase correction due to emitter phase centre offset and variation
$\zeta_r$	Carrier phase correction due to receiver phase centre offset and variation
$\nu$	Shadow function
$\xi^s$	Pseudorange correction due to emitter phase centre offsets
$\xi_r$	Pseudorange correction due to receiver phase centre offsets
$k_r$	Carrier phase receiver instrumental delays
$k^s$	Carrier phase emitter instrumental delays
$\lambda$	Wavelength
$\lambda_{NL}$	Narrow-lane wavelength
$\lambda_{WL}$	Wide-lane wavelength
$\lambda_C$	Chip length
$\lambda_L$	Geocentric longitude
$\mu$	Earth's gravitational parameter
$\mu_{r;WL}$	MW combination of the receiver biases in units of wavelength
$\mu_{WL}^s$	MW combination of the transmitter biases in units of wavelength
$\rho$	True geometric range
$\rho_{d,IR}$	Infrared diffuse reflectance
$\rho_{d,VIS}$	Visible diffuse reflectance
$\rho_{s,IR}$	Infrared specular reflectance
$\rho_{s,VIS}$	Visible specular reflectance
$\phi$	Geocentric latitude
$\varphi$	Phase of orbital error
$\sigma_1$	Clock diffusion coefficient of the phase deviation
$\sigma_2$	Clock diffusion coefficient of the random walk component of the frequency deviation
$\sigma_v$	Standard deviation of the orbital Gauss-Markov error
$\sigma_w$	Standard deviation of the clock Gauss-Markov error
$\sigma_A$	Standard deviation of the amplitude of the orbital error
$\sigma_{CP}$	Carrier phase thermal noise
$\sigma_{ISL}$	Laser white noise
$\sigma_{PR}$	Pseudorange thermal noise
$\tau_r$	Correlation time of the orbital Gauss-Markov error
$\tau_\delta$	Correlation time of the clock Gauss-Markov error

<b>Symbol</b>	<b>Definition</b>
$\omega$	Phase wind-up frequency
$\Delta f$	Frequency drift
$\Delta r_{3D}$	Three-dimensional position error
$\Delta r_{baseline}$	Position error projected along the baseline direction
$\Delta r_{orth}$	Position error projected along the pseudo-orthogonal direction
$\Delta r_{sgra}$	Position error projected along the Sagittaria A*
$\Delta r_{harm}$	Orbital harmonic error
$\Delta r_{GM}$	Orbital Gauss-Markov error
$\Delta t$	Clock sampling rate
$\Delta t_{orb}$	Clock orbit-related error
$\Delta t_{GM}$	Clock Gauss-Markov error
$\Gamma$	Errors in the laser pseudorange
$K_r$	Pseudorange receiver instrumental delays
$K^s$	Pseudorange emitter instrumental delays
$\Phi$	Carrier phase
$a_0$	Constant CPR coefficients
$a_1$	Cosine CPR coefficients
$a_2$	Sine CPR coefficients
$a_{apr}$	A priori analytical solar radiation pressure acceleration
$e_n$	Unit vector normal to the orbital plane
$u$	Argument of latitude
$e_{D,Y,B}$	Unit vectors in the D, Y, B directions of the ECOM model
$e_{\tilde{D},\tilde{Y},\tilde{B}}$	Unit vectors in the D, Y, B directions of the ECOM-SGRA model
$e_{T_1,T_2,T_3}$	Unit vectors of the TERM frame
$e_{SGRA}$	Sagittarius A* geocentric unit vector
$e_{\odot}$	Sun geocentric unit vector
$n$	Normal vector to reflecting surface
$r_1$	Inertial position vector of EHI-1
$r_2$	Inertial position vector of EHI-2
$r_{1/2}$	Relative position between EHI-1 and -2
$r_s$	Emitter inertial position vector
$r_{\odot}$	Sun geocentric position vector
$v_s$	Emitter inertial velocity vector
$r_{SGRA}$	Inertial position vector of Sagittarius A*
$\ddot{r}$	Acceleration
$\ddot{r}_{3B}$	Three-body acceleration
$\ddot{r}_{emp}$	Empirical acceleration
$\ddot{r}_{rel}$	Relativistic acceleration
$\ddot{r}_{SRP}$	Solar radiation pressure acceleration
$p$	Perturbing acceleration
$v$	Inertial velocity vector
$x_0$	Initial position and velocity
$y$	State vector
$z$	Observations vector
$A$	Partial design matrix
$E$	Rotation matrix from body-fixed to inertial frame
$H$	Jacobian matrix
$P_0^{apr}$	A priori covariance matrix
$S$	Sensitivity matrix
$W$	Weighting matrix
$\phi$	State transition matrix
$\Lambda$	Information matrix

# Introduction

The field of Precise Orbit Determination (POD) has experienced a remarkable growth in recent decades, primarily driven by the increasing demands of Earth observation missions with stringent positioning requirements. Missions such as the Sentinel series have played a pivotal role in propelling the advancements in POD within the space industry. POD techniques have been employed not only in single-satellite configurations like the Sentinels but also in satellites operating in formation flying configurations, such as the Swarm constellation or GRACE (Gravity Recovery and Climate Experiment). Typically, Earth observation missions are located at a Low Earth Orbit (LEO) as it provides an optimal altitude regime for their scientific objectives. However, there are also missions that operate at different orbital conditions, further expanding the scope of POD techniques.

This thesis focuses on a mission concept proposed by the European Space Agency (ESA) to image black holes, specifically Sagittarius A\*, using a constellation of space-borne Very Long Baseline Interferometry (VLBI) telescopes located at Medium Earth Orbit (MEO). Achieving a very accurate three-dimensional baseline determination at the millimetre level is essential for processing the VLBI signals measured by the distributed telescopes and obtaining detailed images of the target black hole. Therefore, the precise relative orbit determination of the MEO-based VLBI telescopes becomes a vital aspect of this mission concept.

Precise orbit determination often relies on Global Navigation Satellite System (GNSS) observations, which enable the reconstruction of highly accurate orbits. In absolute POD, GNSS measurements are processed independently for each satellite, while in relative POD, one satellite serves as the reference for estimating the orbits of the other satellites relative to it. Although double-differenced GNSS observations are commonly used in relative POD, they are not suitable for the specific problem addressed in this thesis due to the large intersatellite distances. Instead, this thesis focuses on relative POD using undifferenced GNSS observations and range measurements. These range observations are typically obtained through radio or optical Intersatellite Links (ISLs), which provide precise intersatellite measurements to enhance relative navigation.

The proposed technology to meet the challenging relative positioning requirements of the mission under investigation in this thesis is to employ both GNSS and ISL observations to accurately determine the relative distances between satellites within the constellation. While existing missions like GRACE and GRACE Follow-On in the LEO regime use precise range measurements, they typically involve shorter baseline distances. Consequently, precise relative navigation in higher orbital regimes such as MEO, particularly with high-dynamic baselines, remains a relatively unexplored subject in the field.

The present thesis builds upon the work conducted by Guindal-Martinez (2020) and GMV (2022) in studying the same mission. Nevertheless, the assumptions made in their research will be revisited in this study, and a particular focus will be placed on exploring the use of integer ambiguity resolution. This aspect is crucial for advancing the understanding of precise relative navigation in high-dynamic baselines and refining the techniques proposed by previous researchers.

This chapter serves as an introduction to the thesis, starting with a description of the problem at hand. The chapter then delves into a characterization of the properties of the proposed satellite constellation, including its orbital configuration, pointing strategy, macro-modeling, and sensor suite. The baseline dynamics and mission time frame are also discussed. A review of previous studies related to this constellation is presented, emphasizing significant findings and reassessing the underlying assumptions. The chapter continues with a research proposal, outlining the research objective and questions to be addressed. Finally, the thesis outline is provided, summarizing the structure and content of the remaining chapters.

## 1.1. Problem Description

The Event Horizon Telescope (EHT) is a global Very Long Baseline Interferometry (VLBI) array of telescopes, specifically designed to measure interferometric visibilities for the purpose of imaging and studying the event horizon of black holes (Akiyama et al., 2019). The primary targets of the EHT are Sagittarius A\* (Sgr A\*) at the centre of the galaxy and the black hole located at the centre of the Messier 87 galaxy (M87\*). Figure 1.1 presents an image of Sagittarius A\*, obtained using the EHT, highlighting the remarkable capabilities of this telescope system.

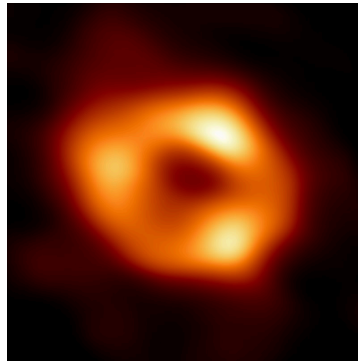


**Figure 1.1:** Sagittarius A\* imaged by the Event Horizon Telescope (EHT Collaboration, 2022).

The EHT performs sub-millimetre interferometry from the ground and thus its performance is limited by atmospheric effects, sparse coverage of the sky, and restricted angular resolution. Particularly, the angular resolution is constrained by the baseline length between telescopes, which is inherently limited by the Earth's diameter. To overcome these challenges, one potential solution is to deploy VLBI telescopes in space (Kudriashov et al., 2021). By venturing into space, the EHT can enhance its performance and unlock new opportunities for groundbreaking astronomical observations.

In order to develop this space VLBI (SVLBI) system, it is required to achieve a very precise baseline determination (PBD) (Kudriashov et al., 2021). Recognizing this necessity, the European Space Agency (ESA) awarded GMV a study titled "Precise Relative Positioning in MEO to Support Science Missions" (PRP-MEO). The main objective of this project was to investigate and evaluate the critical technologies needed to achieve accurate relative positioning in Medium Earth Orbit (MEO) to support scientific applications. The study focused on a specific scenario involving a constellation comprising two coplanar MEO satellites with an altitude offset of 23.3 km and equipped with VLBI antennas. These satellites are referred to as Event Horizon Imagers (EHI), forming the EHI constellation. It is worth noting that a similar analysis could be conducted for constellations designed to serve other scientific endeavors, such as Earth observation or lunar navigation (GMV, 2022).

The initial requirement of the PRP-MEO study aimed for a post-processing accuracy of 0.1 mm (3-sigma) in each of the three relative coordinates. However, a thorough analysis conducted by GMV (2022) demonstrated that attaining a 0.1 mm relative position accuracy in post-processing is currently unattainable. As a result, ESA reconsidered this requirement based on the latest findings from Radboud University, which suggest that a 1-dimensional relative position accuracy of 3.5 mm (3-sigma) can be deemed acceptable in post-processing. It is crucial to note that the direction pointing towards the black hole is of utmost importance in VLBI measurement processing. Therefore, the baseline projected in this direction assumes a particularly significant role in the analysis of the performance of the EHI constellation (GMV, 2022).

To meet the relative navigation objectives, the EHI satellites are equipped with both Global Navigation Satellite System (GNSS) receivers and an Intersatellite Link (ISL). The GNSS receivers need to be multi-constellation and multi-frequency. This choice of multi-constellation receivers ensures maximum visibility of the GNSS satellites at the relatively high altitude of the EHI spacecraft, which is around 8,300 km. Furthermore, dual-frequency measurements are beneficial for eliminating the first-order ionospheric signal delays (GMV, 2022).

The ISL sensor serves a dual purpose: supporting the onboard VLBI correlation process and facilitating ranging between the two EHI spacecraft. For efficient data transfer and meeting the accuracy requirements of relative navigation, optical ISL (OISL) technology has been selected. Optical ISLs oper-

ate at shorter wavelengths compared to radio-frequency (RF) links. The shorter wavelength translates into a higher frequency and greater bandwidth, enabling a higher data rate and improved range accuracy. Nevertheless, it should be noted that ISL range measurements are subject to unavailability during periods when the signal is blocked by the Earth. To address this, a strategy has been proposed, involving the adjustment of the orbit altitude of the two satellites before losing visibility, effectively avoiding blind periods caused by Earth obstruction (GMV, 2022).

## 1.2. EHI Constellation Properties

### 1.2.1. Orbital Configuration and Pointing Strategy

The EHI constellation comprises two spacecraft, namely EHI-1 and EHI-2, positioned in coplanar polar orbits with altitudes of 8,280 km and 8,303.3 km, respectively (GMV, 2022). The initial altitude offset between them is then 23.3 km. The selection of the Right Ascension of Ascending Node (RAAN) is carefully determined to be between the black holes Sagittarius A\* and M87\*, the primary targets of the EHI mission. In particular, the mean RAAN is approximately 140.9 degrees (GMV, 2022), as depicted in Figure 1.2. Table 1.1 presents the initial state vectors of EHI-1 and EHI-2 expressed in Keplerian elements.

Initial state vector	EHI-1	EHI-2
Semi-major axis [km]	14651.0	14674.3
Eccentricity [-]	0	0
Inclination [deg]	90	90
RAAN [deg]	140.9	140.9
Argument of Perigee [deg]	0	0
True Anomaly [deg]	0	0

**Table 1.1:** Initial state vector of the EHI-1 and EHI-2 satellites, represented in Keplerian elements.

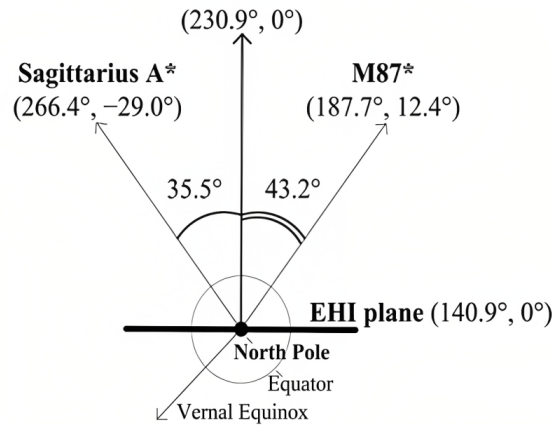


**Figure 1.2:** Orientation of Sagittarius A\*, M87\* and the EHI orbital plane in inertial coordinates (GMV, 2022).

Although the mission aims to image both black holes, this thesis primarily focuses on Sagittarius A\* with the understanding that a similar analysis could be carried out for M87\* as well. Consequently, the attitude law governing the satellites is designed to point towards Sagittarius A\* which maintains constant inertial coordinates over time. Figure 1.3 illustrates the pointing of the EHI constellation towards Sagittarius A\*, represented in inertial coordinates. This figure provides a simplified visual representation of the orientation of the spacecraft with respect to the target black hole.

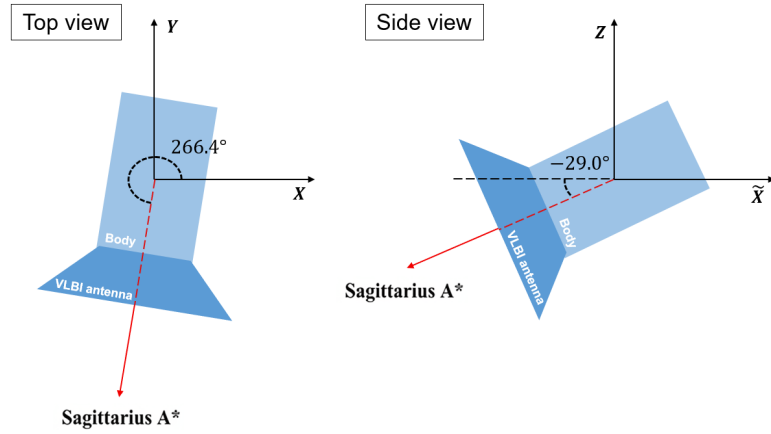


**Figure 1.3:** Illustration of the attitude law for Sagittarius A\* pointing. The figure provides a top view and a side view representation of the attitude law of the EHI spacecraft, which is designed to continuously point towards Sagittarius A\* ( $\alpha = 266.4$  deg,  $\delta = -29.0$  deg).

### 1.2.2. Satellite Macro-Modeling

Each EHI satellite consists of a main bus housing the payloads and is equipped with a static solar panel attached to the bus. The total weight of each satellite is 1,500 kg. The overall configuration of the EHI satellite — including the placement of the GNSS antennas, the ISL instrument, the VLBI antenna, and the solar panel — is depicted in Figure 1.4. The locations of all sensors and the centre of mass are detailed in Table 1.2.

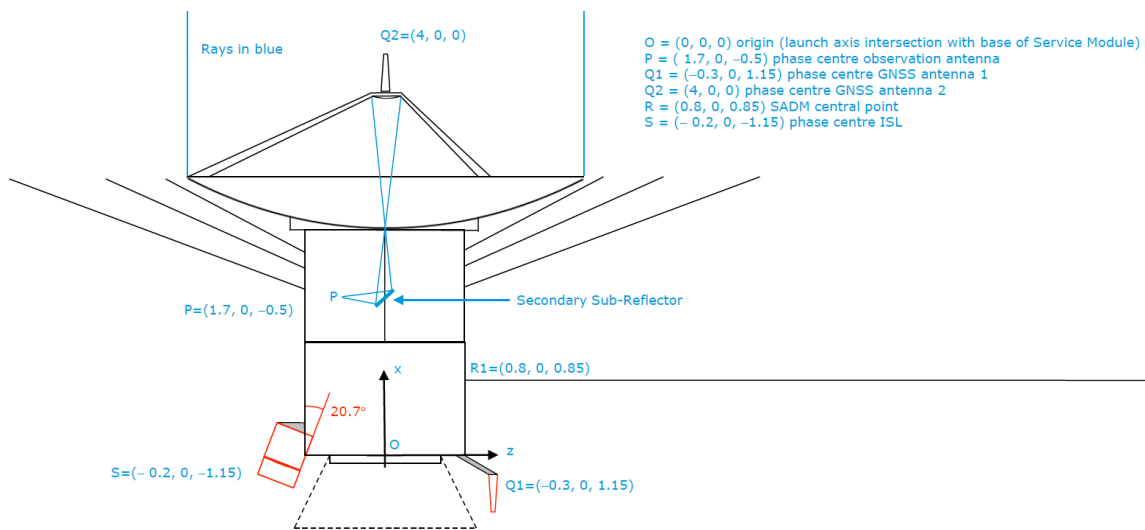


**Figure 1.4:** Configuration of the EHI satellite with the location of the reference points (Martin-Neira et al., 2020).

Element	X [m]	Y [m]	Z [m]
GNSS Q1	-0.30	0.00	1.15
GNSS Q2	4.00	0.00	0.00
ISL	-0.20	0.00	-1.15
VLBI	1.70	0.00	-0.50
Centre of mass	1.70	0.00	0.00

**Table 1.2:** Reference point locations with respect to the launch axis intersection with the base of the service module (GMV, 2022).

Figure 1.5 provides a representation of the full macro-model of the EHI satellites. However, due to its complexity, a simplified representation of the spacecraft is shown in Figure 1.6, dividing it into three main parts: the body, the solar panel (SP), and the VLBI antenna. The areas of this simplified macro-model are compiled in Table 1.3. The X panels represent the VLBI antenna, while the Y and Z panels represent the lateral areas of the main body. In addition, Table 1.3 summarizes the optical properties of the spacecraft, including the visible specular reflectance ( $\rho_{s,VIS}$ ), visible diffuse reflectance ( $\rho_{d,VIS}$ ), visible absorptance ( $\alpha_{VIS}$ ), infrared specular reflectance ( $\rho_{s,IR}$ ), infrared diffuse reflectance ( $\rho_{d,IR}$ ), infrared absorptance ( $\alpha_{IR}$ ), and whether re-radiation is considered. This simplified macro-model of the satellite will be employed to model solar radiation pressure, Earth re-radiation, and albedo during the simulations.

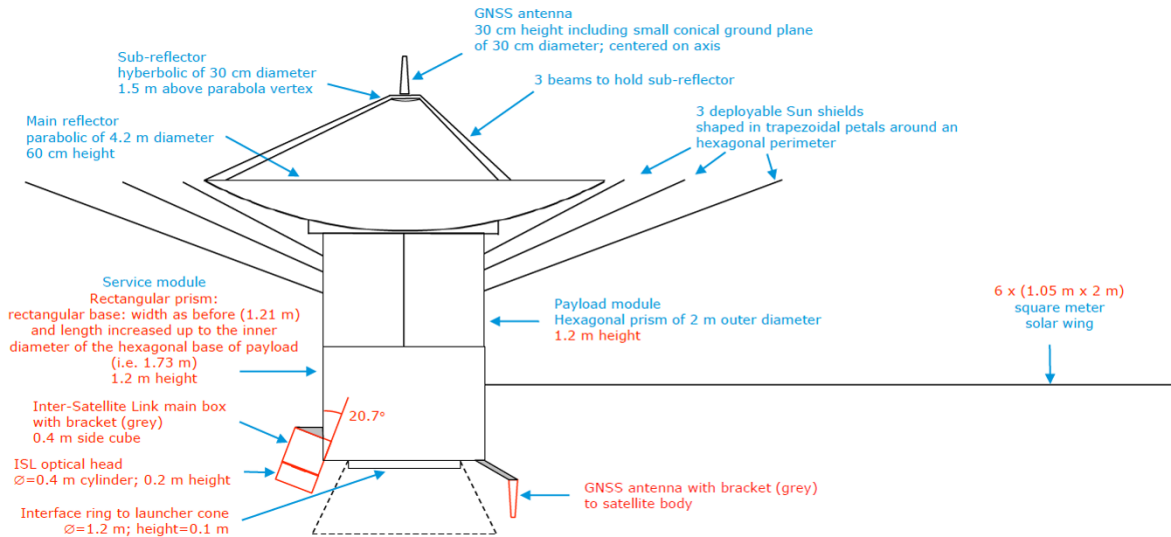


Figure 1.5: Full macro-model of the EHI satellite (Martin-Neira et al., 2020).

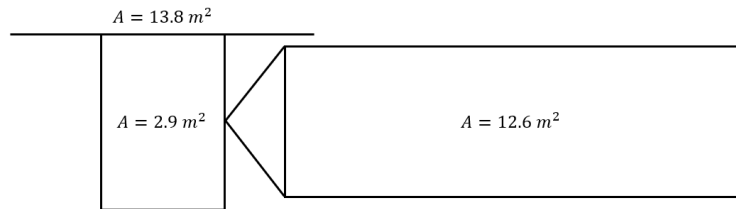


Figure 1.6: Simplified macro-model of the EHI satellite (GMV, 2022).

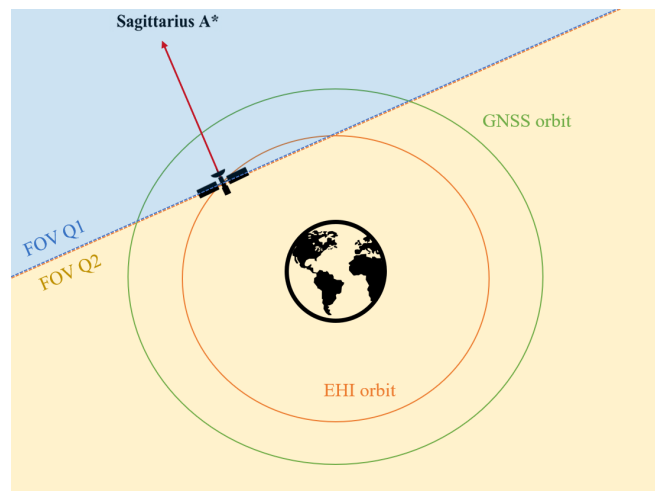
Panel	Area [m <sup>2</sup> ]	$\rho_{s,VIS}$ [-]	$\rho_{d,VIS}$ [-]	$\alpha_{VIS}$ [-]	$\rho_{s,IR}$ [-]	$\rho_{d,IR}$ [-]	$\alpha_{IR}$ [-]	Re-radiation
+X, -X	13.8	0.600	0.050	0.350	0.190	0.200	0.610	Yes
+Y	2.9	0.2312	0.3362	0.4326	0.1462	0.1016	0.7522	Yes
-Y	2.9	0.2096	0.0446	0.7458	0.2213	0.0661	0.7126	Yes
+Z	2.9	0.4205	0.0450	0.5245	0.13764	0.20646	0.6559	Yes
-Z	2.9	0.357	0.073	0.570	0.192	0.191	0.617	Yes
SP front	12.6	0.090	0.0	0.910	0.190	0.0	0.810	No
SP back	12.6	0.080	0.0	0.920	0.0	0.180	0.820	No

Table 1.3: Areas and surface optical properties of the EHI simplified macro-model (GMV, 2022).

### 1.2.3. Sensor Suite

Each EHI spacecraft is equipped with several sensors, including two GNSS antennas, an ISL instrument, a VLBI antenna, and a master clock. These sensors play a crucial role in the overall functionality of the EHI constellation. However, as the focus of this study primarily revolves around relative navigation, further details regarding the VLBI antenna will not be discussed in this context.

One of the key factors contributing to precise relative positioning within this project is the Global Navigation Satellite System. The chosen configuration entails the use of two hemispherical GNSS antennas positioned on opposite sides of the spacecraft. This arrangement maximizes the field-of-view (FOV) and increases the number of visible GNSS satellites. One of the antennas (Q1) is oriented towards the target black hole, while the other antenna (Q2) points in the opposite direction. Figure 1.7 presents a simplified illustration of the antenna configuration, assuming a field-of-view of 180 degrees for both antennas. This configuration ensures that the EHI satellites have an effective view of the entire sky, maximizing the visibility for precise relative positioning purposes.



**Figure 1.7:** Illustration of the antenna configuration for the EHI spacecraft, showing two hemispherical GNSS antennas (Q1 and Q2) positioned on opposite sides of the spacecraft.

For post-processing purposes, both the GPS (Global Positioning System) and Galileo (GAL) constellations are taken into consideration. The current state-of-the-art in multi-constellation GNSS receivers for space applications is represented by the Advanced GPS-Galileo Application Specific Integrated Circuit (AGGA) devices. Notable developments utilizing AGGA-4 include the precise orbit determination receivers (PODRIX) developed by RUAG (Rüstungs Unternehmen Aktiengesellschaft). These receivers are employed in missions such as the Earth observation Copernicus Sentinels-1, -2, -3, and -6, as well as the future PROBA-3 (Project for On-Board Autonomy-3) mission (GMV, 2022).

In terms of the ISL sensor, the design takes inspiration from the optical communication technology demonstrated by TESAT. TESAT promises a ranging accuracy of  $1 \mu\text{m}$  with a 2 Gbps chipping rate and a range of the optical link larger than 45,000 km (Zech et al., 2015). The proposed ISL sensor models are based on a Nd-YAG laser operating at a wavelength of 1064 nm. These models incorporate a coherent homodyne Binary Phase Shift Keying (BPSK) detection scheme. It is worth noting that the European Data Relay Satellite (EDRS) constellation has already integrated TESAT's second-generation optical ISLs for establishing Geostationary Earth Orbit (GEO) to LEO links (Poncet et al., 2017).

The master clock serves an important function in various aspects of the mission, supporting the operations of the GNSS receivers, the main payload, and the optical ISL. Due to the demanding requirements of the VLBI correlation process and precise relative positioning, a more advanced solution than a simple Temperature Compensated Crystal Oscillator (TCXO) is needed. An ultra-stable Oven-Controlled Crystal Oscillator (OCXO) is likely necessary to meet the needs of the mission. For example, the Sentinel-3A and Sentinel-6A missions employ an ultra-stable OCXO (USO) as their master clock to ensure the stability and accuracy of the timing measurements (Jalabert & Mercier, 2018; Montenbruck et al., 2021). When considering the required clock accuracy and stability, an USO is expected to exhibit an upper limit of the Allan deviation ranging from  $5.3 \times 10^{-12}$  s/s at time intervals of 1 s down to  $1.2 \times 10^{-13}$  s/s at 100 s (Montenbruck et al., 2021).

### 1.2.4. Baseline Dynamics

The two EHI satellites will be launched in close proximity to each other, with an initial separation of 23.3 km. However, due to their different altitudes, they will naturally evolve and gradually separate from each other over time. This is a result of the different semi-major axes, which lead to different orbital periods for each satellite. As a consequence, the satellites will eventually be positioned on opposite sides of the Earth. As their orbits continue to progress, the satellites will begin to approach each other once again. It is important to note that if no corrective manoeuvres are performed, there will be a period where the Earth comes in between the two satellites, blocking the signal of the intersatellite link.

Figure 1.8 shows the evolution of the relative distance between the satellites over a 100-day period. In the plot, the yellow points represent signals crossing the ionosphere, assuming the top of the ionosphere is at 1,000 km. On the other hand, the red points indicate the time when the spacecraft do not have line-of-sight visibility due to the blockage of the Earth. The relative geometry between the EHI orbits exhibits an 86-day cycle, with approximately 29.5 days of ISL visibility. The baseline varies between around 23.3 km and 25,000 km in less than one month, highlighting the high-dynamic baseline nature of the EHI constellation.

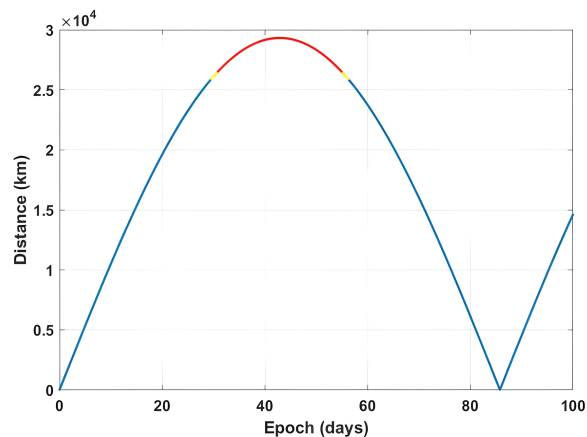


**Figure 1.8:** Evolution of the relative distance between EHI-1 and EHI-2 over a 100-day period. The red points show when the spacecraft are occulted by the Earth, and the yellow points show when the signal travels through the ionosphere (GMV, 2022).

### 1.2.5. Mission Time Frame

In order to select an appropriate simulation period for the EHI mission, several factors need to be considered. First, it is crucial to ensure that the ISL signal is not blocked by the Earth. Second, the simulation should fully capture the dynamic nature of the problem. Third, the chosen period should be free from eclipses that could affect the performance of the mission. Lastly, to ensure optimal imaging of the black hole, it is essential to prevent direct solar radiation from interfering with the VLBI antennas' signal.

To avoid the Sun passing over the field-of-view of the VLBI antennas during the simulation period, a conservative requirement is set, demanding the Sun to be located more than 90 degrees away from the FOV (GMV, 2022). This ensures a significant safety margin in preventing any potential interference. Figure 1.9 provides a visual representation of the EHI orbit and the positions of the relevant celestial bodies, although the distances are not represented to scale.

Considering these requirements, the selected simulation period for the EHI mission is the month of April. Starting from the 1st of April, which assumes the closest distance between the EHI satellites, the simulation extends up to the 30th of April. This period allows for the farthest distance between the satellites, ensuring the ISL can be employed without the obstruction of the Earth. It is important to remark that this thesis will not cover other mission phases such as the Launch and Earth Orbit Phase (LEOP) or the reconfiguration phase, where the satellite altitudes are adjusted to avoid Earth blockage.

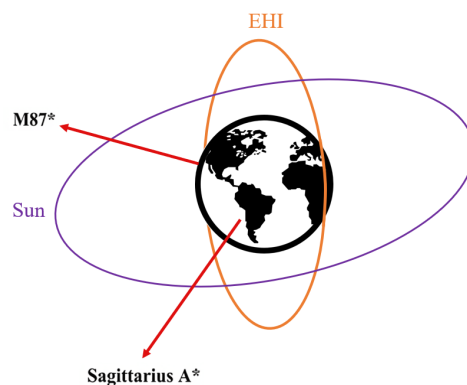


**Figure 1.9:** 3D representation of the EHI orbit and the positions of relevant celestial bodies.

## 1.3. Review of Previous Studies

In this section, previous studies that have contributed to the development of this thesis will be discussed. Specifically, this thesis builds upon the research conducted by Guindal-Martinez (2020) and GMV (2022). However, there are notable differences between these two studies. Guindal-Martinez (2020) focused on a single nadir-pointing GNSS antenna and relied on real GNSS products provided by CNES (Centre National d'Etudes Spatiales). In contrast, GMV (2022) considered the use of two GNSS antennas and performed simulations of the GNSS products. Therefore, the results obtained by GMV (2022) align more closely with the setup of this thesis, and as a result, they will be the primary reference for this study.

### 1.3.1. Key Outcomes of Previous Studies

In the previous study conducted by Guindal-Martinez (2020), several relevant conclusions were drawn. One key aspect investigated was the impact of the minimum grazing altitude on the total number of visibility contacts. Two possibilities were considered: a grazing altitude of 100 km to eliminate tropospheric-affected observations and a grazing altitude of 1,000 km to eliminate also ionospheric-affected observations. After careful analysis, a grazing altitude of 100 km was determined to be the optimal choice, as setting it at 1,000 km resulted in a significant drop in the number of observations. It was noted that the complete elimination of signals traveling through the ionosphere was not deemed necessary, particularly when dual-frequency observations were employed.

Furthermore, Guindal-Martinez (2020) identified that the most favourable antenna configuration for optimizing the number of contacts involved a pair of hemispherical antennas pointing in opposite directions. Based on these findings, the subsequent study conducted by GMV (2022) adopted the use of two GNSS antennas to further explore the subject.

The study conducted by GMV (2022) assessed the impact of various error sources on the final orbital error. The error budget included the GNSS and ISL measurement noise, errors in the GNSS orbits and clocks, and uncertainties in the geopotential model. The investigation specifically focused on the simulation period of April 2021, taking into account all the aforementioned error sources.

The main outcome of this study is presented in Figure 1.10, which shows the difference between the estimated relative position and the reference relative position. The figure provides an overview of the differences observed along three different axes. In particular, it highlights the differences in the baseline direction, the direction towards Sagittarius A\*, and a final pseudo-orthogonal direction.

The baseline direction presents the highest accuracy, primarily due to the use of the ISL, which greatly enhances the performance in that specific direction. The achieved 3-sigma accuracy in the baseline direction is 1.11 mm. Following closely is the Sagittarius A\* direction, which exhibits a relative position accuracy predominantly below 5 mm, with a 3-sigma value of 5.97 mm. On the other hand, the pseudo-orthogonal direction is the least precisely determined, showcasing excursions approaching 10 mm and the largest 3-sigma value of 8.09 mm. These 3-sigma accuracy values are summarized in Table 1.4.

Hence, it becomes evident that the relaxed requirement of a relative position accuracy of 3.5 mm (3-sigma) is solely fulfilled in the baseline direction. The results of this study lead to the conclusion that

while the incorporation of the ISL significantly reduces errors in the baseline direction, it has minimal, if any, impact on the accuracy of the other directions.

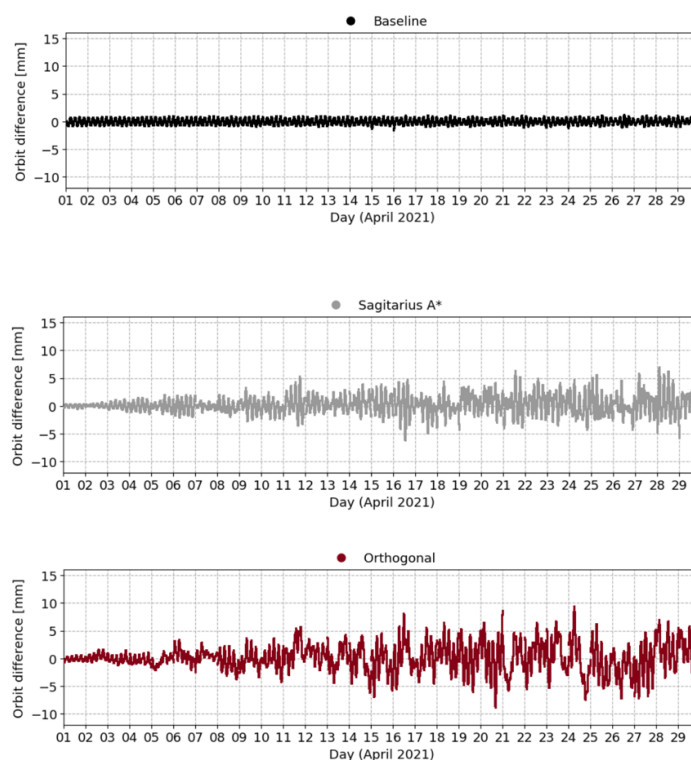


**Figure 1.10:** EHI relative orbital differences in the baseline, Sagittarius A\*, and orthogonal directions obtained by the study conducted by GMV (2022).

Baseline	Sagittarius A*	Orthogonal
1.11 mm	5.97 mm	8.09 mm

**Table 1.4:** EHI relative position 3-sigmas in the baseline, Sagittarius A\* and orthogonal directions obtained by the study conducted by GMV (2022).

### 1.3.2. Revisiting Assumptions of Previous Studies

In the analysis conducted by GMV (2022), certain assumptions were made that need to be revisited. One significant aspect is the treatment of errors in the solar radiation pressure (SRP) model, which was not accounted for in their analysis. In contrast, Guindal-Martinez (2020) addressed this issue by introducing uncertainty in the cross-sectional area of the satellites to mimic errors in the SRP model. The author found that this uncertainty did not have a significant impact on the orbit solution because the introduced error in the area was effectively absorbed by the estimated solar radiation pressure coefficient. Therefore, this method may not accurately capture the uncertainties associated with the SRP model. A more realistic approach could involve using completely different SRP models in the simulation and estimation processes, thereby accounting for these dynamic uncertainties in a more comprehensive manner.

In the work carried out by GMV (2022), where the simulation of the GNSS orbits and clocks was incorporated, it was crucial to ensure that the orbits and clocks used in the POD differed from those employed in the generation of the simulated GNSS observations. Neglecting this differentiation would result in disregarding the inherent errors present in real GNSS products. To account for this, the GNSS products employed in the POD were generated from the nominal products but incorporated additional errors, resulting in orbital errors of 2.5 cm and clock errors of 5 ps. Nevertheless, further investigation is required to verify if these simulated errors reflect the errors present in real GNSS products.

Another notable assumption made was regarding the accuracy of the ISL, which may have been set too optimistically at the micrometre level. At this stage of the mission, it is challenging to provide an exact value for this figure. Nevertheless, considering the intended ranging technology and the large baseline distances, the literature suggests that a micrometre-level ISL ranging accuracy might not be realistic. Instead, a more conservative value of one millimetre is recommended (Michalak et al., 2020). Additional information on this topic will be discussed in Chapter 3.

The study performed by GMV (2022) incorporated empirical accelerations as part of the relative POD processing. However, a detailed investigation into the optimal set of empirical accelerations was not undertaken in this study. Hence, it would be valuable to conduct such an investigation in order to accurately parametrize the orbit determination problem.

Lastly, it is worth noting that the project conducted by GMV (2022) did not include carrier phase integer ambiguity resolution (IAR) in its analysis. Instead, the carrier phase ambiguity was treated as a floating number of cycles, disregarding the fixed integer nature of the ambiguity. Thus, the instrumental biases of emitters and receivers were neglected for the sake of simplicity. However, as indicated by Tenissen and Montenbruck (2017), resolving the integer nature of the ambiguity is of utmost importance for high-precision applications. Therefore, it is essential to investigate whether incorporating carrier phase integer ambiguity resolution into the post-processing improves the baseline determination.

## 1.4. Research Proposal

The research proposal is presented in this section, outlining the objectives and research questions that will be addressed in the current study. By establishing clear objectives and articulating the research questions, the scope of this thesis can be assessed, providing a road map to achieve the objectives and answer the research questions effectively.

### 1.4.1. Research Objective

The research objective of this thesis is to investigate the feasibility of achieving very precise relative positioning in a two-satellite constellation operating in Medium Earth Orbit for the purpose of black hole imaging, with a specific focus on the accurate determination of the baseline in the direction of the target black hole, Sagittarius A\*. The study aims to identify the limitations and challenges associated with high-precision relative navigation in such constellations, examining the role of integer ambiguity resolution and the use of intersatellite link observations along with GNSS. Additionally, a particular emphasis is placed on the analysis of the relationship between relative orbit accuracy and baseline distance while considering the impact of various error sources.

### 1.4.2. Research Questions

The following set of research questions aims to investigate the impact of different error sources on the accuracy of the relative POD solution and assess the overall performance of the solution in a realistic scenario. These questions delve into the role of integer ambiguity resolution, the use of ISL observations, the relationship between relative orbit accuracy and baseline distance, and the fulfillment of the relative navigation requirement. By addressing these questions, the study seeks to gain a deeper understanding of the limitations of achieving very precise relative navigation at MEO altitudes and over very long baselines.

**Q1)** What is the impact of including different error sources on the accuracy of the relative POD solution, and which ones are the most significant? Specifically, the influence of the following errors is examined:

- Q1.a) GNSS and receiver clock biases.
- Q1.b) Thermal noise in the GNSS observations.
- Q1.c) Instrumental delays in both the GNSS emitter and receiver antennas.
- Q1.d) Errors in the GNSS orbits and clocks.
- Q1.e) Gaussian white noise in the ISL observations.
- Q1.f) Uncertainties in the geopotential model.
- Q1.g) Uncertainties in the solar radiation pressure model.

**Q2)** What is the overall performance of the relative POD solution when considering all error sources simultaneously? In particular,

- Q2.a) How does integer ambiguity resolution affect the accuracy of the relative POD solution?
- Q2.b) How does the use of ISL observations contribute to the precise determination of the baseline in the direction of the target black hole?
- Q2.c) What is the relationship between relative orbit accuracy and baseline distance?
- Q2.d) Is the relative navigation requirement of achieving a relative position accuracy of 3.5 mm (3-sigma) in the direction of the target black hole met by the current system configuration? If not, what improvements can be implemented to achieve this requirement?

## 1.5. Thesis Outline

This thesis is organized into several chapters that present the relevant information required to address the research questions. Chapter 2 focuses on the GNSS technology, providing an overview of the available GNSS constellations, observables, signal delays, and its applications in relative navigation systems. Similarly, Chapter 3 offers an in-depth discussion of the ISL technology, including the observation model and the relevance of this technology in relative navigation.

In Chapter 4, the concepts, techniques, and software related to precise orbit determination are outlined. This chapter covers topics such as reference frames, the dynamic model, integer ambiguity resolution, and available software for POD applications. Following that, Chapter 5 provides a detailed explanation of the methodology employed in this thesis. It explains the generation of the reference orbits and clocks, the generation of the observations, the introduction of error sources, and the setup of the orbit determination process.

Subsequently, Chapters 6, 7, and 8 present the results. Chapter 6 presents the ideal scenario where no error sources are introduced, serving as a validation of the software tools developed for this thesis. Chapter 7 systematically introduces the errors one by one to assess their individual impact on the relative orbit accuracy and to identify the most influential ones. Afterwards, Chapter 8 combines all error sources together and shows the results of the POD in this more realistic scenario to check if the mission requirements are met. Lastly, Chapter 9 presents the conclusions drawn from the research and highlights areas for future work.

# Global Navigation Satellite Systems

A Global Navigation Satellite System (GNSS) is usually described as a constellation of satellites orbiting the Earth and continuously transmitting electromagnetic signals that allow both ground-based and space-borne applications. The focus of this report is on the latter. By processing the transmitted signals, it is possible to obtain the distance of the user to a set of GNSS satellites with known coordinates, which enables to compute the absolute position of the receiver (Sanz-Subirana et al., 2013). Two types of observables — pseudorange and carrier phase — can be used to determine the position of the space receiver. However, the travel time of these signals is affected by various effects, such as atmospheric delays or instrumental biases, which can introduce errors in the orbit determination.

In this chapter, the main navigation constellations available are presented. Subsequently, the different types of GNSS observables, their primary error sources, and the techniques for combining these observables to mitigate errors are explained. Finally, the chapter provides an overview of space missions employing GNSS for relative navigation.

## 2.1. GNSS Constellations

The availability of Global Navigation Satellite Systems has revolutionized positioning, navigation, and timing (PNT) applications over the past few decades. Currently, several GNSS constellations are in operation, providing global or regional coverage to users around the world and in space. The first operational GNSS constellation — that is, GPS (Global Positioning System) — was launched in the 1970s and was initially designed for military applications. Since then, other GNSS constellations, including GLONASS (Globalnaya Navigazionnaya Sputnikovaya Sistema), Galileo, and BeiDou, have been deployed.

Each constellation uses different frequency bands for signal transmission and generally consists of satellites located in nearly-circular orbits at altitudes around 20,000 km. To enhance coverage, the satellites within these constellations are placed in different orbital planes. Additionally, there are regional constellations such as QZSS (Quasi-Zenith Satellite System) and NavIC (Navigation Indian Constellation). This section provides an overview of the GNSS constellations available and their characteristics.

### 2.1.1. GPS

The Global Positioning System (GPS) is a satellite navigation system operated by the United States of America. The first satellite was launched in 1978, and since then, the GPS space segment has continuously grown through seven blocks in three generations: Block I (1978), II (1989), IIA (1990), IIR (1997), IIR-M (2005), IIF (2010) and III (2018). It is worth mentioning that satellites from Block I, II, and IIA are no longer operational. At the moment, the GPS constellation consists of 31 operational satellites that ensure the availability of at least 24 operational satellites at all times. The GPS satellites are located in six different orbital planes separated by 60 degrees in longitude, inclined 55 degrees, and at an altitude of 20,180 km (United Nations, 2021).

The legacy GPS signals are transmitted in two frequencies in the L band, L1 at 1,575.42 MHz and L2 at 1,227.60 MHz. The civilian Coarse/Acquisition (C/A) code, which is used in the Standard Positioning Service (SPS), is modulated on L1 while the military Precision (P) code, which is employed in the Precise Positioning Service (PPS), is modulated over both L1 and L2. Apart from these legacy signals, the GPS system modernization of 2005 included one new frequency band (L5 at 1,176.45 MHz), three additional civil signals (L2C, L5, L1C), and a military one (M) (Sanz-Subirana et al., 2013).

### 2.1.2. Galileo

Galileo is the European global navigation satellite system, consisting of a constellation of 30 satellites. Out of these 30 satellites, 24 are currently operational, while the remaining 6 serve as spares. The satellites are evenly distributed across three circular orbital planes that are separated by 120 degrees, inclined at an angle of 56 degrees, and have an altitude of approximately 23,222 km (United Nations, 2021).

Galileo uses four different frequency bands to transmit radio signals: E1 (1,575.42 MHz), E5a (1,176.45 Mz), E5b (1,207.14 MHz), and E6 (1,278.75 MHz). These bands support different services, but the specifics are beyond the scope of this thesis. One noteworthy aspect of Galileo is its open-service signal interoperability with other GNSS constellations, meaning that users can receive signals from multiple constellations simultaneously to improve accuracy and reliability (United Nations, 2021).

### 2.1.3. GLONASS

The GLONASS constellation is operated by the Russian government. Since the first satellite was launched in 1982, three generations of satellites have existed: GLONASS, GLONASS-M and GLONASS-K. The current constellation comprises 24 operational satellites belonging to the two last generations, which are evenly distributed across three orbital planes separated by 120 degrees in longitude. These satellites are inclined at an angle of 64.8 degrees and orbit at a nominal altitude of 19,100 km (Teunissen & Montenbruck, 2017).

The GLONASS constellation broadcasts signals in three frequencies: L1 (centred at 1602 MHz), L2 (centred at 1246 MHz), and L3 (centred at 1202 MHz) (Teunissen & Montenbruck, 2017). GLONASS uses a different signal modulation scheme compared to other GNSS constellations. GLONASS employs FDMA (Frequency Division Multiple Access) for signal transmission rather than CDMA (Code Division Multiple Access) (United Nations, 2021). In CDMA, each navigation satellite uses a different code and a process of cross-correlation is then employed in the receiver satellite. In the case of FDMA, all the satellites employ the same code and thus autocorrelation is required instead (Ávila-Rodríguez, 2018).

### 2.1.4. BeiDou

The Chinese navigation system, also known as BeiDou or BDS (BeiDou Navigation Satellite System), is unique among the GNSS constellations in that it includes both Geostationary Earth Orbit (GEO) and Inclined Geo-Synchronous Orbit (IGSO) satellites in addition to the standard MEO satellites. The constellation comprises 7 GEO satellites, 11 IGSO satellites, and 27 MEO satellites, all of which are part of the second and third generation of BeiDou (BDS-2 and BDS-3) (Xiaochun, 2022). BeiDou broadcasts signals on three frequency bands: B1 (1561.098 MHz), B2 (1207.14 MHz), and B3 (1268.52 MHz) (Teunissen & Montenbruck, 2017).

It is worth noting that the BeiDou-3 MEO satellites are equipped with intersatellite links that enable them to enhance their self-positioning accuracy. By employing intersatellite links, the dependence on ground monitoring stations is reduced, and the satellite orbits can be determined accurately with a reduced ground network. This technology is similar to the one explored in this thesis, where intersatellite ranging is used to enhance the accuracy of the positioning system.

## 2.2. GNSS Observables

This section describes the two main types of observables used in GNSS: pseudorange and carrier phase. Both observables are affected by various factors, such as atmospheric delays, satellite and receiver clock errors, and multipath, which must be taken into account in order to obtain accurate measurements. The observation equations for these variables are presented and discussed, along with the relevant effects that influence their determination.

### 2.2.1. Pseudorange

The GNSS receiver is able to measure the apparent signal travel time from the emitting satellite to the receiver satellite. This time is then multiplied by the speed of light to obtain the apparent range between emitter and receiver. Notice that this range is not the true geometric distance between the two satellites because it contains errors coming from different sources. That is the reason why the observable is called *pseudorange*. The true range is affected by the clock offsets of the emitter and the

receiver with respect to the GNSS system time as well as by other signal delays and errors. All these contributions to the pseudorange are included in Equation 2.1, where  $s$  refers to the emitter satellite,  $r$  to the receiver, and the sub-index  $f$  means that the term is frequency-dependant (Sanz-Subirana et al., 2013; Teunissen & Montenbruck, 2017).

$$p_f = \rho + c(dt_r - dt^s) + \delta^{rel} + T + I_f + K_{f,r} - K_f^s + \xi_{r,f}^s + M_f + \varepsilon_f \quad (2.1)$$

where

- $p_f$  is the pseudorange.
- $\rho$  is the true geometric range between the satellites.
- $c$  is the speed of light.
- $dt_r$  and  $dt^s$  are the clock offsets of the receiver and transmitter satellites with respect to the GNSS time scale, respectively.
- $\delta^{rel}$  is the relativistic correction due to space-time curvature.
- $T$  is the tropospheric delay, which is non-dispersive (does not depend on the signal frequency).
- $I_f$  is the ionospheric delay, which is frequency-dependant.
- $K_{f,r}$  and  $K_f^s$  are the receiver and transmitter instrumental delays, respectively.
- $\xi_{r,f}^s$  is the correction due to phase centre receiver and emitting antenna offsets.
- $M_f$  contains the multipath errors.
- $\varepsilon_f$  is the receiver noise.

The physical meaning of the above terms will be explained in Section 2.3. Furthermore, it should be emphasized that the position of both satellites must be expressed in the same reference frame for consistency.

### 2.2.2. Carrier Phase

In addition to the pseudorange observable, carrier phase measurements provide a more precise way to determine the distance between two satellites. This observable is obtained by measuring the fractional phase shift of the incoming carrier signal with respect to a replica created in the receiver. The short wavelength of the carrier phase makes the measurement much more precise than the pseudorange measurement (Teunissen & Montenbruck, 2017). Nevertheless, the carrier phase measurements are ambiguous by an unknown integer number of wavelengths that changes arbitrarily every time the receiver loses the signal (Sanz-Subirana et al., 2013). This phenomenon is called the carrier phase ambiguity and its resolution is one of the main challenges in GNSS positioning.

The carrier phase can be expressed as:

$$\Phi_f = \rho + c(dt_r - dt^s) + \delta^{rel} + T - I_f + k_{f,r} - k_f^s + \zeta_{r,f}^s + \lambda_f N_f + \lambda_f \omega + m_f + \epsilon_f \quad (2.2)$$

where, besides the terms previously described,

- $k_{f,r}$  and  $k_f^s$  are the carrier phase instrumental delays of the receiver and transmitter, respectively.
- $\zeta_{r,f}^s$  are the antenna phase centre corrections for the carrier phase.
- $\lambda_f$  is the frequency of the signal.
- $N_f$  is the integer ambiguity.
- $\lambda_f \omega$  is the so-called phase wind-up correction.
- $m_f$  gathers the carrier phase multipath errors.
- $\epsilon_f$  represents the receiver carrier phase noise.

## 2.3. GNSS Signal Delays

As mentioned in the previous section, various factors affect the precision of the GNSS observables. Some of these effects can be corrected by external data or models, while others need to be estimated during the orbit determination process. This section provides an overview of these signal errors and the methods used to model them.

### 2.3.1. Relativistic Effects

Both the path of the GNSS signal and the clocks are affected by relativity. Specifically, the range must be corrected due to the space-time curvature caused by the gravitational field of the Earth, which is known as the Shapiro effect. This effect can be accounted for using the formulation provided by Sanz-Subirana et al. (2013):

$$\Delta\rho_{rel} = \frac{2\mu}{c^2} \log\left(\frac{r^s + r_r + \rho_r^s}{r^s + r_r - \rho_r^s}\right) \quad (2.3)$$

where  $\mu$  is the gravitational parameter of the Earth,  $r^s$  and  $r_r$  are respectively the geocentric distance of the GNSS satellite and the receiver, and  $\rho_r^s$  is the distance between them.

Apart from the path of the GNSS signal, the clocks used in the satellites are also subject to relativistic effects. The frequency of a clock will drift due to both the difference in gravitational potential and the eccentricity of the orbit. To counteract the first effect, a constant offset is added to the clock oscillation frequency during manufacturing. The second effect, which causes a periodic time offset, is corrected as explained by Sanz-Subirana et al. (2013):

$$\Delta t_{rel} = -2 \frac{\mathbf{r}^s \cdot \mathbf{v}^s}{c^2} \quad (2.4)$$

where  $\mathbf{r}^s$  and  $\mathbf{v}^s$  are the GNSS satellite inertial position and velocity vectors. The same correction applies to the receiver clock.

It can be then concluded that the relativistic effects on GNSS observables are well-represented by these theoretical models. Therefore, the correction terms can be included directly in the observation model, without the need for additional parameters to be estimated.

### 2.3.2. Tropospheric Delay

The troposphere is the lowest layer of the atmosphere, extending from the surface of the Earth up to an altitude of about 60 km (Sanz-Subirana et al., 2013). GNSS signals traveling through the troposphere experience a delay due to refractive index variation caused by changes in the properties of the atmosphere. This change in refractive index translates into a curvature in the path of the signals, which makes the travel time longer.

The effect of tropospheric refraction is seen as a frequency-independent delay in the GNSS signal. This delay affects both pseudorange and carrier phase measurements in the same way. In this project, the signals transmitted between the GNSS and EHI satellites will not travel through the troposphere as a grazing altitude of 100 km has been set. Thus, the effect of the tropospheric refraction on the measurements can be neglected.

### 2.3.3. Ionospheric Delay

The ionosphere is a layer of the Earth's atmosphere between 60 km and 2,000 km that contains electrically charged particles (Sanz-Subirana et al., 2013). The delay of the GNSS signal passing through the ionosphere depends on the number of free electrons present along its path. This number can vary due to different factors such as the altitude, the time of the day, the season, and solar activity. Additionally, the ionosphere is a dispersive medium, meaning that the phase and code of the signal travel at different velocities. This results in a delay of the pseudorange and an acceleration of the carrier phase (Teunissen & Montenbruck, 2017).

An effective way to correct the 99% of the ionospheric delay is to use a dual-frequency combination of the observations. Since dual-frequency measurements will be employed in this mission, the first-order ionospheric delay is not of relevance since it can be removed through the ionospheric-free combination. Nevertheless, this combination does not remove the remaining high-order ionospheric (HOI) effects.

Guo et al. (2023) analyzed the impact of HOI delay on four different LEO satellites, namely Swarm-A/B, GRACE-A, and GOCE (Gravity field and steady-state Ocean Circulation Explorer), distributed in the altitude range of 200-500 km. The analysis revealed that the influence of HOI delay on LEO satellite GPS data ranged from millimetres to centimetres. The effect of HOI delay on the precision of the POD was found to be at the submillimetre level. Notably, the high-order ionospheric term at altitudes higher than 500 km showed minimal impact on observation data and orbit determination accuracy.

Considering that the EHI satellites operate at MEO altitudes, it can be inferred that the impact of HOI delays on GPS data for the EHI mission would be even less pronounced, as only a small portion of the signals travel through the lower layers of the ionosphere below 500 km (GMV, 2022). Therefore, for the purpose of this study, the simulation of GNSS observations did not incorporate ionospheric errors. The HOI effects are considered negligible, and the first-order ionospheric effects are removed using dual-frequency observables.

#### 2.3.4. Carrier Phase Wind-Up

Phase wind-up is an effect that arises from the electromagnetic nature of circularly polarized waves, such as those used in GNSS. As a GNSS satellite moves along its orbit, it rotates to keep its solar panels pointed towards the Sun, while the antenna continues pointing towards the Earth. This rotation causes a phase variation known as phase wind-up. A similar effect also occurs at a space-borne receiver. The wind-up frequency  $\omega$  is relatively easy to compute knowing the dipole orientation (Sanz-Subirana et al., 2013)

In Equations 2.1 and 2.2, it can be observed that phase wind-up only affects the carrier phase and not the pseudorange. Therefore, this correction is only required for applications that require precise positioning. Given the demanding positioning requirements of this mission, it is necessary to include this effect in the simulations.

#### 2.3.5. Antenna Phase Centre Offset and Variation

The range between the transmitting and receiving antennas is determined by the distance between their electrical phase centres, which may deviate from their geometrical centres. The deviation is usually split into two parts: the Phase Centre Offset (PCO) and the Phase Centre Variation (PCV). Both PCO and PCV depend on the type of antenna and the frequency of the signal, while the PCV also further relies on the elevation and azimuth.

The International GNSS Service (IGS) provides the PCOs and PCVs for GNSS satellites, while the on-board receiver PCOs and PCVs are calibrated on-ground and then re-estimated after launch (Teunissen & Montenbruck, 2017). Nevertheless, due to both the unavailability of PCV maps and software constraints, the estimation of the receiver PCVs during the POD process is not performed in this thesis.

#### 2.3.6. Instrumental Delays

Instrumental delays are caused by various factors such as transmission delays through the antenna cables, as well as due to the filters used in GNSS receivers. These delays impact both pseudorange and carrier phase measurements. The instrumental errors of GNSS satellites are typically obtained from an external source, like IGS, which provides precise observation biases.

In contrast, the instrumental delays of the receiver are included as part of the receiver clock estimation during the orbit determination process. These delays are also mitigated if differenced observations are employed. However, these approaches are less effective for multi-GNSS processing because the instrumental delays coming from different GNSS systems are not identical (Teunissen & Montenbruck, 2017). To address this issue, an additional parameter known as the intersystem bias is introduced, which accounts for both the differences in instrumental delays and the variations in time scales among different constellations (Pan et al., 2021). Nonetheless, in this thesis analysis, the simulation and estimation of the intersystem bias were not included to maintain the simplicity of the clock and instrumental delay modeling.

#### 2.3.7. Multipath Errors

Multipath errors occur when the antenna does not receive the signal from a unique, direct path but from a different, indirect path. When the signal impacts the satellite body or the solar panels, it is reflected

and these reflections arrive with a delay to the receiving antenna. This results in a delay and phase shift of the signal, affecting both pseudorange and carrier phase observations.

The effects of multipath errors are not random and present a temporal pattern that depends on the orientation of the satellite, reflector, and receiver. Several techniques have been proposed to mitigate multipath errors, including the use of specialized antennas and receivers, as well as the placement of the antenna in areas with low signal reflection. In post-processing, weighting the measurements according to their elevation angle can also help to alleviate the effects of these errors (Teunissen & Montenbruck, 2017).

Although the impact of multipath errors is not as significant for space-borne receivers compared to ground-based receivers, they can still introduce errors ranging from 30 to 60 cm and from 6 to 9 mm for ionosphere-free pseudorange and carrier phase observations, respectively (Hauschild & Montenbruck, 2021). To address these errors, a common approach is to let the estimated PCV maps absorb these multipath effects (Conrad et al., 2023). This strategy is particularly effective for satellites without moving parts.

In the context of this thesis, it is assumed that the solar panels remain static, allowing the antenna calibration maps to potentially absorb the multipath effects when they are re-estimated during flight. Hence, for the purpose of this study, multipath errors are not introduced into the GNSS observations.

### 2.3.8. Receiver Thermal Noise

GNSS observations are subject to random errors due to imperfections in the electrical components of the signal processing chain and noise from natural or artificial sources in the environment. The magnitude of these errors depends on the signal-to-noise ratio (SNR) of the signal, which represents the power ratio between the GNSS hardware and environmental background noise. The characteristics of the receiver, such as its bandwidth or chip length, also affect the size of these errors (Teunissen & Montenbruck, 2017). The mathematical modeling of thermal noise errors will be discussed in more detail in Section 5.3.2.

## 2.4. Combinations of Observations

In this section, it is presented how different observations can be combined to eliminate some of the errors previously described. The signals from either one GNSS satellite and one receiver or multiple GNSS satellites and/or receivers can be combined. The latter is typically referred to as differencing. All the information gathered in this section is based on the work of Teunissen and Montenbruck (2017).

The focus is on single-receiver combinations, as they are the types of combinations used in this thesis. The section covers the narrow-lane and wide-lane linear combinations, along with the ionospheric-free combination. Single differences involving two GNSS satellites are also presented since they are used in the Integer Ambiguity Resolution (IAR) scheme explained in Section 4.3.2. Double differences are not discussed here because they will not be employed due to the limited availability of common GNSS satellites in view as the EHI satellites drift apart.

### 2.4.1. Narrow- and Wide-Lane Combinations

Combining two carrier phase observations with different frequencies can lead to different combined frequencies and wavelengths. If the combined wavelength is larger than the largest individual wavelength, the combination is referred to as wide-lane (WL). On the other hand, if the combined wavelength is shorter, then it is a narrow-lane (NL) combination. The combined wavelengths of the most typical dual-frequency wide-lane and narrow-lane combinations are:

$$\lambda_{WL} = \frac{c}{f_A - f_B} \quad (2.5)$$

$$\lambda_{NL} = \frac{c}{f_A + f_B} \quad (2.6)$$

where  $c$  is the speed of light, and  $f_A$  and  $f_B$  are the carrier frequencies of the individual signals. Then, the new carrier phase observations are formed as a linear combination of the individual carrier phase:

$$\Phi_{r,WL}^r = \Phi_{r,A}^s - \Phi_{r,B}^s \quad (2.7)$$

$$\Phi_{r,NL}^r = \Phi_{r,A}^s + \Phi_{r,B}^s \quad (2.8)$$

Wide-lane combinations have a particular use in integer ambiguity resolution, which is the process of finding the integer number of cycles in carrier phase observations. However, they come at the cost of significantly increasing the noise. For instance, the wide-lane combination of GPS L1 and L2 signals presents a noise level of approximately 5.7 times higher than the noise in the individual carrier phase observations.

In addition to phase observations, these combinations can also be applied to pseudoranges. An example is the Melbourne-Wübbena (MW) combination, which is formed from the difference between wide-lane carrier phase observations and narrow-lane pseudorange observations as seen in Equation 2.9. The MW combination can be used to eliminate the first-order ionospheric delay and the geometric effects. It provides a biased estimate of the wide-lane ambiguity, which can be used in the process of ambiguity fixing.

$$MW = \Phi_{r,WL}^s - p_{r,NL}^s \quad (2.9)$$

### 2.4.2. Ionospheric-Free Combination

The ionospheric delay in the GNSS signals can cause significant errors in the positioning calculations. Dual-frequency observations can be used to mitigate the ionospheric effect on GNSS signals. The first-order ionospheric delay can be eliminated using the ionospheric-free (IF) combination, which requires two pseudorange or two carrier phase observations on two different frequencies. The most common IF linear combinations are:

$$p_{r,IF}^s = \frac{f_A^2}{f_A^2 - f_B^2} p_{r,A}^s - \frac{f_B^2}{f_A^2 - f_B^2} p_{r,B}^s \quad (2.10)$$

$$\Phi_{r,IF}^s = \frac{f_A^2}{f_A^2 - f_B^2} \Phi_{r,A}^s - \frac{f_B^2}{f_A^2 - f_B^2} \Phi_{r,B}^s \quad (2.11)$$

However, the noise of these combinations increases by a factor of 3.0 for GPS L1/L2 signals, and by 2.6 for GPS L1/L5 and Galileo E1/E5a signals compared to the noise of single-frequency observations. The noise is higher when the frequency separation is smaller. In this study, the dual-frequency IF combination will be used to eliminate the first-order ionospheric delay.

### 2.4.3. Single Differences

The setup of a single difference observation between two GNSS satellites and one receiver is illustrated in Figure 2.1. This technique involves subtracting the observations coming from one of the GNSS satellites from those coming from the other GNSS satellite, received at the same time and at the same receiver. Notice that the receiver in the figure is depicted on ground, but the same principle applies to a space-borne receiver.

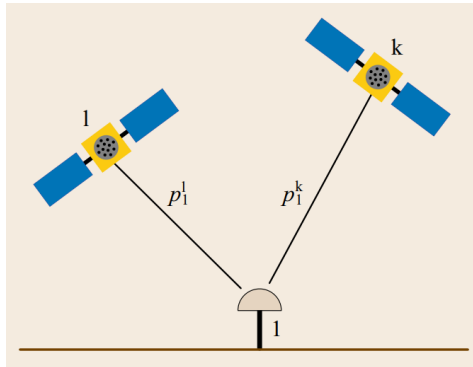


**Figure 2.1:** Single difference of observations from receiver 1 between satellites  $k$  and  $l$  (Teunissen & Montenbruck, 2017).

The combined pseudorange is computed as:

$$p_1^{kl} = p_1^l - p_1^k \quad (2.12)$$

Introducing the extended pseudorange expression in the previous expression leads to:

$$p_1^{kl} = \rho_1^{kl} + cd t^{kl} + c\delta t^{rel,kl} + K_1^{kl} + \xi_1^{kl} + T_1^{kl} + I_1^{kl} + M_1^{kl} + \varepsilon_1^{kl} \quad (2.13)$$

In Equation 2.13, the terms corresponding to the receiver clock offset and its associated relativistic effect correction have been dropped out since they are common for both observations. Similarly, the single-differenced carrier phase is expressed as:

$$\Phi_1^{kl} = \rho_1^{kl} + cdt^{kl} + c\delta t^{rel,kl} + k_1^{kl} + \zeta_1^{kl} + T_1^{kl} - I_1^{kl} + m_1^{kl} + \epsilon_1^{kl} + \lambda^l(\omega_1^l + N_1^l) - \lambda^k(\omega_1^k + N_1^k) \quad (2.14)$$

As with other observation combinations, the process of eliminating parameters from the measurement equations using a single-difference approach also results in an increment of the noise. In particular, the noise of a between-satellite single-differenced observation can be expressed as  $\sigma^{kl} = \sqrt{2}\sigma$ , assuming that the undifferenced observables have the same standard deviation  $\sigma$ .

## 2.5. Relative Navigation with GNSS

Relative navigation refers to the determination of the position of an object with respect to another object considered as the reference. In space-borne applications, a mm-level baseline determination between two satellites can be achieved if carrier phase measurements with fixed integer ambiguities are used for relative positioning. This level of precision is approximately ten times better than what can be achieved using float ambiguity estimation, which typically yields a relative position accuracy of 0.5-1 cm in the best-case scenario (Teunissen & Montenbruck, 2017).

This capability has been demonstrated by different space missions, like Swarm, GRACE, and TerraSAR-X/TanDEM-X (TerraSAR-X add-on for Digital Elevation Measurement). The GRACE mission used a pair of twin satellites to measure the Earth's gravity field with unprecedented accuracy and demonstrated the possibility to obtain 1-mm level baseline precision (Kroes et al., 2005). In the more complex TerraSAR-X/TanDEM-X tandem, a precision of 3-8 mm was achieved for relative positioning (Montenbruck et al., 2011).

The aforementioned missions involve LEO satellites, which significantly differ in their operating conditions compared to a MEO scenario. Firstly, drag is the main perturbing acceleration for a LEO satellite while in MEO drag is practically non-existent and the solar radiation pressure dominates. Furthermore, integer ambiguity resolution can be more challenging for MEO satellites since they have in general less GNSS satellites in common view.

Moreover, it is important to note that these missions present baseline lengths between satellites of no more than a few hundred kilometres, which allows for certain assumptions like similar satellite dynamics. These assumptions do not hold for the EHI constellation under analysis, as its baseline length can reach up to 25,000 km. Precise baseline determination of high-dynamic constellations is a relatively new issue, and there is limited literature on this topic. Some studies, such as Mao et al. (2019b) for the non-pendulum part of the Swarm constellation and Mao et al. (2019a) for the CHAMP (Challenging Minisatellite Payload)/GRACE constellation, have investigated baseline determination for such long-baseline scenarios.

### 2.5.1. Swarm Constellation

The Swarm mission is a three-satellite constellation consisting of two satellites, Swarm-A and Swarm-C, in a pendulum formation, with the third satellite, Swarm-B, at a higher altitude (Friis-Christensen et al., 2006). Figure 2.2 shows a representation of the configuration of the constellation. The distance between Swarm-A and -C is relatively small, allowing for an easier precise relative positioning between the two satellites. Mao et al. (2019b) demonstrated a reduced-dynamic baseline consistency of 1-3 mm for the Swarm-A/C pair, indicating the potential for achieving baseline determination accuracy at the millimetre level.

However, the orbital plane of Swarm-B slowly rotates with respect to those of Swarm-A and Swarm-C, which causes the baseline length to vary between 50 and 3,500 km for both Swarm-B/A and Swarm-B/C pairs. This makes the Swarm constellation a high-dynamic scenario, posing a challenge for precise baseline determination.

Mao et al. (2019b) addressed this challenge by implementing an Iterative Extended Kalman Filter using ambiguity fixing, which showed a reduced-dynamic baseline consistency of 3-5 mm in different directions for the high-dynamic Swarm-B/A and -B/C pairs. The findings of Mao et al. (2019b) demonstrate that the determination of precise baselines is adversely affected as the intersatellite distance increases. Despite this, the study shows that mm-level accuracy can still be achieved for baselines of approximately 3,500 km.

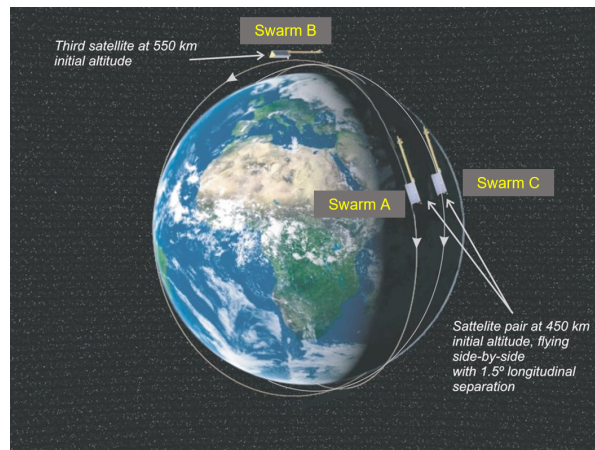


**Figure 2.2:** Illustration of the Swarm constellation (Olsen et al., 2006).

### 2.5.2. CHAMP/GRACE Constellation

Mao et al. (2019a) investigated precise baseline determination for a satellite constellation consisting of two different missions, the CHAMP satellite and the twin GRACE satellites. The baseline between CHAMP and the GRACE tandem varies from 110 km to 7,500 km. The methodology employed in this study is similar to the one used for the previously mentioned Swarm study. Figure 2.3 shows an artist's impression of the CHAMP satellite, while Figure 2.4 presents an artist's concept of the GRACE twin satellites.

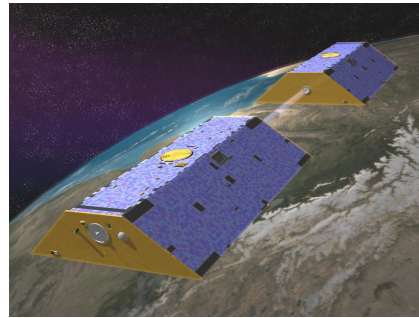
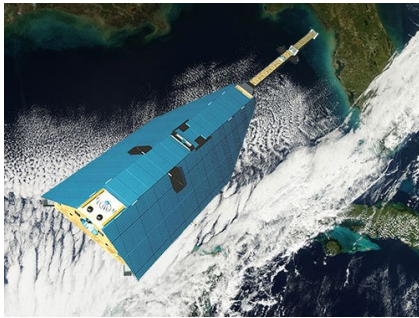


**Figure 2.3:** Artist's impression of CHAMP (Astrium GmbH, n.d.) **Figure 2.4:** Artist's impression of GRACE (NASA/JPL, n.d.)

The results obtained by Mao et al. (2019a) show that the reduced-dynamic/kinematic baseline consistency for the CHAMP/GRACE pairs varies from 0.5 to 2.5 cm. This inconsistency is more pronounced for longer arc lengths due to less common GNSS satellite visibility. The rapidly changing geometry of the constellation poses a challenge for the integer ambiguity resolution process. Nonetheless, ambiguity fixing still improves consistency in the radial, along-track, and line-of-sight directions, although it slightly worsens the cross-track determination. These findings highlight the potential for precise baseline determination in high-dynamic constellations but also emphasize the need for careful consideration of the specific characteristics of each mission.

# Intersatellite Links

Intersatellite Links (ISLs) are a crucial component of modern and future satellite constellations, providing ranging measurements and data communication between satellites. Optical ISLs (OISLs), in particular, offer high-precision ranging measurements that are essential for a wide range of scientific applications. In this chapter, an overview of the available intersatellite ranging technologies is presented, with specific emphasis on optical links. The ISL observable and its primary sources of error are then described. Finally, current and future space missions that employ this type of technology are discussed.

## 3.1. ISL Technology Description

In this section, an exploration of the available technologies for intersatellite ranging is presented, aiming to provide a justification for the selection of the specific ISL used in the EHI constellation. The chosen ISL is a two-way optical link that employs a laser phase ranging technique and features an active transponder architecture. By examining the characteristics and capabilities of various ranging technologies, the rationale behind the adoption of this particular ISL configuration for the EHI mission will be established.

### 3.1.1. Radio Frequency or Optical Intersatellite Links

Intersatellite ranging systems can be divided into two main categories: radio and optical. The frequency band used for ranging determines which category a system belongs to. Although the technology required for radio frequency (RF) ISLs is much more mature than that used in laser/optical ranging, optical intersatellite links provide more accurate measurements at a higher data rate due to their shorter wavelengths. OISL systems offer several advantages over RF ISL systems. Kaushal and Kaddoum (2017) enumerate these advantages:

- High bandwidth. The increase in carrier frequency of optical signals allows them to carry more information, which increases the capacity of the communication system.
- Less power. An optical system typically consumes half of the power of a RF system.
- Less mass. The smaller carrier wavelength of the optical signal enables to achieve the same gain as in a RF system but with a smaller antenna diameter.
- High directivity. Smaller wavelengths translate into a higher directivity and thus an improved gain.
- Unlicensed spectrum. Optical systems are free from spectrum licensing radio regulations, which translates into a decrease of the costs and development time.
- High security. An optical ISL is very directional and hence any dangerous interception will be difficult.

However, OISL technology also has some drawbacks. One of the main limitations of OISL is the requirement for an extremely accurate Acquisition, Tracking and Pointing (ATP) subsystem. The rapid relative motion between the two spacecraft, as is the case in the EHI constellation, makes this tracking process even more complex. Sun et al. (2010) have shown that accurate pointing of the laser beam is critical for the OISL to work properly. Additionally, the optical system performance can be deteriorated due to solar background radiation if the position of the Sun relative to the laser is not optimal, as highlighted by Kaushal and Kaddoum (2017).

The EHI constellation plans to use ISL technology for exchanging data between the two spacecraft and performing ranging measurements. This will enable preliminary filtering of the data on-board, reducing the downlink load and improving the overall system performance. An optical ISL has been selected over a RF ISL as it provides faster and more efficient data transfer, and can possibly meet the demanding relative positioning requirements of this project. In particular, the wavelength proposed for the Event Horizon Imager concept by GMV (2022) is 1064 nm. Thus, the rest of the chapter focuses primarily on optical ISL technologies.

### 3.1.2. Optical ISL Ranging Techniques

Optical ISL ranging techniques can use either pseudorange or phase observables. The main OISL ranging methods currently available are summarized by Gao and You (2006):

- **Laser pulse ranging:** This technique involves sending a pulse from one satellite to another and measuring the time it takes for the pulse to be reflected back. It is commonly used by the International Laser Ranging Service to track satellites from ground. This method provides range measurements with a precision of about one centimetre, which is not sufficient given the EHI mission requirements.
- **Laser phase ranging:** This method calculates the distance between two satellites using the phase delay of the laser signal, typically achieving accuracy below the millimetre-level. The PRISMA (PRecursore IperSpettrale della Missione Applicativa) mission used this kind of ranging method but with radio signals instead of lasers.
- **Laser interferometric ranging:** This technique provides more accurate measurements than the previous two, in the level of nanometres for GRACE-FO (Gravity Recovery and Climate Experiment Follow-On) according to Yang et al. (2014).
- **Laser pulse phase modulation:** The laser pulse is modulated with a single frequency, and the distance is determined by resolving the time difference and phase difference. This method is suitable for measuring very precise distances to kinetic targets. It is intended to be used in the future Laser Interferometer Space Antenna (LISA) mission, where a ranging precision in the pm-level is expected due to phase modulation, according to the preliminary studies by Dornier Satelliten-systeme GmbH (2000).

The first two methods — laser pulse ranging and laser phase ranging — only use code measurements to determine the range. On the other hand, the last two methods — laser interferometric ranging and laser pulse phase modulation — employ carrier phase observations, providing a more accurate measurement of the range.

The chosen technique for the EHI ISL is laser phase ranging. This technique relies only on code observations and does not require the resolution of phase ambiguities, which can be a complex process for small optical wavelengths. It is worth mentioning that GRACE-FO does not require this ambiguity resolution because its goal is to calculate changes in the baseline distance, rather than the absolute baseline length (GMV, 2020).

### 3.1.3. One-Way or Two-Way Ranging

Ranging methods can also be classified as one-way or two-way. In one-way methods, the signal is transmitted from one satellite (the emitter) to the other satellite (the receiver), and the time-of-arrival is measured as the difference between the time of reception and the time of transmission. In contrast, in two-way methods, the signal is sent back by the receiver to the emitter satellite, and the distance is derived from the round-trip time (Laaraiedh et al., 2011). The four previously mentioned ranging techniques can use either one-way or two-way ranging, except for laser pulse ranging which is always two-way.

In one-way ranging, the accuracy of the distance measurement is directly dependant on the quality of synchronization between the emitter and receiver clocks. Thus, it is extremely important to ensure that the clocks on both satellites are accurately synchronized (Alawieh et al., 2016). In addition, if one-way ranging is used, clock biases need to be estimated in the orbit determination process.

Two-way ranging, unlike one-way ranging, does not heavily depend on synchronization between the emitter and receiver. This is because the signal is emitted and received by the same satellite, eliminating the need to estimate clock biases. For this reason, two-way ranging is generally preferred over one-way ranging as it provides greater accuracy (Alawieh et al., 2016).

### 3.1.4. Optical ISL Architecture

When it comes to the architecture of the optical system, there are two options available for two-way links based on how the signal is reflected back. Figure 3.1 illustrates both options, where a) shows a passive retro-reflector architecture, and b) an active transponder architecture.

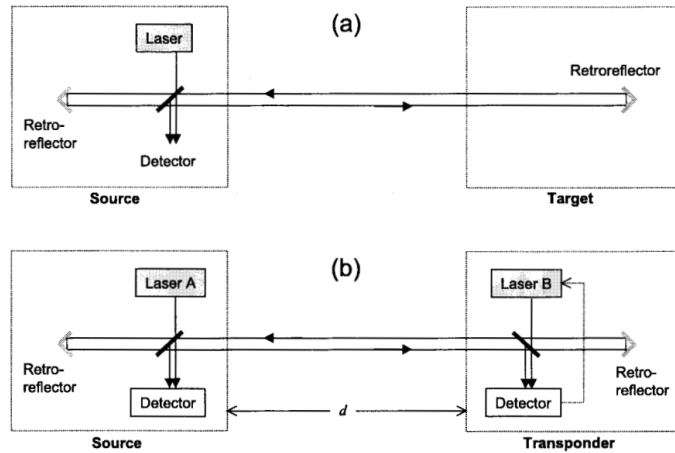


**Figure 3.1:** a) Interferometer with a passive retro-reflector architecture. b) Interferometer with an active transponder architecture (Jeganathan & Dubovitsky, 2000).

The typical approach for the OISL architecture is to install a passive retro-reflector in the receiver satellite, which provides measurements with a resolution better than 1-nm if the relative distance is less than tens of metres. However, as the distance between emitter and receiver increases, it becomes more challenging to get enough optical power back from a passive target. This power loss results in a higher signal-to-noise ratio and thus less accurate measurements (Jeganathan & Dubovitsky, 2000).

Therefore, for larger baseline distances, such as those in the EHI constellation, a passive retro-reflector architecture is not feasible. In such cases, the reflector must be replaced with an active optical transponder, which increases the received optical power and improves the baseline precision (Sheard et al., 2012). As seen in Figure 3.2, the received power decreases with increasing intersatellite range, but at a slower rate for a transponder architecture.

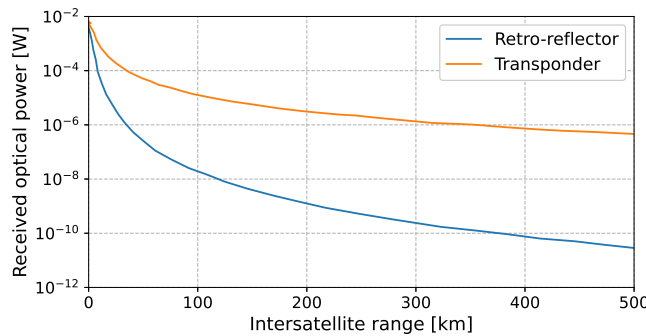


**Figure 3.2:** Received optical power as a function of intersatellite range for both architecture types (Balakrishnan, 2013).

## 3.2. ISL Observation Model

The accuracy of the ISL measurements is essential for the determination of the relative distance between the satellites. To achieve high-precision measurements, it is necessary to model the various error sources that affect the ISL pseudorange observations. This section will describe how the ISL pseudorange observations can be modeled and will provide an overview of the main error sources that affect the measurements of an optical ISL.

### 3.2.1. ISL Observable

In a two-way ranging system, the pseudorange observable can be calculated as half of the round-trip time-of-flight of the signal. This is because the signal is transmitted from the emitter to the receiver and then back to the emitter, as sketched in Figure 3.3. This time-of-flight is then multiplied by the speed of light to obtain the distance traveled by the signal. Equation 3.1 gives the mathematical formulation of this pseudorange calculated at the receiving time (Guindal-Martinez, 2020).

$$p_f(t_r) = \frac{1}{2}c(t_r - t_t) \quad (3.1)$$

where  $p_f$  is the pseudorange at transmission time,  $c$  is the speed of light,  $t_r$  is the receiving time, and  $t_t$  is the transmission time.

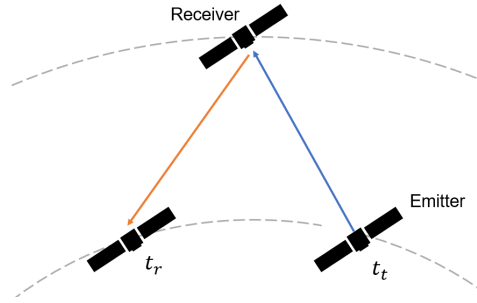


**Figure 3.3:** Sketch of the signal travelled distance in a two-way ISL.

It is important to mention that the pseudorange observable given by Equation 3.1 is not the true range between the satellites, as it is affected by different error sources. Similar to GNSS pseudorange measurements, the errors affecting the ISL pseudorange can be divided into several categories, which will be explained in the following subsection. Equation 3.2 shows how this pseudorange is decomposed into true range, and error sources.

$$p_f = \rho + \Gamma_f \quad (3.2)$$

where  $\rho$  is the true range, and  $\Gamma_f$  is a term that represents all the different errors affecting the measurement.

### 3.2.2. ISL Error Sources

The main error sources and challenges of free space optical intersatellite links have been identified and defined by Kaushal and Kaddoum (2017). Notably, the receiver and emitter clock offsets have not been included in the list of error sources because the two-way range measurement effectively eliminates them. The relevant error sources include:

- Point Ahead Angle (PAA), also known as light-time correction.
- Relativistic effects. In particular, only the Shapiro effect is relevant.
- Atmospheric effects, including both the tropospheric and the ionospheric delays.
- Frequency instability of the clocks.
- Satellite mechanical vibrations.
- Tracking errors, which are caused by disturbances generated by the onboard laser communication instrument. This type of errors include thermal noise, shot noise, and relative intensity noise.
- Background noise due to the radiation of celestial bodies.

The Point Ahead Angle is an effect that arises due to the relative motion between the emitter and transmitter spacecraft. It is caused by the fact that the optical beam is transmitted from the emitter at a time  $t_t$  and received back at a time  $t_r = t_t + \Delta T$ , when the emitter is located at a different position. The magnitude of this delay depends on the relative velocity between the two spacecraft and can be easily corrected. This effect is also known as the light-time correction and is similar to the one that

arises in GNSS. Figure 3.4 depicts this concept for a pair of LEO-GEO satellites, but the same applies to a MEO-MEO pair.

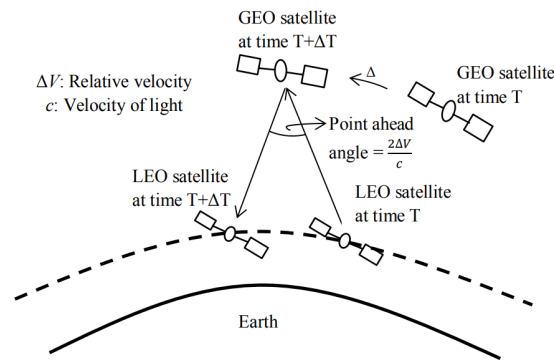


**Figure 3.4:** Concept of PAA in space communication (Kaushal & Kaddoum, 2017).

The relativistic effects influencing an optical signal are analogous to the ones that affect GNSS signals, as described in Section 2.3.1. Two main relativistic effects come into play in OISL measurements. The first one is the Shapiro effect, which results from the space-time curvature caused by the Earth's mass. The other effect is time dilation, which is related to the varying velocity and gravitational potential between the two spacecraft. Nevertheless, the latter effect only affects the clocks and is therefore not relevant for a two-way ranging measurement as it is eliminated.

The optical beam also encounters several losses when propagating through the atmosphere. These losses are related to scattering and absorption, atmospheric turbulence, and beam divergence. The atmospheric effects become more significant as the path of the optical link gets close to the surface of the Earth. A study performed by Loscher (2010) showed that an optical link does not experience any significant interference from the atmosphere for path altitudes greater than 100 km. Hence, by establishing a grazing altitude of 100 km for the EHI's intersatellite link, the atmospheric impact on the pseudorange observable will be negligible.

The remaining error sources — that is, frequency instability, satellite vibrations, tracking errors, and background noise — are challenging to characterize precisely at this stage of the mission. The lack of information about the characteristics of the ISL instrument makes it difficult to develop an accurate model of these effects. As a result, in this study, they are modeled as random white Gaussian noise with a standard deviation similar to state-of-the-art optical ISL precision. It is worth mentioning that this model may be too simplistic, and it might be more realistic to develop a model that accounts for the ISL distance to introduce this noise, as the tracking error depends on this variable (GMV, 2020).

### 3.3. Relative Navigation with ISL

The previous section has shown that some of the error sources present in an optical ISL are difficult to characterize and quantify. The analysis depends on a variety of parameters related to the optical sensor that are not yet fully defined at this early stage of the project. To obtain meaningful information on how to characterize the ISL noise, one approach is to examine space missions that use this technology. The precision level of the instruments on these missions can be used as an indicator of the noise in the range measurements.

There are several missions that use intersatellite links for ranging or communication purposes, such as GRACE, GRACE-FO, PRISMA, and BeiDou-3. Among these missions, GRACE-FO stands out as it employs both a radio ISL and an optical ISL. However, it is worth noting that although the Chinese BeiDou-3 GNSS constellation uses radio ISL, it represents the only ISL mission with MEO spacecraft.

Looking at future missions, LISA and the Kepler system are planning to use optical intersatellite links. LISA is an ESA-led mission that aims to detect gravitational waves, and its optical sensor has been tested by the LISA Pathfinder mission (Amaro-Seoane et al., 2019). The Kepler system, on the other hand, is a concept that is being considered for incorporation into a future generation of Galileo, which would enable all Galileo satellites to be connected via optical ISLs (Giorgi et al., 2019a).

### 3.3.1. GRACE-FO

The Gravity Recovery and Climate Experiment Follow-On (GRACE-FO) mission is composed of a pair of identical satellites used for gravimetry. By measuring the change in the distance between the two spacecraft, the mission is able to detect variations in the Earth's gravitational field (Wuchenich et al., 2014). The separation between the two spacecraft varies between 170 and 270 km, and therefore, to meet the scientific requirements, the range between them needs to be measured with an accuracy of a few micrometres (Kornfeld et al., 2019).

The GRACE-FO mission uses two intersatellite ranging instruments, one of which is the same microwave ranging system employed by its predecessor, GRACE. In addition to this, GRACE-FO also incorporates a technology demonstration of a laser ranging instrument that operates in an active transponder configuration (Sheard et al., 2012). The optical interferometer calculates the round-trip phase variations to determine the change in intersatellite distance (Kornfeld et al., 2019).

Prior to launch, Yang et al. (2014) suggested an expected positioning precision of 50 nm for the GRACE-FO OISL. A subsequent study conducted by Abich et al. (2019) analyzed the in-orbit performance of the laser ranging interferometer and reported a noise level of  $1 \text{ nm}/\sqrt{\text{Hz}}$  at Fourier frequencies above 100 mHz.

The differences between GRACE-FO and the EHI constellation are important to note. Firstly, the GRACE-FO spacecraft operate in LEO orbits, whereas the EHI satellites are located at MEO. Moreover, the baseline distance between the GRACE-FO satellites is a few hundred kilometres, while for the EHIs, it can be as much as 25,000 km. Lastly, the ranging technique of GRACE-FO is based on laser interferometry while the EHIs will employ laser phase ranging, which is less accurate. Based on these differences, it is clear that the analysis of GRACE-FO ranging performance is not directly transferable to the EHI mission. Therefore, assuming an intersatellite ranging noise in the nm-level might be too optimistic.

### 3.3.2. LISA and LISA Pathfinder

The Laser Interferometer Space Antenna (LISA) is a mission consisting of three satellites that aims to detect gravitational waves by measuring the variation in the intersatellite distances. The mission is planned to be launched in the 2030s and will be placed in a heliocentric orbit at a distance of approximately 50 million kilometres from Earth. The three satellites will form an equilateral triangle with a mean intersatellite separation of 2.5 million kilometres (Amaro-Seoane et al., 2019). The orbital configuration of LISA is depicted in Figure 3.5.

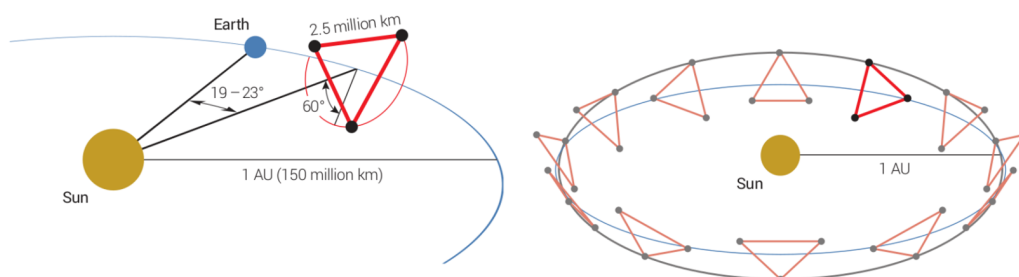


**Figure 3.5:** Orbital configuration of LISA (Amaro-Seoane et al., 2019).

The LISA Pathfinder mission successfully demonstrated several key technologies that will be employed in the upcoming LISA mission (Wanner, 2019). Due to budget constraints, LISA Pathfinder orbited around the first Sun-Earth Lagrangian point on a Lissajous orbit, and it was a single-satellite mission. It carried a precision instrument called the LISA Technology Package (LTP), which included two test masses separated by 38 cm and shielded from external forces such as solar radiation pressure (Racca & McNamara, 2010). The mission achieved an in-orbit noise level of less than  $10 \text{ pm}/\sqrt{\text{Hz}}$  between 1 to 1,000 mHz (Armano et al., 2022).

The EHI constellation and LISA exhibit significant differences. Firstly, their orbital regimes are completely distinct. Moreover, LISA Pathfinder employs an interferometer based on phase measurements,

whereas the EHI's ISL will solely rely on pseudorange observables. Given the differences in orbital conditions and ranging techniques, it may not be realistic to assume a picometre-level ISL ranging noise in this thesis.

### 3.3.3. BeiDou-3

The third-generation BeiDou satellites, also known as BeiDou-3, include ISL payloads that provide Ka-band microwave, single-frequency, one-way pseudorange ranging measurements. This allows for improved orbit accuracy compared to the orbits obtained using solely L-band measurements from a regional network of tracking stations (Tang et al., 2018).

Yang et al. (2020) conducted an analysis of the ISL-enhanced orbit determination for eight MEO BeiDou-3 satellites. The study revealed that the ISL measurement noise ranged from approximately 1 to 3 cm, and the ranging accuracy was about 6 cm. Similarly, Tang et al. (2018) and Bai et al. (2020) reported a ranging noise level in the centimetre range. Furthermore, Zhu et al. (2022) combined ISL and ground-based measurements in a POD analysis and demonstrated that the ISL payloads on BeiDou-3 satellites enhance the performance of the system, even at large baselines.

The ranging technology employed by BeiDou-3 differs fundamentally from that of the EHI constellation. BeiDou-3 uses one-way radio signals, whereas the EHIs intend to use two-way optical signals, which offer more precise measurements. The centimetre-level ISL precision demonstrated by BeiDou-3 can therefore be considered as an upper bound for the expected accuracy of the ISL in the EHIs.

### 3.3.4. Kepler System

The Kepler system is a novel concept designed to enhance the performance of future GNSS architectures, with a specific focus on the next generation of Galileo. It comprises 24 MEO satellites, placed in the same orbits as the current Galileo satellites, and six LEO satellites, located at an altitude of approximately 1,200 km. Each satellite in the Kepler architecture is equipped with three optical terminals that facilitate two-way laser links between the satellites. In particular, each MEO satellite is continuously connected to its two neighbouring MEO satellites within the same orbital plane, as well as to a LEO satellite. In contrast, each LEO satellite is linked to three MEO satellites, which are positioned in different orbital planes (Giorgi et al., 2019a). Figure 3.6 provides a visual representation of the Kepler system.

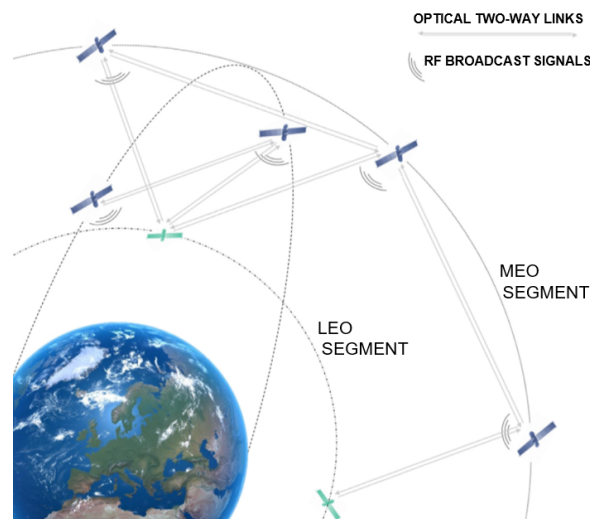


**Figure 3.6:** Kepler constellation architecture, with MEO and LEO satellites interconnected via two-way laser links (Giorgi et al., 2019a).

The optical intersatellite links proposed for Kepler are coherent optical links with a ranging target performance of 300  $\mu\text{m}$ . The first laboratory tests conducted by Mata-Calvo et al. (2020) have shown promising results with a standard deviation of 15  $\mu\text{m}$  for filtered range estimation. Nevertheless, this experiment was conducted in a static environment with masses separated only by 30 m. Future work

will focus on verifying this accuracy in a dynamic closed loop scenario that emulates satellite movement, which is expected to introduce additional challenges.

The studies conducted by Giorgi et al. (2019b), Michalak et al. (2020), and Michalak et al. (2021) present a less optimistic view regarding the ranging accuracy of the optical ISLs in the Kepler system. In their simulations, these studies assumed a Gaussian noise of 1 mm in the optical range measurements. On top of that, Michalak et al. (2020) and Michalak et al. (2021) explored the inclusion of range biases in the laser observations. The results indicated that small biases of up to 5 mm still allowed for POD with sub-centimetre radial accuracy. However, as the biases increased up to 20 mm, the accuracy deteriorated. This level of accuracy is consistent with the findings of Schlicht et al. (2020), who assumed that the ISL biases in the Kepler constellation were randomly distributed between -0.5 and 0.5 mm.

In summary, the noise assumed for the optical ISLs of the Kepler system is generally around 1 mm, which is significantly larger than the noise levels offered by GRACE-FO and LISA Pathfinder. Given the similarities between the Kepler system and the EHI constellation in terms of laser ranging technique and orbital conditions, the estimated noise level of 1 mm in the Kepler ISLs could provide a more realistic estimate for the expected noise level in the ISL of the EHI mission.

# Precise Orbit Determination

The determination of satellite orbits is a fundamental aspect of space missions, allowing to accurately obtain the position and velocity of a satellite. While the point mass force of the Earth is the primary factor affecting the motion of an Earth-orbiting satellite, other forces such as atmospheric drag and solar radiation pressure cannot be ignored in general. These forces define the equation of motion for the satellite, which can be integrated to determine the state of the satellite at any given time. However, the initial position and velocity of the satellite are never known exactly, and physical constants of the forces can only be approximated, causing errors in the predicted motion (Tapley et al., 2004).

The process of determining the best estimate of the state of the satellite from observations influenced by random and systematic errors is known as state estimation, or orbit determination (OD) (Tapley et al., 2004). In particular, Precise Orbit Determination (POD) requires that the orbit is known with an accuracy well below one metre. In the most demanding and challenging cases, this precision is even reduced to just a few centimetres (GMV, 2013).

POD can be approached using different techniques, including kinematic, dynamic, or reduced-dynamic methods. The kinematic approach only considers the observations and does not take into account the satellite dynamics. In contrast, the fully dynamic technique combines the satellite dynamics and noisy instantaneous measurements. The reduced-dynamic method, which is the selected approach for the simulations in this thesis, employs both the processed observations and the dynamic model to enhance the orbit solution (Wu et al., 1991).

Furthermore, POD can be performed using either batch or sequential estimators. The Weighted Least Squares (WLS) algorithm is the most common batch estimator used in post-processing, while the Kalman filter is the sequential estimator typically employed for real-time applications. In this thesis, WLS is the selected estimator as the focus is on post-processing. More information about this algorithm can be found in Appendix A.

The chapter begins by presenting the most relevant reference frames used in this thesis. Afterwards, the dynamical model is explained in detail, making particular emphasis on the solar radiation pressure as it is the main perturbing acceleration at MEO altitude. Finally, the chapter ends with an explanation of the Integer Ambiguity Resolution (IAR) problem, which is the process of estimating the unknown integer number of cycles in the carrier phase observations.

## 4.1. Reference Frames

In the context of orbit determination, several reference frames are defined to represent the motion of satellites in space. In this section, the three most important frames used in the EHI mission will be described: the Geocentric Celestial Reference Frame (GCRF), the radial/along-track/cross-track QSW frame, and the ISL-SGRA frame. The definitions of each frame, their importance for the mission, and the mathematical expressions defining their axes will be explained.

### 4.1.1. GCRF Reference Frame

The Geocentric Celestial Reference Frame (GCRF) is an inertial reference frame, whose origin is located at the centre of mass of the Earth. The axes of this frame are defined relative to distant extragalactic objects, ensuring its inertial nature (Capitaine et al., 2000; Petit & Luzum, 2010). The GCRF is considered quasi-inertial because the centre of the Earth is accelerating in its orbit around the Sun. However, this acceleration is typically negligible for most POD applications.

### 4.1.2. QSW Reference Frame

The QSW frame is a local coordinate system that is based on the satellite orbit itself. The origin of this system is located at the centre of mass of the satellite. The Q axis, which is also known as the radial axis, points from the centre of the Earth towards the satellite. The S axis, which is named along-track, is defined inside the orbital plane and is perpendicular to the radial axis. Finally, the W axis, which is called the cross-track, is normal to the orbital plane and thus perpendicular to both the Q and S axes (Chen et al., 2017). The QSW frame is also referred to as the RSW frame. The mathematical definition of these axes is presented in Equation 4.1, and a graphical representation is given in Figure 4.1.

$$\hat{Q} = \frac{\mathbf{r}}{|\mathbf{r}|}, \quad \hat{W} = \frac{\mathbf{r} \times \mathbf{v}}{|\mathbf{r} \times \mathbf{v}|}, \quad \hat{S} = \hat{W} \times \hat{Q} \quad (4.1)$$

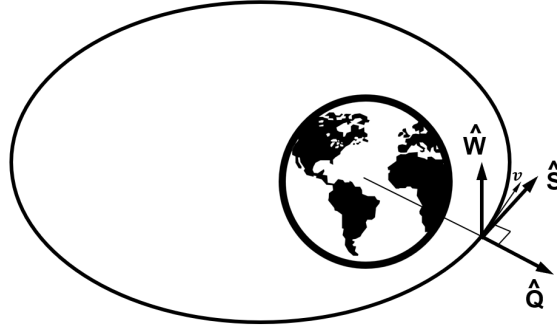


Figure 4.1: Representation of the QSW reference frame.

This frame is particularly useful for studying the accelerations that affect the motion of the spacecraft in the radial, along-track and cross-track directions. For example, the gravitational attraction of the Earth points in the negative radial direction. By defining the QSW frame, the dynamics of the spacecraft can be more easily analyzed and modeled.

### 4.1.3. ISL-SGRA Reference Frame

Another frame of interest for this project is the ISL-SGRA frame, which is defined based on the baseline between EHI-1 and EHI-2 and the attitude of the spacecraft. In this frame, the X axis aligns with the baseline direction, pointing from EHI-1 to EHI-2, while the Y axis points towards the black hole Sagittarius A\*. The Z axis is orthogonal to both X and Y. However, it should be noted that this frame is not orthogonal since X and Y are non-orthogonal.

A schematic representation of the ISL-SGRA coordinate system can be observed in Figure 4.2. It is important to clarify that the depicted EHI orbits in Figure 4.2 are not an accurate representation of the actual orbits but have been simplified for illustrative purposes. The axes of the ISL-SGRA frame are defined as follows:

$$\hat{X} = \frac{\mathbf{r}_2 - \mathbf{r}_1}{|\mathbf{r}_2 - \mathbf{r}_1|}, \quad \hat{Y} = \frac{\mathbf{r}_{\text{SGRA}}}{|\mathbf{r}_{\text{SGRA}}|}, \quad \hat{Z} = \hat{X} \times \hat{Y} \quad (4.2)$$

where  $\mathbf{r}_1$ ,  $\mathbf{r}_2$ , and  $\mathbf{r}_{\text{SGRA}}$  represent the inertial position vectors of EHI-1, EHI-2, and Sagittarius A\*, respectively.

The ISL-SGRA reference frame plays a crucial role in the analysis conducted in this study, providing a consistent coordinate system for various measurements and computations. This frame incorporates the two key axes of the problem. Firstly, the baseline direction, aligned with the ISL observations, holds special significance since previous studies have demonstrated that the ISL enhances GNSS navigation accuracy primarily in the baseline direction (GMV, 2022; Guindal-Martinez, 2020). Secondly, defining an axis that points towards Sagittarius A\* is vital for the success of the EHI mission because achieving high-quality images of the black hole requires a precise determination of the baseline distance in this specific direction.

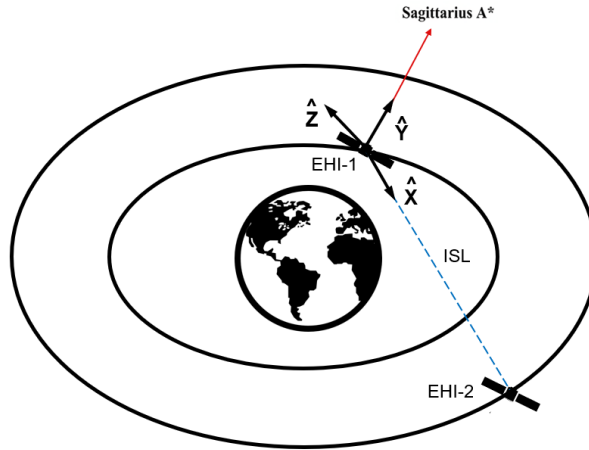


Figure 4.2: Representation of the ISL-SGRA reference frame.

## 4.2. Dynamic Model

The gravitational attraction of the Earth is the primary factor in determining the orbit of a satellite around the Earth. In the case where the Earth is considered a perfect sphere with homogeneous mass distribution, the resulting satellite orbit is a conic section known as a Keplerian orbit and the equation that describes its motion is the two-body equation (Curtis, 2014).

In reality, the motion of a satellite is affected by various perturbations that cause its trajectory to deviate from a Keplerian orbit. These perturbations can include the non-sphericity of the Earth, atmospheric drag, solar radiation pressure, and gravitational attraction of other celestial bodies (Curtis, 2014). To take into account these perturbations in the dynamic model, a perturbing term is added to the right-hand side of the typical two-body equation:

$$\ddot{\mathbf{r}} = -\mu \frac{\mathbf{r}}{r^3} + \mathbf{p} \quad (4.3)$$

where  $\mu$  is the gravitational parameter of the Earth,  $\mathbf{r}$  is the geocentric inertial position of the satellite, and  $\mathbf{p}$  represents the total effect of all the perturbing accelerations.

In Figure 4.3, the magnitude of the main perturbing accelerations as a function of the orbital radius is shown. The nominal radius of the orbits of EHI-1 and EHI-2 is represented by the red vertical line. It is clear from this figure that atmospheric drag no longer plays a role at a low MEO altitude regime and, therefore, it will not be considered in the dynamical model of the EHIs. Additionally, it can be observed that the importance of the geopotential decreases rapidly with increasing altitude. At the altitude of the EHIs,  $J_{18,18}$  is less significant than the third-body effects of Venus and Jupiter.

In order to achieve high-precision orbit determination, it is essential to employ a highly accurate dynamic model that accounts for the main perturbations. These perturbations include:

- The gravitational acceleration of the Earth, taking into account the non-sphericity and non-uniform mass distribution of the Earth.
- The third-body gravitational accelerations.
- The solar radiation pressure.
- The Earth's infrared radiation.
- The Earth's albedo.
- Solid and ocean tides.
- Polar tides.
- Relativistic effects.

Despite the inclusion of the previous perturbations in the dynamical model, there are still some remaining dynamic model errors. This can be due to either the mismodeling of the perturbations that are being considered or the presence of other perturbations that have not been accounted for, such as

the influence of thermal forces. These unmodeled effects can lead to uncertainties in the dynamical model, which in turn affect the accuracy of the orbit determination solution.

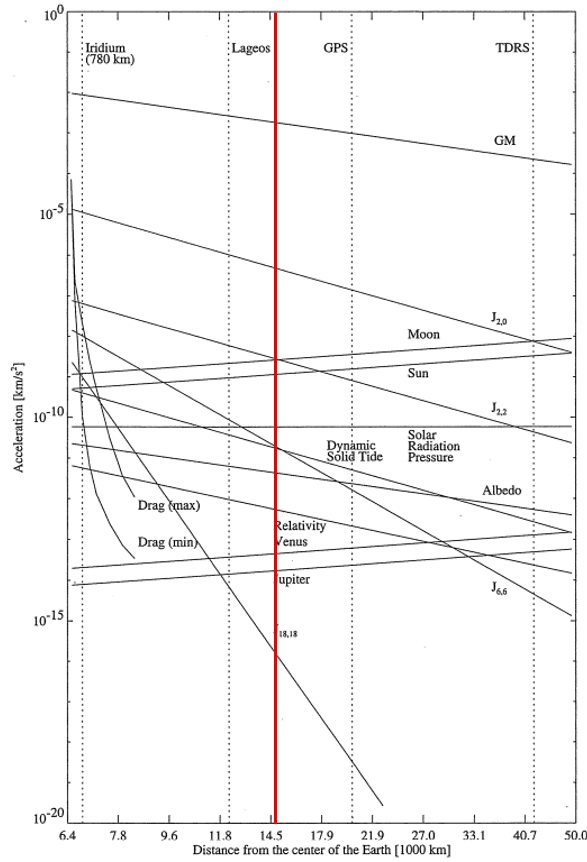


**Figure 4.3:** Order of magnitude of various perturbations of a satellite orbit as a function of the radius of the orbit (Montenbruck & Gill, 2000). The red line represents the nominal radius of the orbits of the EHI satellites.

#### 4.2.1. Gravity of the Earth

The Earth is not a perfect sphere but an oblate spheroid with non-uniform mass distribution. To mathematically describe the full Earth's gravity potential, a common approach is to use a spherical harmonic expansion, which involves decomposing the potential into a series of harmonic functions (Montenbruck & Gill, 2000):

$$U = \frac{\mu}{r} \sum_{n=0}^{\infty} \sum_{m=0}^n \frac{R^n}{r^n} P_{nm}(\sin \phi) (C_{nm} \cos(m\lambda_L) + S_{nm} \sin(m\lambda_L)) \quad (4.4)$$

where  $U$  is the Earth's gravity potential,  $\mu$  is the gravitational parameter of the Earth,  $R$  is the mean Earth equatorial radius,  $r$  is the geocentric orbital radius,  $\phi$  is the geocentric latitude,  $\lambda_L$  is the geographic longitude,  $C_{nm}$  and  $S_{nm}$  are constant model parameters, and  $P_{nm}$  are the associated Legendre polynomials of degree  $n$  and order  $m$ .

#### 4.2.2. Third-Body Forces

Third-body perturbations refer to the gravitational effects of other celestial bodies on the motion of the satellite around the Earth. Assuming that the celestial bodies are point masses, the total acceleration exerted on the satellite can be expressed as (Wakker, 2015):

$$\ddot{\mathbf{r}}_{3B} = \sum_{k=1}^n \mu_k \left[ \frac{\mathbf{r}_k - \mathbf{r}}{|\mathbf{r}_k - \mathbf{r}|^3} - \frac{\mathbf{r}_k}{|\mathbf{r}_k|^3} \right] \quad (4.5)$$

where  $\ddot{r}_{3B}$  is the net third-body acceleration,  $n$  is the total number of celestial bodies,  $\mu_k$  is the gravitational parameter of body  $k$ ,  $r_k$  is the position vector from body  $k$  to Earth, and  $r$  is the geocentric position of the satellite.

### 4.2.3. Solid, Ocean and Pole Tides

Due to the non-rigid nature of the Earth, the gravitational attraction of other celestial bodies — mainly the Sun and Moon — causes a deformation of the Earth. This deformation produces a redistribution of the Earth's crust and water masses in the oceans, resulting in solid and ocean tides, respectively. Furthermore, the asymmetrical mass distribution of the solid Earth and oceans leads to a precession and nutation of the rotation axis of the Earth, causing pole tides (Tapley et al., 2004).

These tidal forces cause the harmonic coefficients in Equation 4.4, specifically  $C_{nm}$  and  $S_{nm}$ , to vary with time, making them non-constant. The solid tides contribution to  $C_{nm}$  and  $S_{nm}$  can be expressed in terms of the Love number, while the dynamical effect of ocean tides can be incorporated as periodic variations in these coefficients. The detailed procedure for calculating these time-varying corrections is provided by Petit and Luzum (2010).

### 4.2.4. Solar Radiation Pressure

Solar radiation pressure (SRP) is the main non-gravitational effect that influences the dynamics of a MEO satellite. It arises from the pressure exerted on the satellite by photons emitted by the Sun, which produces a non-negligible acceleration. The magnitude of the SRP acceleration depends on the particular geometry, orientation, and surface optical properties of the satellite (Teunissen & Montenbruck, 2017).

The modeling of solar radiation pressure can be approached in two ways, with analytical or empirical models. Analytical models are based on the physics of the problem and the satellite's structure and surface properties. These models aim to describe the physical reality of the problem through mathematical expressions that depend on the geometrical properties of the system, satellite characteristics, and universal constants. However, the complexity of the physical reality makes it difficult to accurately capture the real behaviour of the problem (Rodríguez-Solano et al., 2012). Two examples of analytical models are the cannonball model and the box-wing model.

Empirical models, on the other hand, estimate the acceleration through a set of coefficients. These models do not try to mathematically represent the physics of the problem. Instead, they rely solely on observations to estimate the effects of solar radiation pressure. Nevertheless, this loss of physical understanding can lead to non-physical orbits and the introduction of undesired systematic errors (Rodríguez-Solano et al., 2012). An example of an empirical model is the ECOM (Empirical CODE Orbit Model). It is also possible to employ an a priori analytical model to enhance the performance of the empirical model, these are the so-called hybrid models.

In the context of this thesis, the analytical box-wing model and the ECOM model are used. The analytical box-wing model is chosen due to its simplicity, as the precise geometry of the EHI spacecraft is still uncertain at this stage. The ECOM model will also be employed as an alternative approach to capture the solar radiation pressure effects.

#### 4.2.4.1. Box-Wing Model

The box-wing model is a type of analytical panel model that decomposes the satellite into a central box-like structure and solar panels attached to it. In constructing this model, the following assumptions described by Rodríguez-Solano et al. (2012) are made:

- The satellite structure can be approximated by a box shape and flat solar panels.
- Smaller structures, like antennas or engines, contribute to the effective area but their shape is not considered.
- Forces due to internal heat generation cancel from opposite surfaces.
- Shadowing or re-reflection from one surface to another are not considered.
- Heating and cooling effects are neglected.
- The dimensions and mass of the satellite are known.

The mathematical expression for the SRP acceleration  $\ddot{\mathbf{r}}_{\text{SRP}}$  exerted on each surface can be described using Equation 4.6.

$$\ddot{\mathbf{r}}_{\text{SRP}} = -\nu P_{\odot} C_R \frac{A}{m_{\text{sat}}} \frac{1 \text{AU}^2}{r_{\odot}^2} \cos \theta [(1 - \varepsilon) \mathbf{e}_{\odot} + 2\varepsilon \cos \theta \mathbf{n}] \quad (4.6)$$

where  $P_{\odot}$  is the solar radiation pressure at 1 AU from the Sun,  $A$  is the satellite's cross-sectional area,  $m_{\text{sat}}$  is the satellite's mass,  $r_{\odot}$  is the geocentric vector of the Sun, and  $C_R$  is the radiation pressure coefficient which is typically estimated. This coefficient depends on the optical properties of the satellite surfaces according to  $C_R = 1 + \varepsilon$ , where  $\varepsilon$  is the surface reflectivity. Moreover,  $\mathbf{e}_{\odot}$  is the unit vector in the direction Earth-Sun and  $\mathbf{n}$  is the unit vector perpendicular to the surface. In this way,  $\theta$  is the angle between these two vectors. Lastly,  $\nu$  is the shadow function, such that  $\nu = 0$  if the satellite is in umbra,  $\nu = 1$  if the satellite is in sunlight, and  $0 < \nu < 1$  if the satellite is in penumbra (Montenbruck & Gill, 2000).

#### 4.2.4.2. ECOM

The Empirical CODE Orbit Model (ECOM) is an empirical SRP model developed by the Center for Orbit Determination in Europe (CODE). ECOM decomposes the perturbing SRP acceleration into three orthogonal directions that are well-adapted to SRP modeling (Arnold et al., 2015). These directions are:

$$\mathbf{e}_D = \frac{\mathbf{r}_{\odot} - \mathbf{r}}{|\mathbf{r}_{\odot} - \mathbf{r}|}, \quad \mathbf{e}_Y = -\frac{\mathbf{e}_r \times \mathbf{e}_D}{|\mathbf{e}_r \times \mathbf{e}_D|}, \quad \mathbf{e}_B = \mathbf{e}_D \times \mathbf{e}_Y \quad (4.7)$$

where  $\mathbf{r}_{\odot}$  and  $\mathbf{r}$  are the geocentric vectors of the Sun and the satellite, respectively, and  $\mathbf{e}_r$  is the unit vector associated with  $\mathbf{r}$ . Therefore,  $\mathbf{e}_D$  is the unit vector pointing in the direction satellite-Sun,  $\mathbf{e}_Y$  is perpendicular to the plane satellite-Sun-Earth, and  $\mathbf{e}_B$  completes the right-handed orthogonal reference system. It is worth noting that the  $\mathbf{e}_Y$  direction aligns with the solar panel axis if the satellite follows a yaw-steering attitude law. Figure 4.4 shows the Sun-satellite-Earth reference frame illustrating the orientation of the D, Y, and B axes.

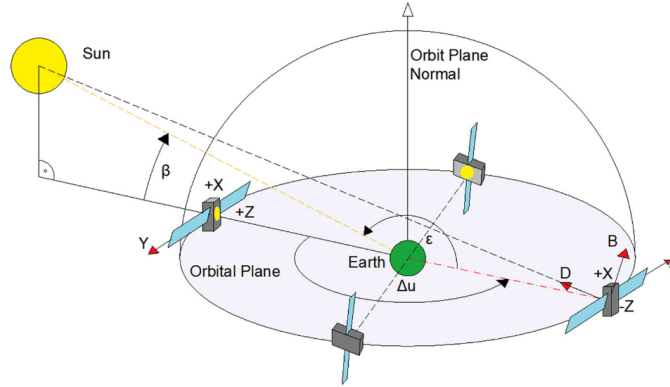


**Figure 4.4:** Sun-satellite-Earth reference frame illustrating the D, Y, and B directions (Bury et al., 2020).

Expressing each acceleration component as a truncated Fourier series expansion with respect to the satellite's argument of latitude  $u$ , the total SRP acceleration can be written as:

$$\mathbf{a} = \mathbf{a}_{\text{appr}} + D(u)\mathbf{e}_D + Y(u)\mathbf{e}_Y + B(u)\mathbf{e}_B \quad (4.8)$$

in which  $\mathbf{a}_{\text{appr}}$  is the acceleration coming from a selectable a priori analytical model. If the model is purely empirical, then no a priori model is used and thus  $\mathbf{a}_{\text{appr}} = \mathbf{0}$  (Arnold et al., 2015).

These  $D$ -,  $Y$ - and  $B$ -coefficients are estimated during the orbit determination process. In the original ECOM,  $D(u)$ ,  $Y(u)$  and  $B(u)$  are truncated after the once-per-revolution terms:

$$\begin{aligned} D(u) &= D_0 + D_c \cos u + D_s \sin u \\ Y(u) &= Y_0 + Y_c \cos u + Y_s \sin u \\ B(u) &= B_0 + B_c \cos u + B_s \sin u \end{aligned} \quad (4.9)$$

#### 4.2.4.3. Modified ECOM: ECOM-SGRA

The standard ECOM model previously presented is specifically designed for satellites that follow a yaw-steering attitude law, where the Y axis aligns with the solar panels. Therefore, it cannot be expected to accurately represent the behaviour of satellites following different attitude laws (Prange et al., 2017). In particular, for satellites employing an Orbit-Normal (ON) attitude law — such as BeiDou-2 IGSO and MEO, and BeiDou-3 — several studies have developed strategies to address this attitude-related issue.

In the ON mode, the satellite-fixed reference frame axes are defined as follows: the Z axis points radially towards the Earth, the X axis points along the along-track direction, and the Y axis is perpendicular to the orbital plane, completing the right-hand reference frame (Zhao et al., 2022). Figure 4.5 provides a visual representation of these axes in the ON mode.

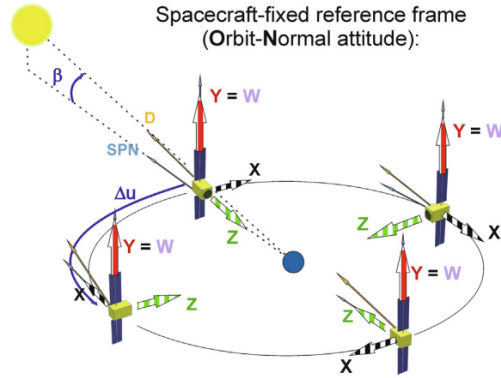


**Figure 4.5:** Representation of the satellite-fixed reference frame axes in the Orbital-Normal attitude mode (Prange et al., 2020).

In order to use the ECOM model in the ON mode, Prange et al. (2020) have developed a series of empirical SRP models, similar to ECOM, specifically tailored for satellites in the ON mode. These modified models redefine the Y and B axes of the standard ECOM model to better capture the influence of the attitude of the satellite. The new reference frame, known as the terminator frame (TERM), is characterized by three directions:  $T_1$ ,  $T_2$ , and  $T_3$ . In this frame,  $T_3$  points towards the Sun,  $T_1$  is perpendicular to both the satellite-Sun direction and the normal of the orbital plane, and  $T_2$  completes the orthogonal reference system. These axes are then defined as follows:

$$e_{T_1} = \frac{e_D \times e_n}{|e_D \times e_n|}, \quad e_{T_2} = e_{T_3} \times e_{T_1}, \quad e_{T_3} = e_D \quad (4.10)$$

where  $e_n$  represents the direction normal to the orbital plane, which coincides with the solar panel axis in the ON mode. Figure 4.6 provides a visual representation of the axes within the TERM coordinate system.

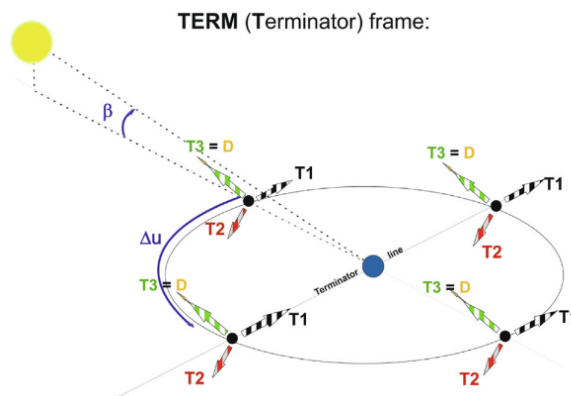


**Figure 4.6:** Representation of the TERM frame (Prange et al., 2020).

The EHI spacecraft deviate from both the yaw-steering and orbital-normal attitude laws and instead follow an inertial attitude law, aligning themselves with the black hole Sagittarius A\*. Although the ECOM model was originally adapted for the ON attitude mode, it served as an inspiration to develop a modified ECOM system suitable for the EHI attitude law. In this modified frame, the D axis remains aligned with the satellite-Sun direction. The Y axis is redefined as perpendicular to both D and the direction pointing towards the black hole, while the B axis completes the orthogonal frame. This new frame, referred to as ECOM-SGRA, is defined by the following directions:

$$\mathbf{e}_{\tilde{D}} = \mathbf{e}_D = \frac{\mathbf{r}_{\odot} - \mathbf{r}}{|\mathbf{r}_{\odot} - \mathbf{r}|}, \quad \mathbf{e}_{\tilde{Y}} = \mathbf{e}_{\tilde{D}} \times \mathbf{e}_{SGRA}, \quad \mathbf{e}_{\tilde{B}} = \mathbf{e}_{\tilde{D}} \times \mathbf{e}_{\tilde{Y}} \quad (4.11)$$

where  $\mathbf{e}_{SGRA}$  is the direction pointing towards Sagittarius A\*.

It is important to note that no existing literature was found on adapting the ECOM model to attitude laws other than the ON mode. Hence, one of the objectives of this thesis is to evaluate whether using the ECOM-SGRA model, instead of the standard ECOM model, for SRP modeling yields more physically accurate results and improves orbit accuracy.

#### 4.2.5. Earth Albedo and Infrared Radiation

Direct solar radiation is not the only source of radiation that affects the motion of a satellite. The Earth's infrared radiation (IR) and albedo should also be considered in POD applications. Albedo is the solar radiation that impacts the Earth and is immediately reflected back onto the satellite. This reflected radiation constitutes about 30% of the incoming solar radiation. The remaining solar radiation that is absorbed and re-emitted later is referred to as infrared radiation. It is worth mentioning that the radiation from other celestial bodies such as the Moon is typically not significant enough to affect Earth-orbiting satellites and therefore does not need to be considered (Vallado, 2001).

Earth's albedo and IR travel differently through the atmosphere because they have different wavelengths. Thus, they are separated into two different effects. To model these effects, the formulas presented in the previous subsection for SRP can be modified to account for the IR or albedo pressures. A box-wing model is used in this thesis to model the effect of IR and albedo radiation, and the resulting acceleration is computed by summing the accelerations induced on each component of this macro-model.

#### 4.2.6. Relativistic Effects

The motion of a satellite should be described according to the principles of general relativity. There are three main relativistic effects: the Schwarzschild effect, the Lense-Thirring effect, and the de Sitter effect. The Schwarzschild effect results in a secular shift in the argument of perigee, while the Lense-Thirring and de Sitter effects cause precession of the orbital plane. For high orbits, the magnitude of the Lense-Thirring and de Sitter precession is around two or three orders lower than the magnitude of the Schwarzschild effect (Petit & Luzum, 2010).

If only the Schwarzschild effect is considered, as is the case in this thesis, the relativistic correction to the acceleration of a satellite can be expressed as:

$$\ddot{\mathbf{r}}_{rel} = \frac{\mu}{c^2 r^3} \left[ \left( \frac{4\mu}{r} - \mathbf{v} \cdot \mathbf{v} \right) \mathbf{r} + 4 (\mathbf{r} \cdot \mathbf{v}) \mathbf{v} \right] \quad (4.12)$$

where  $\mu$  is the gravitational parameter of the Earth,  $c$  is the speed of light, and  $\mathbf{r}$  and  $\mathbf{v}$  are the geocentric position and velocity of the satellite (Petit & Luzum, 2010).

#### 4.2.7. Dynamical Model Uncertainties

Imperfections in the non-conservative force models pose a major challenge to POD applications. Even the most detailed satellite models are limited by uncertainties of the time-varying orientation, material properties, and surface temperatures (Montenbruck & Gill, 2000). In addition to these challenges, there are other non-gravitational forces that can impact the satellite and are typically not modeled. For example, the heating of satellite components by the Sun and the Earth can produce an unsymmetrical thermal distribution, which will create a thermal force (Tapley et al., 2004).

In certain contexts, empirical accelerations may be incorporated into the equations of motion to account for unknown forces or errors. A common method for modeling these empirical accelerations is

through Cycle-Per-Revolution (CPR) accelerations, where the periodicity of the error is equal to the orbital period. As per Montenbruck and Gill (2000), the CPR empirical acceleration can be mathematically represented as:

$$\ddot{\mathbf{r}}_{emp} = \mathbf{E}(\mathbf{a}_0 + \mathbf{a}_1 \sin \theta + \mathbf{a}_2 \cos \theta) \quad (4.13)$$

where  $\mathbf{a}_0$  are the constant coefficients, while  $\mathbf{a}_1$  and  $\mathbf{a}_2$  are the sine and cosine coefficients, and  $\theta$  is the true anomaly. It is a common practice to express the empirical acceleration in the local QSW frame. Hence, the acceleration must be transformed into the inertial reference system using the corresponding rotation matrix  $\mathbf{E}$ .

The estimation of CPR coefficients is a critical step in the orbit determination process. These coefficients are determined during the solution of the least-squares problem and may vary significantly from orbit to orbit, or even during a single orbit due to changes in the satellite's environment. To account for these variations, a common approach is to divide the orbital arc into sub-intervals and estimate a different set of CPR coefficients for each sub-interval. Nevertheless, selecting the optimal number of sub-intervals can be a challenge as it largely depends on the specific problem at hand.

### 4.3. Integer Ambiguity Resolution

POD typically relies on carrier phase measurements to estimate satellite orbits with high accuracy. The use of carrier phase measurements requires estimating the phase ambiguity to obtain the correct phase measurements. In high-precision applications, it is also crucial to resolve the integer nature of the ambiguity, which can be achieved through a process called Integer Ambiguity Resolution (IAR). Once the carrier phase ambiguities have been fixed, the carrier phase measurement behaves like a very precise pseudorange.

When fixing the ambiguity, the observation equations of the orbit determination problem include both real and integer unknown parameters, forming a mixed-integer problem. This problem can be solved using the steps outlined by Teunissen and Montenbruck (2017):

1. Float solution: the integer nature of the ambiguities is ignored, and a regular parameter estimation is performed with all unknowns treated as real numbers.
2. Integer solution: a mapping is introduced to transform the float ambiguities to integer values. There are several mappings available, including integer rounding, integer bootstrapping, and integer least-squares.
3. Accept/reject integer solution: a test is performed to check if the integer solution can be accepted as valid. If the test indicates that the integer solution is not valid, the integer solution is rejected and the float solution is chosen instead.
4. Fixed solution: the ambiguity residual, which represents the difference between the observed and computed carrier phase measurements, is used to recompute the unknowns obtained in the float solution step. This results in a new set of estimated parameters that includes integer ambiguities. The ambiguity test is performed again to check if the fixed solution can be accepted or if another iteration is needed. This iterative procedure continues until a valid integer solution is obtained or a maximum number of iterations is reached.

#### 4.3.1. Integer Ambiguity Resolution Strategies

The ambiguity parameter loses its integer nature when the instrumental delays in both the transmitter and receiver are not estimated or removed from the equations. The float ambiguities absorb these delays and, as a result, the inherent accuracy of carrier phase measurements is not fully exploited. Other signal delays, such as antenna phase centre variations, also contribute in a lesser extent to this fractional part of the ambiguity. To overcome this limitation, differential observations are commonly used to remove the fractional part and recover the integer ambiguities (Zhang et al., 2021).

There are two principal methods for performing IAR: double difference (DD) IAR and single-receiver (SR) IAR. The DD IAR method involves creating double-differenced observations between two receiver satellites and two GNSS satellites. These observations are free from instrumental delays if one assumes that the two receiver spacecraft are identical (Ge et al., 2005). On the other hand, SR ambiguity fixing typically involves using single-differenced (SD) observations between the receiver satellite and

two GNSS satellites. In this case, only the receiver instrumental delays are eliminated, while the GNSS instrumental biases remain. However, these biases can often be corrected using external data sources.

For LEO satellites, SR IAR has been proven to be a better strategy for absolute POD, while DD IAR is the preferred option for relative POD (Guo et al., 2020; Zhang et al., 2021). Nevertheless, the performance of the DD IAR method degrades as the baseline distance increases, mainly due to the limited number of GNSS satellites in common view, which makes it challenging to perform double differencing (Allende-Alba et al., 2018). In such cases, SR IAR may be a more practical option. Given the significantly large baselines present in the EHI constellation, SR IAR was deemed the most appropriate strategy for POD in this thesis.

### 4.3.2. Integer Ambiguity Resolution Algorithm

This section provides an overview of the Integer Ambiguity Resolution (IAR) algorithm used in this study, which is based on the work developed by Ge et al. (2005) and Montenbruck et al. (2018). The algorithm employs the Melbourne-Wübbena (MW) combination and single difference techniques to resolve wide-lane and narrow-lane ambiguities in GNSS observations.

The first step in the ambiguity fixing process is to compute the MW combination from the dual-frequency code and phase observations. This combination is used to resolve the wide-lane ambiguities. As described in Section 2.4, the MW combination is defined as:

$$MW(\Phi_1, \Phi_2, p_1, p_2) = \frac{c}{f_1 - f_2} \left[ \left( \frac{\Phi_1}{\lambda_1} - \frac{\Phi_2}{\lambda_2} \right) - \frac{f_1 - f_2}{f_1 + f_2} \left( \frac{p_1}{\lambda_1} + \frac{p_2}{\lambda_2} \right) \right] \quad (4.14)$$

By inserting the observation equations of pseudorange ( $p$ ) and carrier phase ( $\Phi$ ), i.e., Equations 2.1 and 2.2, into Equation 4.14, the MW combination can be expressed as:

$$MW(\Phi_1, \Phi_2, p_1, p_2) = \lambda_{WL} N_{r;WL}^s + MW(\xi_{r;1}^s, \xi_{r;2}^s, \zeta_{r;1}^s, \zeta_{r;2}^s) + cMW(K_{r;1}, K_{r;2}, k_{r;1}, k_{r;2}) - cMW(K_1^s, K_2^s, k_1^s, k_2^s) \quad (4.15)$$

where  $\lambda_{WL}$  represents the wide-lane wavelength,  $N_{r;WL}^s$  denotes the wide-lane ambiguity,  $\xi$  and  $\zeta$  refer to the code and phase variations of the receiver and transmitter antennas,  $K_r$  and  $k_r$  represent the code and phase instrumental biases of the receiver antenna, and  $K^s$  and  $k^s$  represent the code and phase instrumental biases of the transmitter antenna.

By forming the MW combination, the geometric range, clock offsets, relativistic effects, first-order ionospheric delays, and phase wind-up are eliminated. However, the MW combination is still affected by the code and phase variations of the receiver and transmitter antennas, as well as the code and phase instrumental biases. Effects such as multipath and thermal noise are neglected in Equation 4.15.

Laurichesse et al. (2009) suggest that the influence of code and phase variations, as well as other measurement errors like multipath, is small enough compared to the wide-lane wavelength so that they can be neglected in the resolution of wide-lane ambiguities. Based on this assumption, the MW observation model can be approximated as:

$$MW(\Phi_1, \Phi_2, p_1, p_2) \approx \lambda_{WL} N_{r;WL}^s + \lambda_{WL} (\mu_{r;WL} - \mu_{WL}^s) \quad (4.16)$$

where the terms  $\mu_{r;WL}$  and  $\mu_{WL}^s$  denote the MW combination of the receiver and transmitter biases in units of the wide-lane wavelength, respectively. The transmitter biases are provided by the International GNSS Service (IGS) analysis centres. Thus, during the POD process, these biases are known and taken into account to ensure accurate resolution of wide-lane ambiguities. On the other hand, receiver biases remain unknown.

For each pass, the carrier phase ambiguity remains constant if no cycle slips occur, allowing the ambiguity fixing to be performed on a pass-wise basis rather than epoch-wise. Hence, the next step is to compute the mean value of the MW combination for each pass  $I$  and adjust the obtained value by incorporating the wide-lane transmitter biases:

$$m_I = \frac{(\overline{MW})_I}{\lambda_{WL}} + \mu_{WL}^s \quad (4.17)$$

By substituting Equation 4.16 into Equation 4.17,

$$m_I = (N_{r;WL}^s)_I + \mu_{r;WL} \quad (4.18)$$

where  $(N_{r;WL}^s)_I$  represents the pass-specific wide-lane ambiguity.

The subsequent step involves the computation of the MW wide-lane single-differenced ambiguities  $N_{WL}^{SD}$ , which helps eliminate the receiver biases present in Equation 4.18 and ensures the ambiguity becomes an integer value.

Following that, the fixing probability of the MW wide-lane SD ambiguities is determined. If this probability surpasses a specific threshold, the computation of the narrow-lane (NL) SD ambiguity is performed. The narrow-lane ambiguities are determined by combining the wide-lane SD ambiguities and the ionospheric-free ambiguities obtained from the preceding float orbit determination process, as outlined in Equation 4.19.

$$N_{NL}^{SD} = \frac{f_1 + f_2}{f_1} N_{IF}^{SD} - \frac{f_2}{f_1 - f_2} N_{WL}^{SD} \quad (4.19)$$

where  $N_{IF}^{SD}$  are the single-differenced ionospheric-free ambiguities, and  $f_1$  and  $f_2$  are the frequencies of the original signals.

The fixing probability of the narrow-lane SD ambiguities is then determined. All the single differences are sorted based on their combined probability of being fixed, which is defined as the product of the WL and NL fixing probabilities. As multiple SD ambiguities are formed, some redundancies may exist. Therefore, the independent subset of SD ambiguities is selected from the complete set of possibilities.

The independent SD equations are incorporated into the normal equations of the float orbit determination problem to enforce the integer nature of the ambiguities. By solving these constrained equations, a revised set of estimated parameters is obtained, which includes the ambiguities, initial state vector, receiver clock offsets, and other relevant variables. These updated parameters serve as input for the subsequent iteration of the ambiguity fixing procedure.

The iteration continues until no further ambiguities can be resolved or until the maximum number of iterations is reached. Upon completion of the iteration, the final obtained parameters are employed as the initial estimates for a new orbit estimation process. In this subsequent estimation, the previously fixed integer ambiguities are retained, while the float ambiguities that could not be fixed are re-estimated.

## 4.4. POD Software

The history of orbit determination software dates back to the launch of the first satellites. Over time, different organizations have developed software for this purpose. In this section, two POD software packages will be highlighted: NAPEOS (Navigation Package for Earth Orbiting Satellites), developed by the European Space Agency (ESA), and MAORI (Multi-purpose Advanced Orbit Restitution Infrastructure), developed by GMV

NAPEOS emerged in the 1990s and was developed in Fortran 90/95. At the European Space Operations Centre (ESOC), NAPEOS was first employed for flight dynamics and POD of LEO satellites. At GMV, an initial version of NAPEOS from the early 2000s was used as a starting point for the development of FocusSuite, which is used for spacecraft flight dynamics operations, mission analysis, and orbit determination (Fernandez, 2022).

On the other hand, MAORI is a new flight dynamics C++ library developed by GMV in the 2020s. This library enables the development of advanced flight dynamics tools for precise orbit determination. MAORI is already being used in the operational POD service of the Copernicus programme provided by GMV.

One of the main differences between NAPEOS and MAORI is the architecture of the data model. NAPEOS does not clearly separate the data from the algorithms. Each programme generates output data that must be written to files so that the next programme in the chain can use them as inputs. For example, the GNSSSIM module simulates GNSS observations and writes them to a file, which the BAHN module reads and uses in a batch least-squares orbit determination.

In contrast, MAORI adopts a central data model that stores all the data in a common data layer known as *scenario*, which all algorithms can access and manipulate. The data within the scenario is organized in a physically meaningful structure, represented by a set of tables that capture the data and their relationships. As a result, the data can be accessed throughout the orbit determination process without continuously writing and reading files. Figure 4.7 provides a visual representation of the data models of NAPEOS and MAORI, emphasizing their differences.

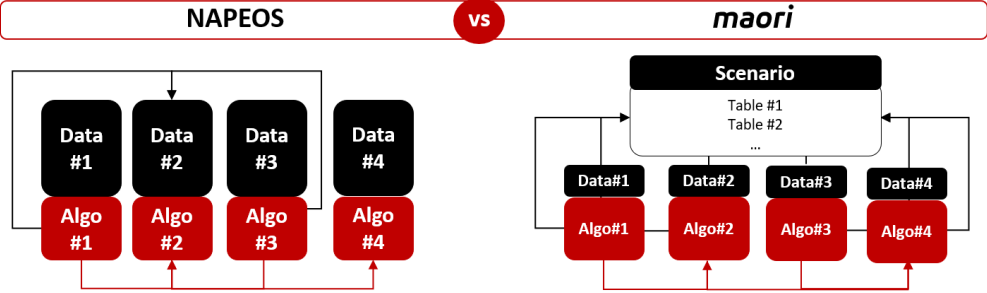


Figure 4.7: Representation of the data model architectures of NAPEOS and MAORI.

In this thesis, the MAORI library has been employed to conduct all simulations and perform the orbit determination. The new algorithms developed in MAORI as part of this thesis have been validated using NAPEOS. Moreover, NAPEOS was also employed to validate some of the results of this study, given that it was the technology used in the previous EHI mission studies conducted by Guindal-Martinez (2020) and GMV (2022).

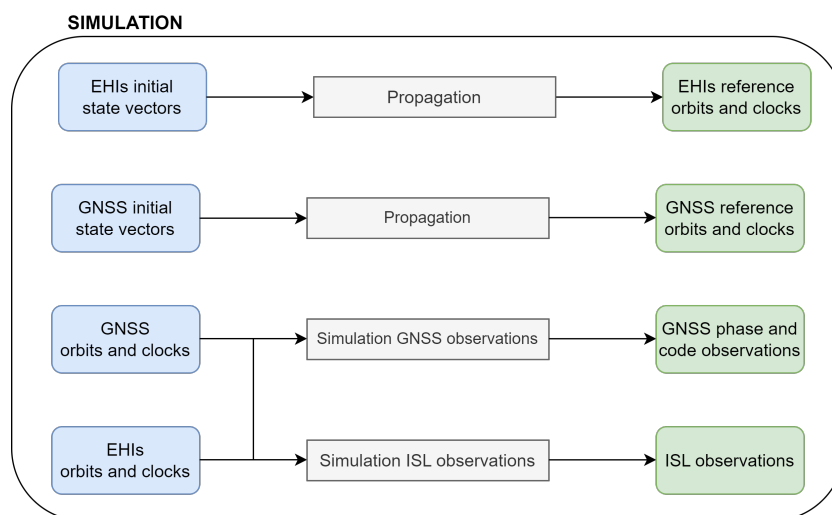
# 5

## Methodology

The objective of this chapter is to present the methodology used in this thesis. It covers several key components, including the generation of reference orbits and clocks, the simulation of observations and error sources, and the precise orbit determination process. Figure 5.1 provides a schematic diagram of the thesis methodology.

Initially, the GNSS and EHI satellites initial state vectors are propagated using state-of-the-art dynamic models, resulting in the generation of the reference orbits and clocks. These orbits and clocks are employed to simulate the GNSS observations. Additionally, the EHI orbits and clocks are used to generate the ISL observations. To enhance the realism of the analysis, errors such as thermal noise can be introduced to the observations, and perturbations can be applied to the GNSS orbits and clocks, as well as to the dynamic models. The absolute POD process then employs the GNSS orbits, clocks, and observations to estimate the orbits and clocks of the EHI-1 and EHI-2 satellites. In the relative POD process, the ISL observations and the previously estimated orbit and clocks of EHI-1 are also incorporated to obtain a refined solution for EHI-2.

The chapter begins by describing the generation of the reference orbits and clocks, followed by the simulation of the GNSS and ISL observations. The chapter then covers the modeling of different error sources, including clock biases, GNSS thermal noise, instrumental delays, errors in the GNSS orbits and clocks, laser noise, uncertainties in the geopotential model, and uncertainties in the solar radiation pressure model. Lastly, the POD process itself is explained, encompassing both the absolute POD and the relative POD.



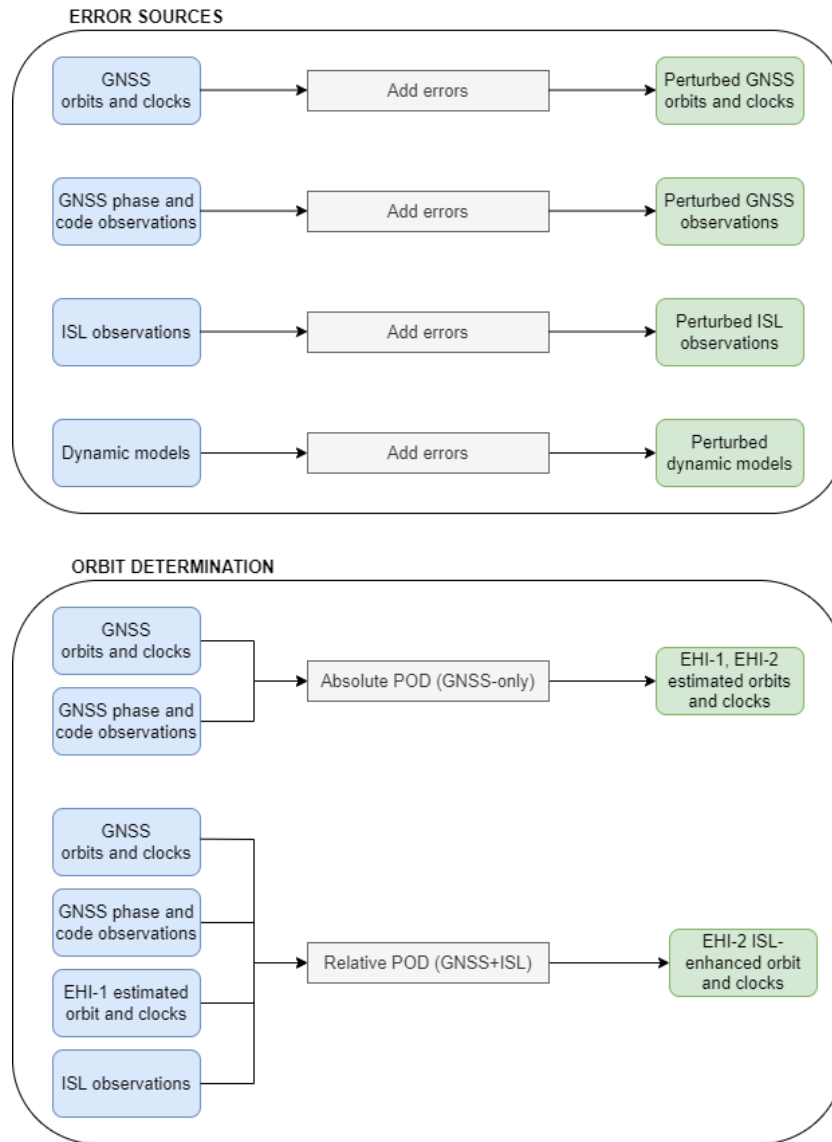


Figure 5.1: Overview of the thesis methodology.

## 5.1. Generation of Reference Orbits and Clocks

### 5.1.1. Generation of Reference Orbits

As the mission has not been launched yet, there is no real observational data available. Therefore, the orbits of both the GNSS and EHI satellites must be simulated in order to then generate the observations from them. These orbits are simulated by propagating the initial state vectors of the satellites using realistic dynamic models. These propagated orbits will serve as the reference, representing the reality.

All initial state vectors are referred to the epoch 01/04/2022 00:00:00 GPS. Then, the propagation is performed for each day of the month of April 2022, using either 24-hour or 34-hour propagation arcs. The 34-hour arcs are centered on a nominal day and include 5 hours before and after the nominal day. Moreover, in all propagations, a multi-step 8<sup>th</sup> Adams-Bashforth-Moulton propagator is used, with 420 steps per revolution.

#### 5.1.1.1. Generation of Reference GNSS Orbits

The GNSS initial state vectors are generated according to the GPS and Galileo constellation information retrieved in Section 2.1. In this way, this simulation includes 30 GPS satellites distributed among 6 different orbital planes and 24 Galileo satellites located at 3 different planes. The initial argument of

perigee for all satellites is set to zero degrees, while the true anomalies are selected to ensure the satellites are distributed according to the typical GPS and Galileo constellation designs.

The full dynamical model used for generating the GNSS reference orbits is presented in Table 5.1. Regarding the attitude, it is assumed that the GPS satellites follow the typical GPS attitude law, which implies a yaw-steering attitude mode. In the same way, the Galileo satellites follow the classic Galileo attitude law, also employing a yaw-steering mode.

<b>GNSS Dynamical Model</b>	
Gravity Field (static)	EIGEN-GRGS.RL04.MEAN-FIELD.quadratic_mean_pole_grace (12x12)
Gravity Field (time-varying)	Drift/annual/semi-annual- piece-wise linear terms (1x1)
Solid Earth Tides	IERS 2010
Ocean Earth Tides	FES2014 (12x12)
Earth Pole Tides	IERS 2010
Ocean Pole Tides	IERS 2010
Third Body	Sun, Moon and all planets in Solar System DE405
Relativistic Gravitation	IERS 2010
Solar Radiation Pressure	Constant area: $A_{GPS} = 13.6 \text{ m}^2$ , $A_{GAL} = 13.0 \text{ m}^2$ , and $C_R = 1$
Earth's Albedo	Not applied
Earth's Infrared	Not applied
Atmospheric Effects	Not applied

**Table 5.1:** Dynamic model used in the propagation of the GNSS reference orbits.

#### 5.1.1.2. Generation of Reference EHI Orbits

As mentioned in Section 1.2, the EHI-1 and EHI-2 spacecraft are assumed to be located at polar circular orbits of 8,280 and 8,303.3 km altitude, respectively. Moreover, the initial Right Ascension of the Ascending Node (RAAN) is 140.9 degrees for both EHIs. For a detailed representation of the initial state vectors of the EHI satellites, refer to Table 1.1.

The dynamic model used in the propagation of the reference orbits of the EHIs is summarized in Table 5.2. As for the macro-model, the simplified macro-model described in Section 1.2.2 is employed. In terms of attitude, it is assumed that the EHIs follow the Sagittarius A\* pointing law discussed in Section 1.2.

<b>EHI Dynamical Model</b>	
Gravity Field (static)	EIGEN-GRGS.RL04.MEAN-FIELD.quadratic_mean_pole_grace (35x35)
Gravity Field (time-varying)	Drift/annual/semi-annual- piece-wise linear terms (10x10)
Solid Earth Tides	IERS 2010
Ocean Earth Tides	FES2014 (35x35)
Earth Pole Tides	IERS 2010
Ocean Pole Tides	IERS 2010
Third Body	Sun, Moon and all planets in Solar System DE405
Relativistic Gravitation	IERS 2010
Solar Radiation Pressure	Macro-model
Earth's Albedo	Macro-model
Earth's Infrared	Macro-model
Atmospheric Effects	Not applied

**Table 5.2:** Dynamic model used in the propagation of the EHI reference orbits.

#### 5.1.2. Generation of Reference Clocks

In a similar manner to the ephemerides data, it is necessary to simulate the GNSS and EHI clocks in order to generate the GNSS observations. These simulated clocks will be considered as the reference,

assuming they represent the truth. For each EHI satellite, two clocks are being simulated, corresponding to the two different GNSS antennas. On the other hand, only one clock is simulated per GNSS satellite. The clock simulation is based on the model described by Galleani et al. (2003).

If no noise is introduced into the model, the simulated clock will have zero bias, and thus the clock offset in the observation equations will be zero. This scenario represents an ideal clock condition, where the clocks are perfectly aligned with GPS time. Since no intersystem bias has been introduced into the simulations, GPS time is also perfectly aligned with Galileo time.

## 5.2. Generation of Observations

The next step is to use the aforementioned reference orbits and clocks to generate the simulated observations. These observations include both GNSS pseudorange and carrier phase measurements between the GNSS satellites and the EHIs, as well as the optical intersatellite link measurements between the two EHIs. This section describes the methodology used to generate these observations together with the assumptions and simplifications made in the process.

### 5.2.1. Generation of GNSS Observations

In order to generate the GNSS observations, the first step is to simulate the visibility between the GNSS and EHI satellites using their corresponding reference orbits. It is considered that a satellite 'sees' another satellite when they are both within each other's antenna field-of-view (FOV). A cone is typically used to define the FOV of an antenna. The axis of this cone is the antenna pointing, and its half-angle is the antenna half-aperture.

Each GNSS satellite has one emitter antenna that follows the typical GNSS pointing law, directing its signal towards the centre of the Earth. The phase centres of the GNSS antennas are located at the typical positions provided by the International GNSS Service (IGS) for each respective GNSS satellite. The FOV semi-angle is assumed to be 23.5 deg for GPS and 20.5 deg for Galileo.

On the other hand, each EHI has two antennas: one pointing towards the black hole and the other in the opposite direction. The positions of the EHI antennas are given by Table 1.2. Each antenna has an aperture of 180 deg, allowing the EHIs to see the whole sky. Table 5.3 summarizes the characterization of the FOV of all the antennas.

Antenna	Pointing	Semi-aperture angle [deg]
GPS	Geocentric pointing	23.5
Galileo	Geocentric pointing	20.5
EHI-1 Q1	Towards Sagittarius A* pointing	90
EHI-1 Q2	Opposite to Sagittarius A* pointing	90
EHI-2 Q1	Towards Sagittarius A* pointing	90
EHI-2 Q2	Opposite to Sagittarius A* pointing	90

**Table 5.3:** Field-of-view properties of the antennas.

In order to avoid that the GNSS signal travels through the troposphere, a grazing altitude can be defined to ensure that no signal gets too close to the surface of the Earth. Previous studies have shown that a grazing altitude of 100 km is suitable to filter out signals affected by the tropospheric delay without compromising visibility (Guindal-Martinez, 2020). To better illustrate how visibility is defined, Figure 5.2 presents a simplified sketch that exemplifies how visibility would be represented between a GPS and an EHI antenna. It is also worth noting that there is no maximum limit on the number of GNSS channels.

After determining the visibility between the GNSS and EHI satellites, dual-frequency code and phase observations are simulated at a rate of 10 seconds. The GPS satellites transmit signals on the L1 and L5 frequencies, while Galileo uses E1 and E5a. These observations are combined to create an ionospheric-free linear combination, as explained in Section 2.4.2. This combination reduces the ionospheric delay of the signals by 99%. The simulation of the GNSS observables involves accounting for various contributions, which include:

- Geometric range, including the light-time correction.

- Relativistic effects, including the periodical clock corrections and the Shapiro effect.
- Emitter and receiver clock offsets, which are assumed to be zero in the error-free scenario.
- Location of the antenna reference point with respect to the centre of mass of the satellite.
- Antenna phase centre offsets and variations. The GNSS calibration maps are retrieved from the IGS14 ANTEX (Antenna Exchange Format) file provided by IGS. The EHIs' PCOs and PCVs are assumed to be zero.
- Phase wind-up.
- Phase ambiguity.
- Instrumental delays, which are assumed to be zero in the error-free scenario.

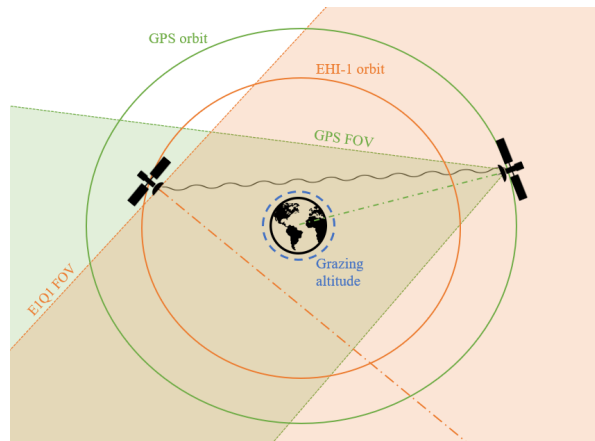


**Figure 5.2:** Sketch of the visibility between a GPS antenna and one of the EHI-1 antennas.

#### 5.2.1.1. Generation of GNSS Ambiguity

Simulating carrier phase ambiguity is a complex process, as it involves an unknown integer number of cycles. Hence, special attention must be given to explain how it is simulated. It is assumed that the ambiguity during one pass is constant, as no cycle slips are introduced in the simulation. To simulate this pass-wise ambiguity, a random number is generated for each pass, following a uniform distribution between 0 m and the average distance between the GNSS and EHI spacecraft in that pass. This random distance is then transformed into cycles, and only the integer part of this float number of cycles is taken. Finally, this integer number of cycles is converted back to distance units.

#### 5.2.1.2. Generation of GNSS Instrumental Delays

Modeling instrumental delays is essential in simulating high-precision GNSS observations, especially when using integer ambiguity resolution techniques during the POD. Instrumental delays are typically modeled as a bias in the observations, which differs for each instrument and signal type. Both the receiver and emitter satellites exhibit instrumental biases that affect pseudorange and carrier phase observations. Hence, it is necessary to simulate the code and phase biases for both the GNSS and EHI instruments.

The biases of GNSS satellites are determined and provided by various analysis centres, such as CODE. These centres provide daily estimated values of the bias parameters ( $B$ ) along with their corresponding estimated standard deviations ( $SD$ ). This information is commonly presented in the Bias-SINEX (Solution INdependent EXchange) data format, which is widely used in the GNSS community. Figure 5.3 provides an excerpt of a Bias-SINEX V1.00 file, showing the format of the data provided by these analysis centres. In this bias estimation procedure conducted by CODE, the estimation of the code biases is coupled with the estimation of the GNSS clocks (Schaer et al., 2021).

To simulate these instrumental delays, the distribution of the bias final products provided by CODE was examined. It was observed that phase biases displayed a uniform distribution ranging from -1.5 ns to 1.5 ns, represented as  $B_{CP}^s \sim U(-1.5, 1.5)$  ns. Therefore, GNSS phase biases are randomly generated according to this distribution. On the other hand, the values of code biases in the analyzed data were uniformly distributed between -15 ns and 15 ns, represented as  $B_{PR}^s \sim U(-15, 15)$  ns. However,

for simplicity, the GNSS code biases are set to zero in this project. This decision was made because these biases are typically coupled with the simulation of GNSS clocks, which was not considered in this project.

The simulation of the code and phase instrumental biases at the receiver follows a similar approach to that used for the GNSS satellites. The phase biases are randomly generated according to the distribution  $B_{r,CP} \sim U(-1.5, 1.5)$  ns. Nevertheless, in contrast to the GNSS satellites, the code biases at the receiver are not set to zero, and thus the clock estimation will absorb them, as it happens in real applications. Thus, the receiver code biases are generated following the distribution  $B_{r,PR} \sim U(-15, 15)$  ns.

*BIAS SVN_	PRN	STATION_	OBS1	OBS2	BIAS_START_	BIAS_END_	UNIT_	ESTIMATED_VALUE_	_STD_DEV_
OSB	G063	G01	C1C		2018:256:00000	2018:257:00000	ns	11.0960	0.0065
OSB	G063	G01	C1W		2018:256:00000	2018:257:00000	ns	12.1990	0.0064
OSB	G063	G01	C2W		2018:256:00000	2018:257:00000	ns	20.1247	0.0084
OSB	G061	G02	C1C		2018:256:00000	2018:257:00000	ns	-12.8302	0.0066
OSB	G061	G02	C1W		2018:256:00000	2018:257:00000	ns	-14.1435	0.0065
OSB	G061	G02	C2W		2018:256:00000	2018:257:00000	ns	-23.2726	0.0084
OSB	G069	G03	C1C		2018:256:00000	2018:257:00000	ns	7.3892	0.0065
OSB	G069	G03	C1W		2018:256:00000	2018:257:00000	ns	8.3351	0.0064
OSB	G069	G03	C2W		2018:256:00000	2018:257:00000	ns	13.8998	0.0084
OSB	G063	G01	L1C		2018:256:00000	2018:257:00000	ns	-0.40989	0.00000
OSB	G063	G01	L1W		2018:256:00000	2018:257:00000	ns	-0.40989	0.00000
OSB	G063	G01	L2W		2018:256:00000	2018:257:00000	ns	-0.67184	0.00000
OSB	G063	G01	L2X		2018:256:00000	2018:257:00000	ns	-0.67184	0.00000
OSB	G061	G02	L1C		2018:256:00000	2018:257:00000	ns	-0.86212	0.00000
OSB	G061	G02	L1W		2018:256:00000	2018:257:00000	ns	-0.86212	0.00000
OSB	G061	G02	L2W		2018:256:00000	2018:257:00000	ns	-1.31564	0.00000
OSB	G061	G02	L2X		2018:256:00000	2018:257:00000	ns	-1.31564	0.00000
OSB	G069	G03	L1C		2018:256:00000	2018:257:00000	ns	-0.32326	0.00000
OSB	G069	G03	L1W		2018:256:00000	2018:257:00000	ns	-0.32326	0.00000
OSB	G069	G03	L2W		2018:256:00000	2018:257:00000	ns	-0.43774	0.00000
OSB	G069	G03	L2X		2018:256:00000	2018:257:00000	ns	-0.43774	0.00000

Phase biases

Code biases

**Figure 5.3:** Bias-SINEX V1.00 file excerpt, illustrating observable-specific signal bias entries for all involved pseudorange code (blue) and carrier phase (red) observable types (Schaer et al., 2021).

### 5.2.2. Generation of ISL Observations

The ISL observable is modeled as a very high-frequency pseudorange observation, with a wavelength of 1064 nm. In order to simulate the visibility of the ISL, it is assumed that the ISL instruments located in the EHIs have a 360-degree field of view, enabling them to see all the sky and ensuring continuous line-of-sight visibility between the EHI satellites.

The simulated ISL observations are generated at a rate of 10 seconds and include the geometrical range, relativistic effects, and the location of the ISL instrument reference point, which can be retrieved from Table 1.2. Since the ISL measurements are two-way range observations, the simulation does not require the inclusion of clock offsets. Similar to the GNSS observations, a grazing altitude of 100 km is used to avoid the troposphere. Moreover, the frequency of the optical ISL is high enough so that it is not affected by the ionosphere (Sosnica et al., 2015).

## 5.3. Generation of Error Sources

In the following section, the generation of error sources is explored as a crucial component of the simulation methodology. Accurately modeling these errors is essential for assessing the performance and robustness of the orbit determination process. Several key error sources are considered, including errors in the GNSS observations such as clock biases, thermal noise, and instrumental delays, errors in the GNSS orbits and clocks, laser noise in the intersatellite link, and errors in the dynamical model.

### 5.3.1. Clock Biases

To simulate the reference clock accurately, it is necessary to incorporate the effect of clock noise in the clock generation process. This clock simulation model follows the approach described by Galleani et al. (2003). The expression used to compute the noise is:

$$\begin{bmatrix} b_{\text{clk}}(t_k) \\ d_{\text{clk}}(t_k) \end{bmatrix} = \begin{bmatrix} 1 & \Delta t \\ 0 & 1 \end{bmatrix} \begin{bmatrix} b_{\text{clk}}(t_{k-1}) \\ d_{\text{clk}}(t_{k-1}) \end{bmatrix} + \begin{bmatrix} \Delta t & \Delta t^2/2 \\ 0 & \Delta t \end{bmatrix} \begin{bmatrix} 0 \\ \Delta f \end{bmatrix} + \mathbf{L} \begin{bmatrix} n_0 \\ n_1 \end{bmatrix} \quad (5.1)$$

where  $b_{\text{clk}}$  represents the clock bias,  $d_{\text{clk}}$  represents the clock drift,  $\Delta t$  is the clock sampling rate,  $\Delta f$  is the frequency drift,  $n_0$  and  $n_1$  are normally distributed random variables with zero mean and unit

variance ( $n_0, n_1 \sim N(0, 1)$ ), and  $L$  is a lower triangular matrix such that  $B = LL^*$ , where  $L^*$  denotes the conjugate transpose of  $L$ . The matrix  $B$  is constructed considering the clock diffusion coefficients of the phase deviation ( $\sigma_1$ ) and the 'random walk' component of the frequency deviation ( $\sigma_2$ ):

$$B = \begin{bmatrix} \sigma_1^2 \Delta t + \sigma_2^2 \frac{\Delta t^3}{3} & \sigma_2^2 \frac{\Delta t^2}{2} \\ \sigma_2^2 \frac{\Delta t^2}{2} & \sigma_2^2 \Delta t \end{bmatrix} \quad (5.2)$$

Therefore, this clock model requires the consideration of several parameters, including the initial bias ( $b_0$ ), initial drift ( $d_0$ ), the frequency drift ( $\Delta f$ ), and  $\sigma_1$  and  $\sigma_2$ . The values of these clock parameters have been adjusted by analyzing real clocks used in GNSS navigation. This analysis is based on computing the Allan deviation of the clock biases, which is a common statistical measure of the stability of a clock over time. The Allan deviation characterizes how the clock bias varies as a function of the averaging time (Kaplan & Hegarty, 2006).

### 5.3.1.1. GNSS Clock Biases

For this analysis, the GNSS clock products provided by the Center for Orbit Determination in Europe (CODE) are employed, specifically the CODE final series clock products. These clocks have a rate of 5 seconds. The data used corresponds to the period between 01/01/2023 00:00:00 GPS and 24/01/2023 00:00:00 GPS. The Allan deviation is calculated for each of the clocks at different averaging time intervals to examine the temporal stability of the clocks.

The objective of this analysis is to adjust the Allan deviation of a simulated clock to match that of the real GNSS clocks by fine-tuning  $\sigma_1$  and  $\sigma_2$ . The clock initial bias, initial drift, and frequency drift are all set to zero, which is a reasonable assumption considering the very low frequency drift of GNSS clocks (Teunissen & Montenbruck, 2017).

As described in Section 2.1.1, the operational GPS satellites are divided into four blocks, with Block IIR exhibiting similar clock behaviour to Block IIR-M, while Block IIF is comparable to Block III. Figure 5.4a presents the Allan deviation of one clock from each GPS block, along with the simulated clock that was found to be the best match with  $\sigma_1 = 2 \times 10^{-12}$  and  $\sigma_2 = 10^{-16}$ . The behaviour of the simulated clock closely matches the expected behaviour of Caesium atomic clocks found in GPS satellites, as described by Teunissen and Montenbruck (2017).

Similarly, the Allan deviation of Galileo clocks was analyzed and the results are shown in Figure 5.4b. The optimal values for simulating the Galileo clocks were determined to be  $\sigma_1 = 2 \times 10^{-12}$  and  $\sigma_2 = 3 \times 10^{-17}$ . It is worth noting that the value of  $\sigma_2$  for Galileo clocks is lower compared to GPS clocks, indicating better long-term stability possibly due to the presence of very stable passive Hydrogen masers on Galileo satellites, in addition to Rubidium atomic clocks (Teunissen & Montenbruck, 2017). Although some Galileo clocks deviate from the overall trend in Allan deviation, this aspect will not be further explored in this thesis.

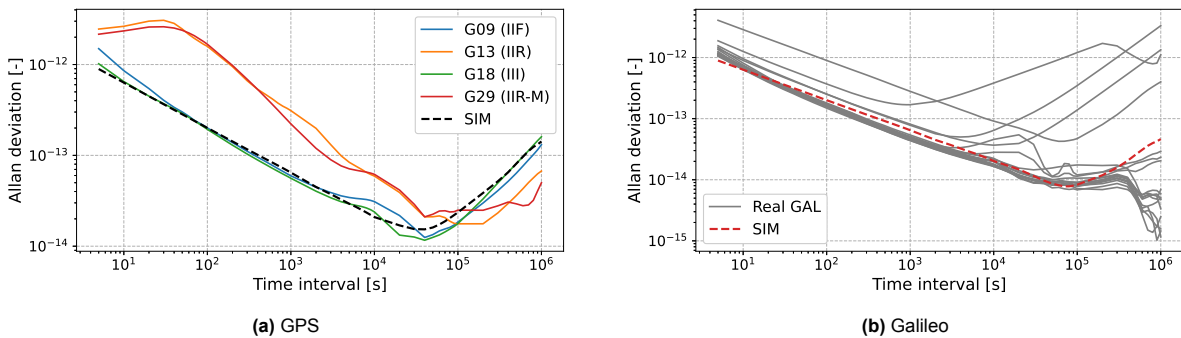


**Figure 5.4:** Allan deviation of real GPS and Galileo clocks and the optimal simulated GPS and Galileo clocks. For Galileo, each gray line represents a different clock within the constellation.

### 5.3.1.2. EHI Clock Biases

An ultra-stable Oven Controlled Crystal Oscillator (OCXO) is assumed to be used in the EHI satellites, which is also the type of oscillator used on-board Sentinel-3A, -3B, and -6A (GMV, 2022). Consequently,

a similar analysis as the one performed for the GNSS clocks will be conducted using the Sentinel clocks estimated by GMV's Copernicus Precise Orbit Determination (CPOD) operational service.

Figure 5.5 presents the Allan deviation of the Sentinel-3A (S3-A), Sentinel-3B (S3-B), and Sentinel-6A (S6-A) clocks. The clock data has a sampling rate of 10 seconds and corresponds to the period from 31/12/2022 20:00:00 GPS to 02/01/2023 04:00:00 GPS. The simulated clock that best matched the stability of these ultra-stable oscillators (USOs) is also shown in the figure. This simulated clock was obtained using  $\sigma_1 = 2 \times 10^{-11}$  and  $\sigma_2 = 5 \times 10^{-16}$ . These parameters are used to simulate the EHI-1 and EHI-2 clocks. A summary of the parameters used for simulating all the required clocks can be found in Table 5.4.

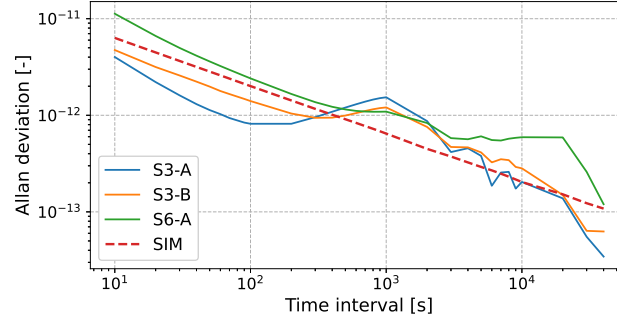


**Figure 5.5:** Allan deviation of Sentinel-3A, -3B and -6A clocks and the optimal simulated EHI clock.

Clock parameter	GPS	GAL	EHI-1/-2
$b_0$ [s]	0	0	0
$d_0$ [s/s]	0	0	0
$\Delta f$ [s/s <sup>2</sup> ]	0	0	0
$\sigma_1$ [-]	$2 \times 10^{-12}$	$2 \times 10^{-12}$	$2 \times 10^{-11}$
$\sigma_2$ [-]	$10^{-16}$	$3 \times 10^{-17}$	$5 \times 10^{-16}$

**Table 5.4:** Clock models used for simulating the GNSS and EHI clocks.

### 5.3.2. Thermal Noise

The thermal noise at the GNSS receiver affects the quality of the observations. The level of thermal noise depends on the signal-to-noise ratio (SNR) of the received signal and on several characteristics of the receiver. These characteristics vary depending on the type of signal and the observable being considered, whether it is a pseudorange or a carrier phase observable. To model thermal noise in GNSS observations, Kaplan and Hegarty (2006) propose a Gaussian noise model. The standard deviations for the code and phase observables can be computed using Equations 5.3 and 5.4, respectively.

$$\sigma_{PR} = \lambda_C \sqrt{\frac{Bd}{2C/N_0} \left(1 + \frac{1}{T_c C/N_0}\right)} \quad (5.3)$$

$$\sigma_{CP} = \frac{\lambda}{2\pi} \sqrt{\frac{B}{C/N_0} \left(1 + \frac{1}{2T_c C/N_0}\right)} \quad (5.4)$$

where  $\lambda_C$  is the signal chip length,  $B$  is the loop noise bandwidth,  $d$  is the correlation spacing,  $T_c$  is the coherent integration time,  $\lambda$  is the signal wavelength, and  $C/N_0$  is the carrier-to-noise ratio.

The parameters in Equations 5.2 and 5.3 vary depending on the frequency band of the transmitted signal. Tables 5.5 and 5.6 summarize the values corresponding to GPS L1 and L5, and Galileo E1 and E5a code and phase observations, based on the parameter values proposed by Zangerl (2017) for a LEO POD receiver.

Parameter	Code L1	Code E1	Code L5/E5a
Loop bandwidth, $B$ [Hz]	0.5	0.5	0.25
Coherent integration time, $T_c$ [ms]	10	12	20
Correlation spacing, $d$ [chips]	0.1412	0.0706	0.706
Chip length, $\lambda_c$ [m]	293.05	293.05	29.305

Table 5.5: Code Tracking Loop Parameters (Zangerl, 2017).

Parameter	Carrier L1	Carrier E1	Carrier L5/E5a
Loop bandwidth, $B$ [Hz]	10	10	5
Coherent integration time, $T_c$ [ms]	10	12	20
Wavelength, $\lambda$ [mm]	190.29	190.29	254.8

Table 5.6: Carrier Tracking Loop Parameters (Zangerl, 2017).

The strength of this thermal noise component is also dependant on the SNR, which is a measure of the strength of a signal compared to the environment background noise. Another metric that represents the same concept is the carrier-to-noise ratio ( $C/N_0$ ). To simulate the  $C/N_0$  values, the link budget analysis presented by Perello-Gisbert and Garcia (2010) is used. This approach takes into account various factors such as the transmitted power, antenna gains, hardware losses, free-space losses, and receiver noise temperature. In this formulation, the carrier-to-noise ratio is expressed in decibels as:

$$\frac{C}{N_0} = EIRP + \frac{G}{T} - FSPL - HWL \quad (5.5)$$

where  $EIRP$  is the effective isotropically radiated power of the transmitter antenna,  $G/T$  is the gain-to-noise temperature ratio of the receiver antenna,  $FSPL$  are the free-space path losses, and  $HWL$  are the hardware losses.

Each of these contributions can be further developed. First, the effective isotropically radiated power depends on the power ( $P_{TX}$ ) and the gain ( $G_{TX}$ ) of the transmitter antenna, as shown in Equation 5.6. The transmit power is a constant value depending on the frequency of the observation, while the gain depends also on the elevation and azimuth angles according to a specific antenna radiation pattern.

$$EIRP = P_{TX} + G_{TX} \quad (5.6)$$

The next contribution to the  $C/N_0$  is the gain-to-noise temperature ratio of the receiver antenna. This ratio depends on the gain of the receiver antenna ( $G_{RX}$ ) and the system noise temperature ( $T_{sys}$ ), as expressed in Equation 5.7. Similar to the transmitter, the gain of the receiver antenna can vary with elevation and azimuth angles. In the simulations, a fixed noise temperature of 300 K is assumed.

$$\frac{G}{T} = G_{RX} - k_B 10 \log_{10}(T_{sys}) \quad (5.7)$$

where  $k_B$  is the Boltzmann constant expressed in dBW/HzK.

Another important contribution to the carrier-to-noise ratio is the free-space path losses. These losses occur because the signal strength diminishes as it propagates through space. The calculation of this loss is expressed by:

$$FSPL = 20 \log_{10} \left( \frac{4\pi Df}{c} \right) \quad (5.8)$$

where  $D$  is the distance between emitter and receiver,  $f$  is the frequency of the signal, and  $c$  is the speed of light.

The last contribution to the carrier-to-noise ratio is the hardware losses, which account for the losses in the transmitter and receiver hardware. These losses are typically caused by factors such as cable losses, connector losses, and mismatches in the antenna system. The total hardware loss ( $HWL$ ) is calculated as the sum of the emitter and receiver losses:

$$HWL = HWL_{TX} + HWL_{RX} \quad (5.9)$$

where  $HWL_{TX}$  and  $HWL_{RX}$  are the losses in the transmitter and receiver hardware, respectively.

It is important to note that the antenna gain pattern  $G_{TX}$  in Equation 5.6 varies depending on the GNSS constellation, satellite block, and band frequency (Ripoll, 2017). Thus, it is crucial to consider the specific antenna gain pattern for each satellite and frequency. Figure 5.6 shows an example of a real antenna pattern for a Block IIR GPS L1 receiver, where each line corresponds to a different azimuth value. From this figure, it is clear that the dependency on elevation is much stronger than the one on azimuth, so the azimuth dependency will be neglected in the antenna model.

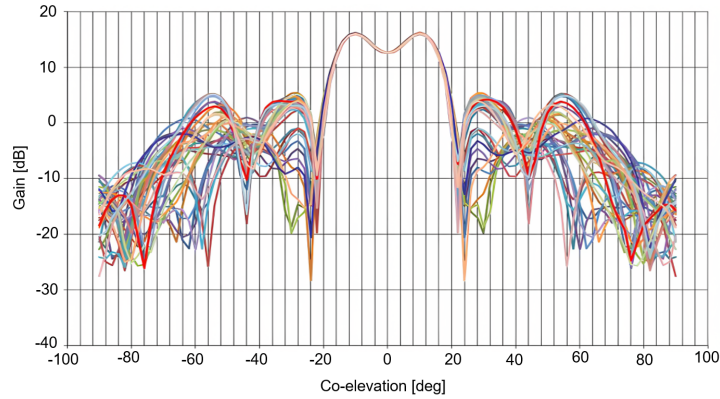


**Figure 5.6:** Antenna gain pattern of GPS L1 in a Block IIR satellite. Each line represents a different azimuth value (Bauer, 2015).

Antenna radiation patterns are often kept undisclosed by the responsible authorities of GNSS constellations due to security concerns. However, Lockheed Martin on behalf of the United States government has published the antenna pattern of the Block IIR GPS antenna. Given the lack of published antenna patterns, it is generally assumed that all other GNSS transmitter antennas have a similar pattern (Ripoll, 2017).

In this thesis, the tabulated antenna transmitter patterns provided by the GNSSSIM tool of NAPEOS have been used. Figure 5.7 illustrates the employed antenna gain patterns for GPS L1 and L5, and Galileo E1 and E5a frequencies. The same pattern is used for all satellites within the same constellation. Furthermore, the transmitted power values  $P_{TX}$  used in the simulations are taken from the same source. Specifically, for GPS, the transmitted power is set to  $P_{TX} = 24$  dBW, while for Galileo, it is set to  $P_{TX} = 24.3$  dBW.

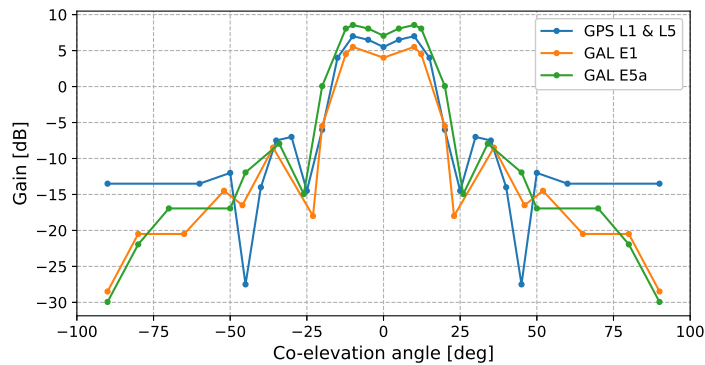


**Figure 5.7:** Antenna gain pattern of simulated GNSS antennas for GPS L1 and L5, and Galileo E1 and E5a frequencies.

In addition to the emitter antenna gain pattern, the carrier-to-noise ratio also depends on the gain of the receiver. However, characterizing the gain of the receiver is more challenging, as the space mission being analyzed in this thesis is in a preliminary stage and data on the receiver antenna gain is not yet available. As a result, a Patch Excite Cup (PEC) antenna design with two choke-rings, designed by RUAG Space, was selected for all the receiver antennas. This antenna design is commonly used for POD applications, particularly in missions such as Swarm and the Sentinels.

The evolution of the receiver antenna gain pattern with respect to the co-elevation angle is shown in Figure 5.8. The gain pattern presented in the figure is based on the pattern provided by Zackrisson and Öhgren (2011). It is important to note that the gain can vary depending on whether the tracked signal is L1/E1 or L5/E5a.

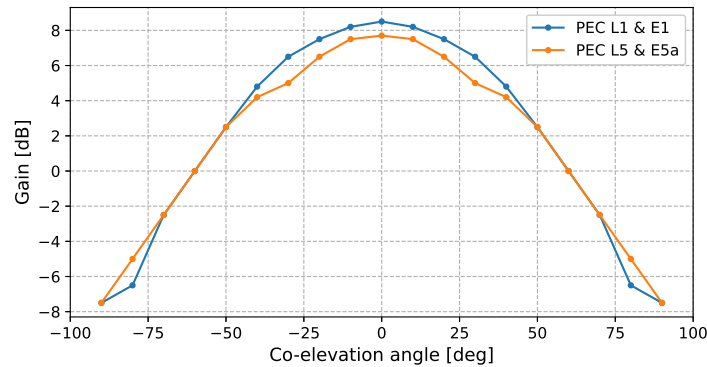


**Figure 5.8:** Antenna gain pattern of a Patch Excite Cup (PEC) antenna tracking L1, L5, E1, and E5a signals.

To validate the chosen antenna gain patterns and ensure their suitability for accurately simulating the thermal noise, the carrier-to-noise ratio of Sentinel-6A was simulated using the same tools employed in this project. The simulated values were then compared with the observed values obtained during actual operations to ensure their compatibility. This analysis serves a dual purpose: not only does it verify the correctness of the selected antenna gain patterns, but it also enables the selection of appropriate values for the hardware losses involved in the simulation process.

Figures 5.9a and 5.9b depict the carrier-to-noise ratio values measured for Sentinel-6A for GPS and Galileo signals. The data, sourced from Bouridah et al. (2021), presents the real carrier-to-noise ratio as a function of the elevation angle. The focus is on S1C signals, corresponding to L1 and E1 frequencies, as well as S5Q signals, corresponding to L5 and E5a frequencies.

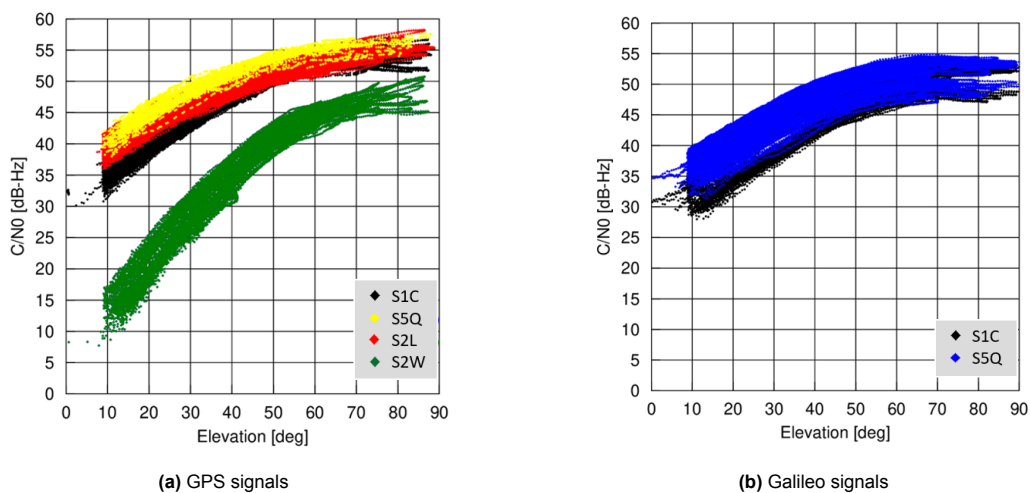


**Figure 5.9:** Real observed carrier-to-noise ratio for GPS and Galileo signals tracked by Sentinel-6A as a function of elevation (Bouridah et al., 2021).

The next step involves simulating the carrier-to-noise ratio for Sentinel-6A using the antenna models described in this section and tuning the hardware losses. After some trial and error, it was found that incorporating hardware losses of 5 dB for GPS antennas and 10 dB for Galileo antennas improved the alignment with the observed results shown in Figure 5.9. However, the inclusion of these hardware losses introduced excessive thermal noise into the observations, leading to discrepancies in the root-mean-square of the observation residuals compared to actual Sentinel-6A operations.

To address this issue, it was decided to set the hardware losses to zero. Figures 5.10a and 5.10b showcase the simulated carrier-to-noise ratio for Sentinel-6A assuming no hardware losses. Although this assumption results in simulated carrier-to-noise ratio values that are higher than the real ones, it is a necessary step to avoid introducing unrealistic levels of thermal noise. Thus, in the context of this thesis, the hardware losses will be assumed to be zero as well.

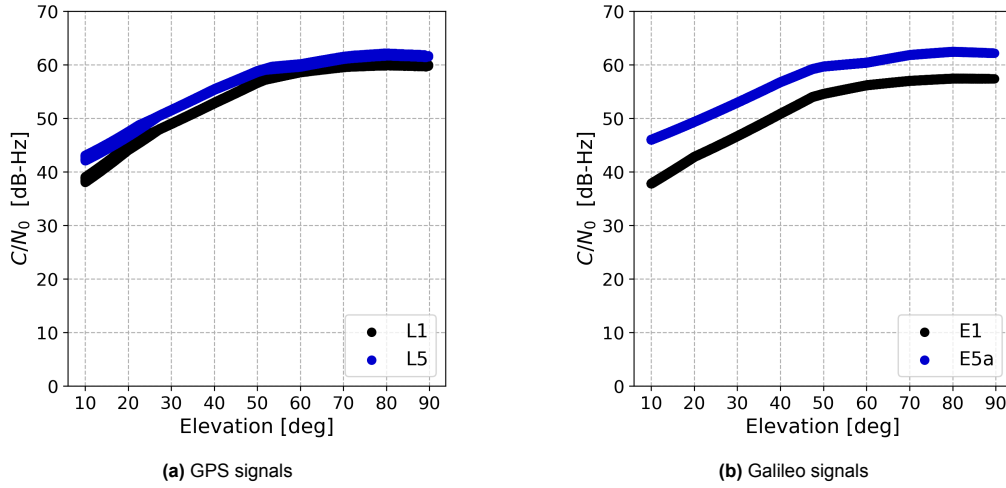


**Figure 5.10:** Simulated carrier-to-noise ratio for GPS and Galileo signals tracked by Sentinel-6A as a function of elevation, assuming no hardware losses.

### 5.3.3. Instrumental Delays

To introduce uncertainty in the estimation process during the orbit determination, a distinct set of instrumental delays is employed, which differs from the ones used for generating the GNSS observations. This is achieved by perturbing the instrumental biases used in generating the GNSS observations.

The emitter GNSS instrumental biases are perturbed using a normal distribution, with the mean equal to the previously simulated bias value and a random standard deviation ( $SD$ ). For each bias value, a random  $SD$  needs to be generated, following a normal distribution with a mean  $\mu$  and a standard deviation  $\sigma$ . These perturbed biases are then employed in the POD process. Figure 5.11 illustrates the methodology followed to generate both the unperturbed and perturbed bias values.

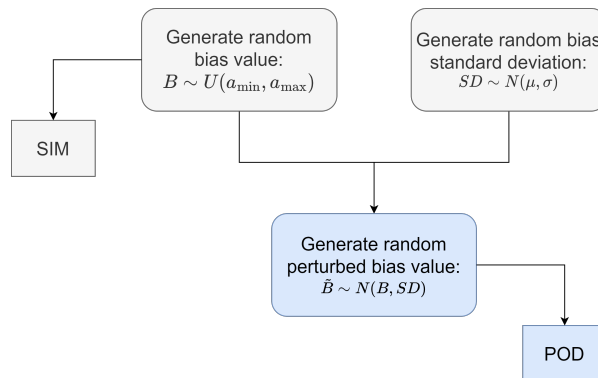


**Figure 5.11:** Diagram showing the methodology followed to simulate the unperturbed and perturbed bias values used in simulation and estimation, respectively.  $U$  stands for uniform distribution, and  $N$  for normal distribution.

To determine the standard deviations, an analysis was conducted on the behaviour of the bias standard deviations provided by CODE's final bias products. It was found that the standard deviations of the code biases followed a normal distribution  $SD_{PR}^s \sim N(\mu = 0.02, \sigma = 0.001)$  ns. As for the emitter phase biases, it was observed that their standard deviations were always set to zero in the CODE bias files. Nonetheless, it was decided to perturb these biases to explore the potential impact of uncertainty in the emitter phase biases on the POD process. After conducting various experiments,

it was determined that the standard deviation of the emitter phase biases should follow a distribution of  $SD_{CP}^s \sim N(\mu = 10^{-4}, \sigma = 10^{-5})$  ns.

The receiver instrumental biases, on the other hand, are not used in the POD process and thus they do not need to be perturbed. It is assumed that these biases are eliminated through single-satellite differencing during single-receiver ambiguity resolution. Therefore, there is no need to introduce perturbations to the receiver biases as they are not explicitly included in the POD process.

#### 5.3.4. Errors in the GNSS Orbits and Clocks

In real-world scenarios, the precise orbits and clocks of GNSS satellites are provided by analysis centres, such as IGS analysis centres. Although IGS products are highly precise, they are not free from errors. As such, to conduct realistic simulations, it is important to model the errors present in these orbits and clocks. This section explains the method used to model these errors in this thesis. This model is used to perturb the reference GNSS orbits and clocks presented in Section 5.1. The non-perturbed products are employed to simulate the observations, while the perturbed ones are used in the orbit determination process.

The GNSS ephemerides contain systematic once-per-revolution errors that result mainly from unmodeled forces. These errors tend to be harmonics of the orbital period in the radial, along-track, and cross-track orbital directions (Colombo, 1989; Urschl et al., 2007). As a result, the orbital errors are introduced in the QSW frame. The ephemerides also exhibit time-correlated errors due to unmodeled time-varying effects (Olynik et al., 2002). The most common way to simulate these time-correlated errors is through a Gauss-Markov process (Petovello et al., 2009). Therefore, the orbital errors can be split into two contributions: a harmonic contribution  $\Delta \mathbf{r}_{harm}$  and a Gauss-Markov contribution  $\Delta \mathbf{r}_{GM}$ .

$$\Delta \mathbf{r}(t) = \Delta \mathbf{r}_{harm}(t) + \Delta \mathbf{r}_{GM}(t) \quad (5.10)$$

The harmonic contribution in each direction of the QSW frame can be described by Equation 5.11:

$$\Delta r_{harm,i}(t) = A_{m,i} \cos \left( 2\pi \frac{t - t_0}{T} + \varphi_i \right), \quad i = \{Q, S, W\} \quad (5.11)$$

where  $\Delta r_{harm,i}(t)$  is the harmonic orbital error being generated at time  $t$ ,  $t_0$  is the initial time of the orbit,  $T$  is the orbital period,  $A_m$  is the amplitude error, and  $\varphi$  is the phase error. The amplitude error is a random variable normally distributed  $A_m \sim N(0, \sigma_A)$ , and the phase error is also a random variable normally distributed  $\varphi \sim N(0, 2\pi)$ .

On the other hand, the Gauss-Markov contribution in each direction of the QSW frame can be modeled using the Equation 5.12:

$$\Delta r_{GM,i}(t_k) = \Delta r_{GM,i}(t_{k-1}) e^{-(t_k - t_{k-1})/\tau_r} + \sqrt{1 - e^{-2(t_k - t_{k-1})/\tau_r}} v_i(t_k), \quad i = \{Q, S, W\} \quad (5.12)$$

where  $\Delta r_{GM,i}$  represents the Gauss-Markov orbital error being generated, and  $t_k$  and  $t_{k-1}$  denote the times of consecutive epochs. The subscript  $k$  is used because the error is time-correlated. The parameter  $\tau_r$  represents the correlation time of the process, and  $v$  is an uncorrelated random noise that follows a normal distribution  $v \sim N(0, \sigma_v)$ .

After obtaining the errors in position, they are transformed to a Cartesian inertial frame to compute the errors in the velocity. This is achieved by taking into account that the orbital velocity of a GNSS satellite is typically three orders of magnitude lower than its position, and thus the error should also be three orders of magnitude lower. Equations 5.13, 5.14 and 5.15 represent the transformation of the errors in position to errors in velocity in the  $x$ ,  $y$ , and  $z$  directions, respectively:

$$\Delta v_x = \Delta r_y / 1000 \quad (5.13)$$

$$\Delta v_y = \Delta r_x / 1000 \quad (5.14)$$

$$\Delta v_z = \Delta r_z / 1000 \quad (5.15)$$

Regarding GNSS clock errors, they are correlated with orbit errors due to the coupling of clock estimation with the radial component of the position. Thus, GNSS clock errors also exhibit a harmonic behaviour associated with radial position errors (Senior et al., 2008). Furthermore, clock errors display a time-correlated behaviour (Olynik et al., 2002). As a consequence, clock errors can be modeled as a

combination of an orbit-related component  $\Delta\delta_{orb}(t)$  and a Gauss-Markov process  $\Delta\delta_{GM}(t)$ , as shown in Equation 5.16.

$$\Delta\delta(t) = \Delta\delta_{orb}(t) + \Delta\delta_{GM}(t) \quad (5.16)$$

The orbital-related component of clock errors is associated with the radial orbit error described in Equation 5.11. This component can be computed using the expression:

$$\Delta\delta_{orb}(t) = \frac{\Delta r_{harm,Q}(t)}{c} = \frac{A_{m,Q}}{c} \cos\left(2\pi \frac{t-t_0}{T} + \varphi_Q\right) \quad (5.17)$$

where  $\Delta r_{harm,Q}$  is the radial harmonic orbital error, and  $c$  is the speed of light.

The Gauss-Markov clock error is expressed as:

$$\Delta\delta_{GM}(t_k) = \Delta\delta_{GM}(t_{k-1})e^{-(t_k-t_{k-1})/\tau_\delta} + \sqrt{1 - e^{-2(t_k-t_{k-1})/\tau_\delta}}w(t_k) \quad (5.18)$$

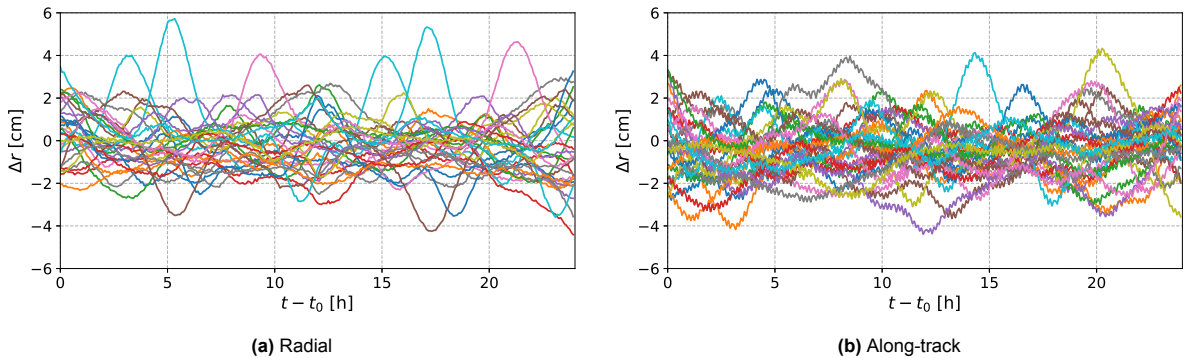
where  $\Delta\delta_{GM}$  is the Gauss-Markov clock error being generated,  $t_k$  and  $t_{k-1}$  are the times of consecutive epochs,  $\tau_\delta$  is the correlation time of the process, and  $w$  is the uncorrelated random noise that follows a normal distribution  $w \sim N(0, \sigma_w)$ .

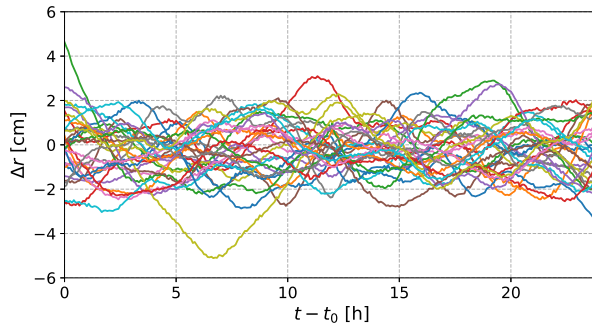
The model provides several degrees of freedom to characterize the GNSS orbit and clock errors, namely the standard deviations of  $A_m$  ( $\sigma_A$ ),  $v$  ( $\sigma_v$ ) and  $w$  ( $\sigma_w$ ), as well as the orbit and clock Gauss-Markov correlation times ( $\tau_r$  and  $\tau_\delta$ ). Regarding the orbit error parameters, the same values of  $\sigma_A$ ,  $\sigma_v$ , and  $\tau_r$  are employed for each direction within the QSW frame.

These parameters must be carefully selected to introduce realistic errors into the analysis. To achieve this, the orbit and clock products from two analysis centres — CODE and GFZ (German Research Centre for Geosciences) — have been compared to gain insights into the order of magnitude and time behaviour of these errors. Subsequently, the parameters of the model were adjusted to ensure that the comparison between the reference and perturbed orbits and clocks closely aligns with the comparisons between the different analysis centres.

The radial, along-track, and cross-track differences between the final GPS orbit products provided by CODE and GFZ on 08/01/2023 are shown in Figure 5.12, along with the corresponding statistics in Table 5.7. The results obtained for the rest of the week from 08/01/2023 to 14/01/2023 were similar. The Galileo satellites also exhibited a similar behaviour.

Based on Figure 5.12, it can be observed that the orbit comparisons present a sinusoidal shape in the radial, along-track, and cross-track directions, with a period matching the orbital period. Since the developed model assumes a unique Gauss-Markov standard deviation for all components, and no significant Gauss-Markov behaviour is observed in the radial and cross-track directions, it is reasonable to set  $\sigma_v = 0$ . Although a slight Gauss-Markov behaviour is observed in the along-track component, it is relatively minor compared to the harmonic error, and considering the simplification of the model, this effect is neglected. Additionally, Table 5.7 shows that the averages of the errors are non-zero, but this effect is not included in the developed model.





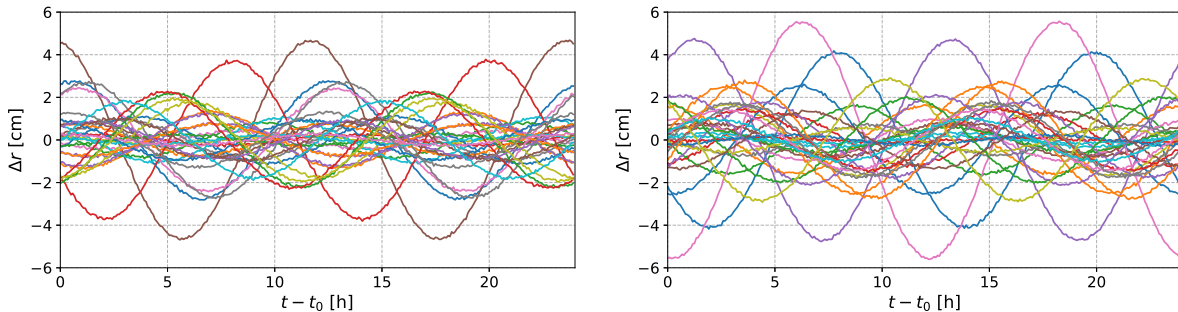
(c) Cross-track

**Figure 5.12:** Comparison between the CODE and GFZ final GPS orbit products on 08/01/2023 in the radial, along-track, and cross-track directions. Each line represents a different GPS satellite.

Component	Mean [mm]	RMS [mm]	Max [mm]	Sigma [mm]
Radial	-2.09	11.62	57.25	9.07
Along	-3.98	12.49	43.93	11.22
Cross	-2.36	11.07	51.13	9.87

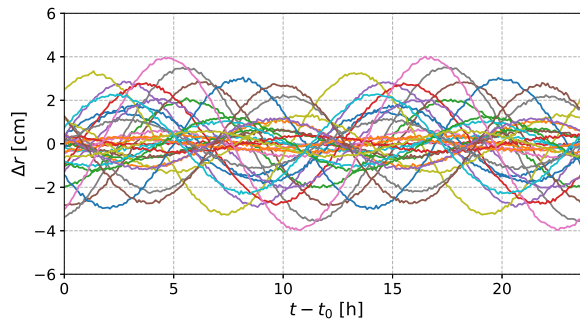
**Table 5.7:** Statistics of the comparison between CODE and GFZ final GPS orbits on 08/01/2023 in the radial, along-track, and cross-track directions.

After conducting some trial and error, it was determined that the optimal standard deviation for the amplitude error is  $\sigma_A = 0.02$  m. In Figure 5.13, the comparison between the reference GNSS orbits and the perturbed GNSS orbits using  $\sigma_A = 0.02$  m and  $\sigma_v = 0$  m is shown. It is worth noting that the correlation time is not relevant in this case, as the Gauss-Markov orbital errors are neglected.



(a) Radial

(b) Along-track



(c) Cross-track

**Figure 5.13:** Comparison between the reference GNSS orbits and the perturbed GNSS orbits using  $\sigma_A = 0.02$  m and  $\sigma_v = 0$  m in the radial, along-track, and cross-track directions. Each line represents a different GNSS satellite.

Although it was not expected for the simulated orbital errors to match the real ones shown in Figure 5.12 precisely, as the model does not fully encompass all the complexities of the real problem, it can be observed that the model still captures the order of magnitude and periodic shape of the errors. The comparison statistics between the reference and perturbed GNSS orbits are presented in Table 5.8.

Component	Mean [mm]	RMS [mm]	Max [mm]	Sigma [mm]
Radial	-0.03	8.99	46.88	8.94
Along	-0.16	12.48	56.03	12.41
Cross	-0.20	12.03	57.54	11.96

**Table 5.8:** Statistics of the comparison between the reference GNSS orbits and the perturbed GNSS orbits during one day with  $\sigma_A = 0.02$  m and  $\sigma_v = 0$  m.

For the IGS clock product analysis, the CODE and GFZ final clock products with a rate of 30 s were used. Figures 5.14a and 5.14b show the comparison between these clocks for GPS and Galileo, respectively, from 08/01/2023 to 14/01/2023. In these comparisons, an epoch-wise radial correction based on the associated orbit has been applied to remove the orbit-related clock errors. As shown in these figures, the clock biases jump each day. This occurs because clock biases are computed using a station clock as reference, with each day having a different station chosen and each station having different instrumental biases. Moreover, each analysis centre uses a different station, causing the clock comparisons to follow a different drift each day. An anomalous behaviour is observed for the GPS clocks on 09/01/2023, but explaining this behaviour is out of the scope of this thesis. To better illustrate the daily behaviour, Figure 5.15 presents the comparison of the Galileo clocks on 08/01/2023.

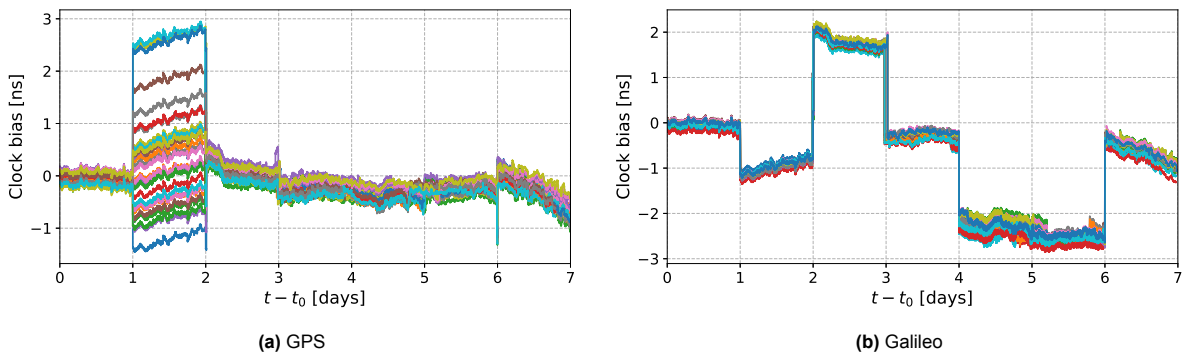


**Figure 5.14:** Comparison of GPS and Galileo clocks between CODE and GFZ analysis centres for the period from 08/01/2023 to 14/01/2023, with the orbit-related clock errors removed. Each line represents a different clock.

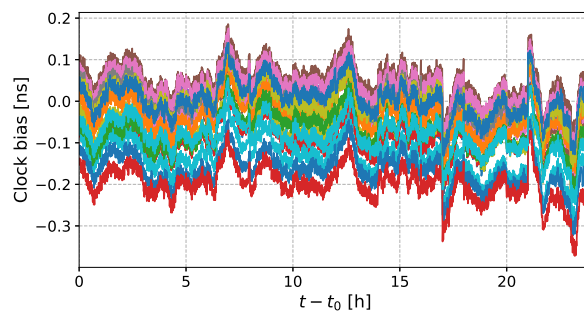


**Figure 5.15:** Comparison of Galileo clocks between CODE and GFZ analysis centres on 08/01/2023, with the orbit-related clock errors removed. Each line represents a different clock.

The analysis revealed that the standard deviation of the clock comparison for both GPS and Galileo was approximately 65 ps. To match the observed IGS clock error, the clock Gauss-Markov standard deviation  $\sigma_w$  and correlation  $\tau_\delta$  parameters were adjusted. After several trials, it was found that setting

$\sigma_w = 70$  ps and  $\tau_\delta = 30$  min resulted in a standard deviation of the clock comparison matching the observed value of 65 ps. Figure 5.16 displays the comparison between a reference and perturbed simulated clock, illustrating the behaviour achieved through the adjustment of the clock perturbation parameters.

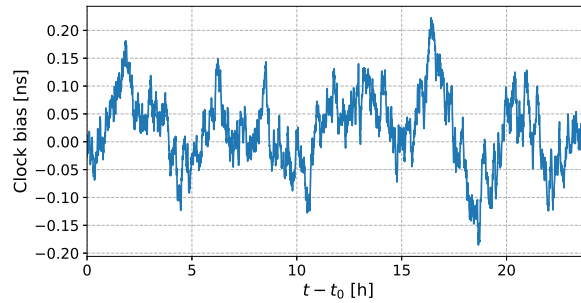


**Figure 5.16:** Comparison between the reference and perturbed clocks for one GNSS satellite using the tuned Gauss-Markov parameters  $\sigma_w = 70$  ps and  $\tau_\delta = 30$  min. The orbit-related clock errors have been removed using an epoch-wise radial correction.

The obtained results are consistent with what is typically reported in the literature. Senior et al. (2008) highlight two key observations regarding the precision of IGS orbits and clocks. Firstly, the internal precision of IGS orbits and clocks is typically around 1 cm (33 ps) one-dimensional RMS. Secondly, if the errors in the orbits and clocks are primarily sinusoidal, a 1 cm RMS error would correspond to an amplitude of 1.5 cm (50 ps). The results obtained in this study align with this estimation, as the one-dimensional orbit error RMS is at the 1 cm level, while the clock errors appear to be slightly higher at 70 ps compared to the expected 50 ps.

Table 5.9 presents the values that were finally chosen for the parameters involved in modeling the GNSS orbit and clock errors. In Chapter 8, a sensitivity analysis will be conducted to evaluate the impact of changes in these parameters on the accuracy of the orbit determination.

Parameter	Nominal value
$\sigma_A$ [m]	0.02
$\sigma_v$ [m]	0
$\sigma_w$ [ps]	70
$\tau_\delta$ [min]	30

**Table 5.9:** Nominal values of the parameters used in the modeling of GNSS orbit and clock errors.

### 5.3.5. Laser Noise

In Chapter 3, the challenges associated with modeling laser noise in the intersatellite link were discussed. Due to the lack of precise information about the ISL instrument characteristics, it is difficult to develop an accurate model of laser error sources related to frequency instability, satellite vibrations, tracking errors, and background noise. As a result, in this study, these effects are modeled as random white Gaussian noise with a standard deviation similar to state-of-the-art optical ISL precision, which is 1 mm in the nominal scenario.

### 5.3.6. Uncertainties in the Geopotential Model

To simulate uncertainties in the geopotential model, a different model will be used for the simulation and estimation phases. These models provide the spherical harmonic coefficients of the Earth's gravity field. Specifically, the 'COST-G' (Combination Service for Time-variable Gravity fields) model will be employed in the generation of the reference orbits and simulation of the observations, while the 'EIGEN-GRGS.RL04.MEAN-FIELD.quadratic\_mean\_pole' (European Improved Gravity model of the Earth by New techniques) model will be used in the orbit determination process.

The difference between these two geopotential models becomes larger as time progresses. The increasing discrepancies between the geopotentials are due to the fact that the COST-G model is

regularly updated every four months, incorporating time-dependent terms, whereas the EIGEN model has not changed since 2019. Thus, two different scenarios will be explored to quantify the effect of the uncertainties in the geopotential. In the first scenario, the orbit determination will be performed for a reference epoch in 2017, when the difference between the two models is relatively small. In the second scenario, the analysis will be performed for a reference epoch in 2022, when the two models are more dissimilar.

### 5.3.7. Uncertainties in the Solar Radiation Pressure Model

The uncertainties in the SRP model arise mainly from a lack of accurate knowledge about the geometry and optical characteristics of the spacecraft. To simulate these uncertainties, two distinct models for the SRP acceleration will be employed during the simulation and estimation stages. An analytical box-wing model will be used in simulation and an empirical ECOM model in estimation.

Selecting the appropriate ECOM model for accurate estimation of the solar radiation pressure effect is not a straightforward task. It requires careful evaluation to determine whether the proposed ECOM-SGRA model outperforms the standard ECOM model in capturing the influence of SRP. Furthermore, it is necessary to determine the optimal number of ECOM coefficients needed for the estimation and consider whether dividing the estimation arc into sub-intervals, with each sub-interval associated with a different set of ECOM coefficients, would enhance the ability to capture the variations in SRP effect more effectively.

## 5.4. Precise Orbit Determination Process

The purpose of this section is to explain the methodology followed in the estimation process of the problem. A simplified overview of the various steps involved in this process is depicted in Figure 5.17. This section will provide a description and analysis of each step, enabling a thorough understanding of the entire procedure applied to estimate the orbits of the EHI satellites.

### 5.4.1. GNSS-only POD

The initial step of the orbit determination process involves the pre-processing of the GNSS observations. This pre-processing stage encompasses various tasks, such as generating the ionospheric-free combination, applying specific criteria to discard certain observations, and detecting the passes. In the final pre-processing step, the global positioning system equations are solved using the Bancroft algorithm, which is known for providing an estimate for the state vector with the minimum RMS error through a kinematic approach (Bancroft, 1985). This algorithm exclusively employs the ionospheric-free pseudorange observables.

The state vector obtained from the Bancroft algorithm serves as the starting state for the Single Point Positioning (SPP) estimation. Alongside the state vector, the Cartesian XYZ observations generated by this algorithm are also used in the SPP estimation. Compared to the POD estimation, the SPP employs a simpler dynamical model and estimates only the initial state vector. The main goal of the SPP is to quickly obtain a preliminary orbit that is used as input for the subsequent POD process.

The POD process employs the initial state vectors obtained from the SPP estimation as the starting point. It is important to remark that a separate POD process is carried out for EHI-1 and EHI-2. The POD estimation uses the same propagation model as the one employed for generating the reference orbits, except when accounting for uncertainties in the dynamical model. The POD estimation incorporates the ionospheric-free code and phase observations, as well as the GNSS orbits and clocks, to estimate the initial state vector, phase ambiguities, receiver clock biases, and dynamical coefficients if applicable.

After the float estimation, the next step involves the integer fixing of the ambiguities using the strategy outlined in Section 4.3. This process resolves the integer ambiguities present in the phase observations, further refining the accuracy of the estimated orbits. With the ambiguities fixed, a subsequent iteration of the POD scheme is performed, using the same methodology as before but with the integer ambiguities held constant.

As a result of the GNSS-only POD process, the estimated orbits and clocks of EHI-1 and EHI-2 are obtained, comprising both the float and fixed solutions. The relative orbit of EHI-2 with respect to EHI-1 is then derived by subtracting the absolute orbit of EHI-2 from that of EHI-1. This relative orbit can be computed based on the GNSS-only float solutions of EHI-1 and EHI-2, as depicted in Equation 5.19. Alternatively, the relative orbit can be computed using the GNSS-only fixed solutions of EHI-1

and EHI-2, as shown in Equation 5.20.

$$\Delta \mathbf{r}_{1/2, \text{GNSS-only float}} = \mathbf{r}_{2, \text{GNSS-only float}} - \mathbf{r}_{1, \text{GNSS-only float}} \quad (5.19)$$

$$\Delta \mathbf{r}_{1/2, \text{GNSS-only fixed}} = \mathbf{r}_{2, \text{GNSS-only fixed}} - \mathbf{r}_{1, \text{GNSS-only fixed}} \quad (5.20)$$

#### 5.4.2. GNSS+ISL POD

In the next step of the estimation process, the ISL observations are introduced along with the GNSS observations to potentially improve the precision in estimating the orbit and clock parameters of EHI-2. During this estimation, the orbit and clock of EHI-1 are constrained to the fixed solution obtained from the GNSS-only POD. The fixed solution is chosen over the float solution due to its expected higher accuracy. In this POD, the initial state of EHI-2, the clocks of EHI-2, the GNSS float ambiguities, and, if applicable, dynamical coefficients are re-estimated.

The float solution obtained from the GNSS+ISL POD process serves as the input for the integer ambiguity resolution algorithm, enabling the determination of the GNSS+ISL fixed solution for EHI-2. Next, the relative orbit between EHI-1 and EHI-2 is computed using the GNSS-only fixed orbit of EHI-1 and the GNSS+ISL fixed orbit of EHI-2, as illustrated in Equation 5.21. It should be noted that computing the GNSS+ISL float relative orbit would have required to use the float solution for EHI-1 as input in the GNSS+ISL POD process. However, for computational efficiency and considering the expected higher accuracy of the fixed solution, only the fixed EHI-1 solution is employed. Thus, the GNSS+ISL float relative orbit is not computed in this case.

$$\Delta \mathbf{r}_{1/2, \text{GNSS+ISL fixed}} = \mathbf{r}_{2, \text{GNSS+ISL fixed}} - \mathbf{r}_{1, \text{GNSS-only fixed}} \quad (5.21)$$

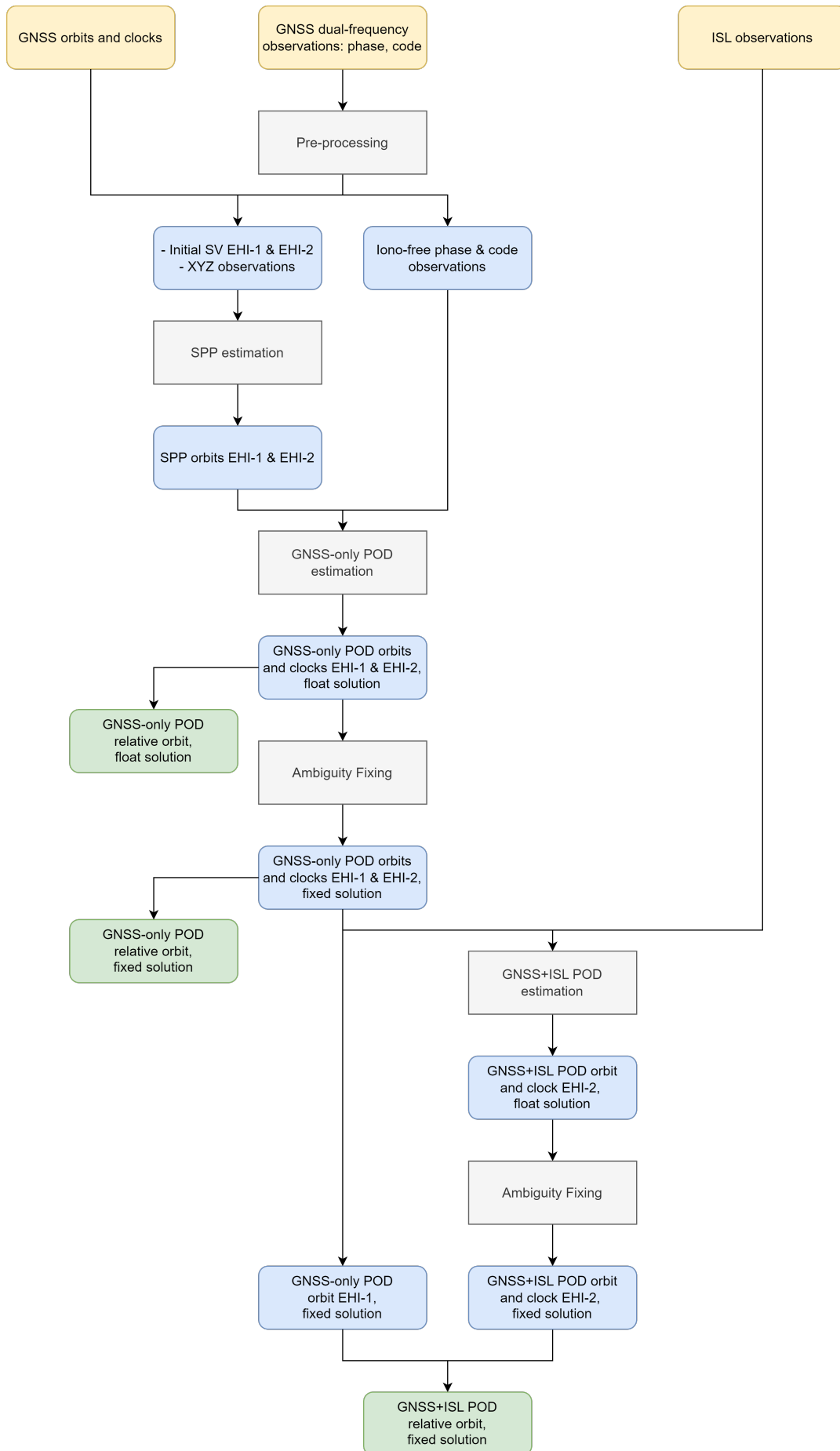


Figure 5.17: Diagram of the steps of the orbit determination process.

## Results: Perfect Modeling

This chapter provides an in-depth analysis of the results obtained from the Precise Orbit Determination (POD) process under the assumption of perfect modeling. In this context, perfect modeling refers to the absence of errors in the observations, GNSS products, and dynamical model. The main objective of this chapter is to validate the methodology by comparing the estimated orbits with the reference orbits, which are expected to align almost perfectly in this ideal scenario.

The POD results presented in this chapter were computed using the MAORI software, which has proven to be a robust tool for accurate orbit estimation. However, to further ensure the reliability and validate the obtained simulation results, a verification process has been conducted using the NAPEOS software package. The tools developed by GMV (2022) within the NAPEOS software were used for this purpose. By employing these tools, a thorough comparison of the estimated orbits was conducted, adding an additional layer of confidence to the findings presented in this chapter.

The chapter begins with an explanation of the selection of the reference scenarios. Next, the validation of the reference orbits that serve as the benchmark for evaluating the accuracy of the estimated orbits is introduced. The chapter then covers the results of the GNSS-only POD and the GNSS+ISL POD, assessing their accuracy against the reference orbits. It is important to note that, in this error-free scenario, the GNSS+ISL POD utilizes the GNSS-only float solution of EHI-1 as a reference, as integer ambiguity resolution has not yet been introduced during this stage of the validation process. Finally, the last section investigates the impact of integer ambiguity resolution to examine its influence on the results. By examining the outcomes obtained under ideal modeling conditions, a fundamental understanding of the capabilities of the POD methodology can be established.

### 6.1. Selection of Reference Scenarios

The analysis of the entire month of April throughout this report, including all the scenarios and results, would be excessively time-consuming. Therefore, for the purpose of Chapters 6 and 7, it was decided to focus on three particular scenarios that represent three different baseline distances. Each scenario covers one day, i.e., a 24-hour arc. The evolution of the relative distance between EHI-1 and EHI-2 during April 2022 is depicted in Figure 6.1.

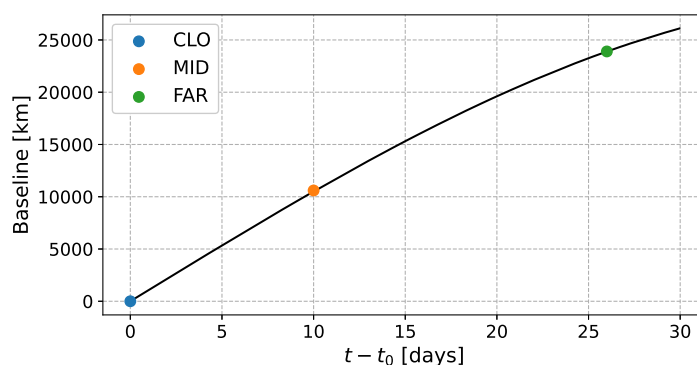


**Figure 6.1:** Evolution of the baseline between EHI-1 and EHI-2 over the month of April 2022, with the three different scenarios highlighted.

At the beginning of the simulation, the two satellites are closest to each other, after which they gradually move apart due to their offset in altitude, eventually reaching intersatellite distances of up to 25,000 km. Recall that during this whole month the visibility between both EHIs has been ensured, as explained in Section 1.2.5.

According to Figure 6.1, three scenarios have been defined, each representing a different order of magnitude of the intersatellite distance. The first one is named CLO because the satellites are the closest to each other and the baseline distance evolves from 23.3 km up to 1,000 km. In the second scenario, MID, the baseline distance is around 10,000 km and in the FAR scenario this distance is approximately 23,500 km. The time arc of the three scenarios together with the baseline distance range are gathered in Table 6.1.

Scenario	Start date	End date	Baseline start [km]	Baseline end [km]
CLO	01/04/2022 00:00:00 GPS	02/04/2022 00:00:00 GPS	23.3	1,074
MID	10/04/2022 00:00:00 GPS	11/04/2022 00:00:00 GPS	9,492	10,501
FAR	26/04/2022 00:00:00 GPS	27/04/2022 00:00:00 GPS	23,252	23,889

**Table 6.1:** Characteristics of the three reference scenarios.

## 6.2. Reference Orbits

The initial stage of the study involves generating the reference orbits, which serve as the true representation of the actual orbits of the EHI spacecraft. These orbits are propagated using the dynamical model outlined in Section 5.1. To ensure the correctness of this generation process, the simulated reference orbits are compared against the reference orbits calculated with the NAPEOS software using the same problem configuration. Figures 6.2a and 6.2b present the results of this comparison for the absolute orbits of EHI-1 and EHI-2 in the CLO scenario, illustrating the differences in three-dimensional (3D) position. Similar outcomes were observed for the MID and FAR scenarios.

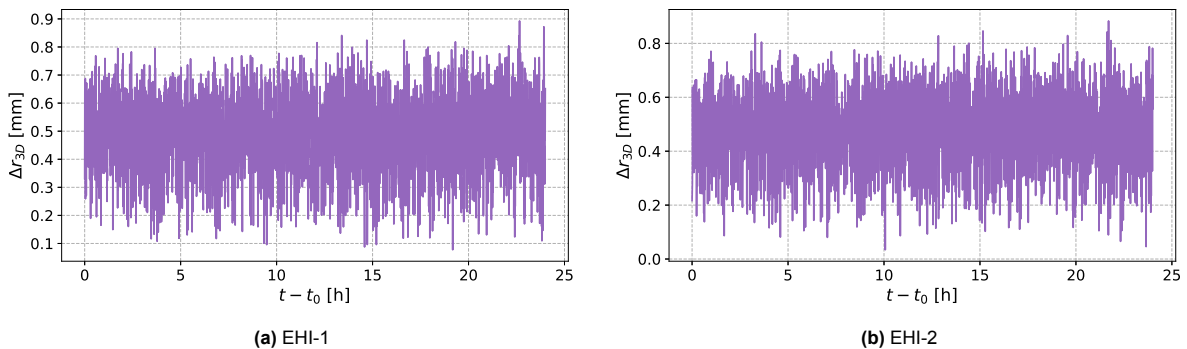


**Figure 6.2:** Comparison of the reference orbits generated by MAORI against the reference orbits generated by NAPEOS for EHI-1 and EHI-2 in the CLO scenario. The comparison is done in terms of the three-dimensional position difference.

The comparison reveals that the differences between the generated reference orbits and the NAPEOS-calculated reference orbits are consistently below 1 mm. This limitation arises due to the resolution of the orbit files used in the simulation in NAPEOS, which stores the orbits with a precision of 1 mm (SP3 file format). Therefore, it can be stated that the reference orbits generated using MAORI and NAPEOS coincide, thereby validating the successful generation of these orbits.

## 6.3. Results Perfect GNSS-only POD

The results of the perfect GNSS-only POD process, which exclusively considers GNSS observations, are presented in this section. The initial state of the EHIs, the EHI clocks, and the float ambiguities are estimated during this POD. In order to validate the POD process, a comparison is made between the GNSS-only POD orbits estimated by MAORI against the orbits estimated with NAPEOS using the tools developed by GMV (2022). It is important to note that the latter orbits were recomputed specifically for

this study, ensuring the use of the same dynamical model settings and including the same effects in the generation of the clocks and observations.

Figures 6.3a and 6.3b depict the comparison results for EHI-1 and EHI-2 orbits in the CLO scenario, showcasing the discrepancies in 3D position between the orbits estimated by MAORI and NAPEOS. Similar findings were observed for the remaining scenarios. As discussed in the previous section, the comparison precision is limited to 1 mm due to the resolution of the orbit files used in NAPEOS.

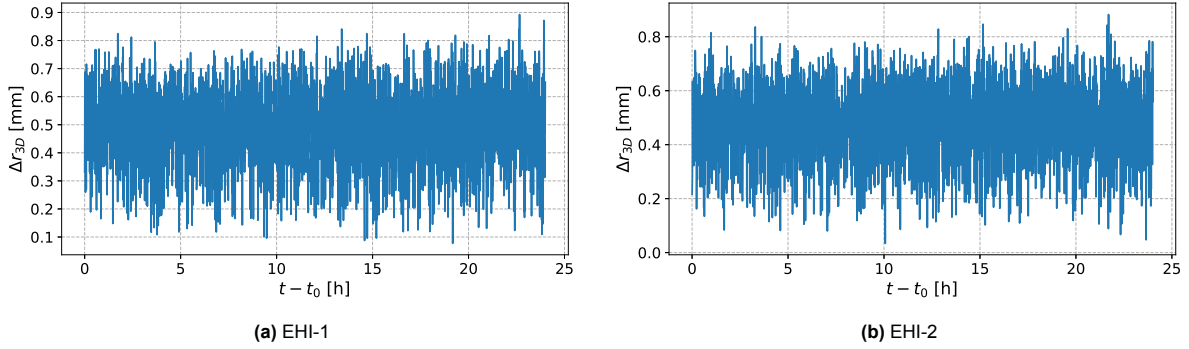


**Figure 6.3:** Comparison of the GNSS-only POD orbits estimated by MAORI against the orbits estimated by NAPEOS for EHI-1 and EHI-2 in the CLO scenario. The comparison is done in terms of the three-dimensional position difference.

To assess the accuracy of the POD estimation, a comparison is conducted between the POD orbits and the reference orbits, using both MAORI and NAPEOS. The results of this comparison, focusing on the difference in 3D position, are depicted in Figures 6.4a and 6.4b for EHI-1 and EHI-2, respectively, in the CLO scenario. Additionally, Figure 6.4c illustrates the comparison of the relative orbit, which corresponds to the orbit of EHI-2 relative to that of EHI-1 (EHI-1/2). The relative orbit holds significant importance in this project as it determines the feasibility of meeting the relative navigation requirements. Similar results were obtained for the MID and FAR scenarios.

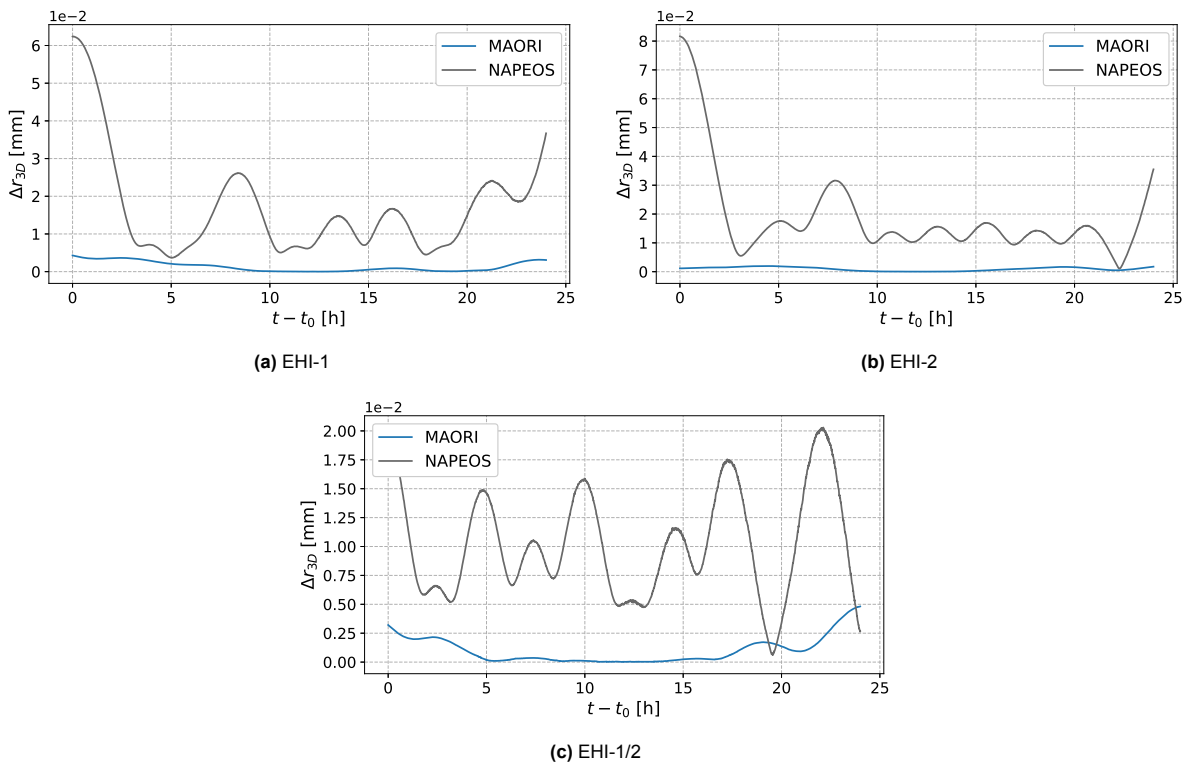


**Figure 6.4:** Comparison between the GNSS-only POD orbits and the reference orbits for EHI-1, EHI-2 and EHI-1/2 in the CLO scenario, computed using both MAORI and NAPEOS. The comparison is done in terms of the three-dimensional position difference.

The observed discrepancy between the MAORI and NAPEOS results can be attributed to the contrasting data model architectures employed by these software, as discussed in Section 4.4. The architecture of NAPEOS lacks clear separation between data and algorithms, requiring a continuous reading and writing of files to exchange information between tools. This leads to a loss of precision due to the inherent resolution of data files. In contrast, MAORI employs a centralized data model that stores all the data in a unified layer accessible to all algorithms, eliminating the need for file-based data transfer and ensuring that precision is preserved throughout the process.

Figure 6.5 presents the same comparison as before, focusing solely on the orbits computed by MAORI to provide a clearer view of the results. The displayed orbits exhibit accuracy at the micrometre level, with the slight discrepancies mainly attributed to numerical noise. Notably, the error is lower in the middle of the 24-hour interval, corresponding to the location where the initial state vector is estimated, and increases towards the interval ends. Although extending the interval by a few hours could address this issue, it was not considered necessary at this stage of the result generation process. This adjustment will be performed in subsequent analyses involving more complex setups and the inclusion of error sources.

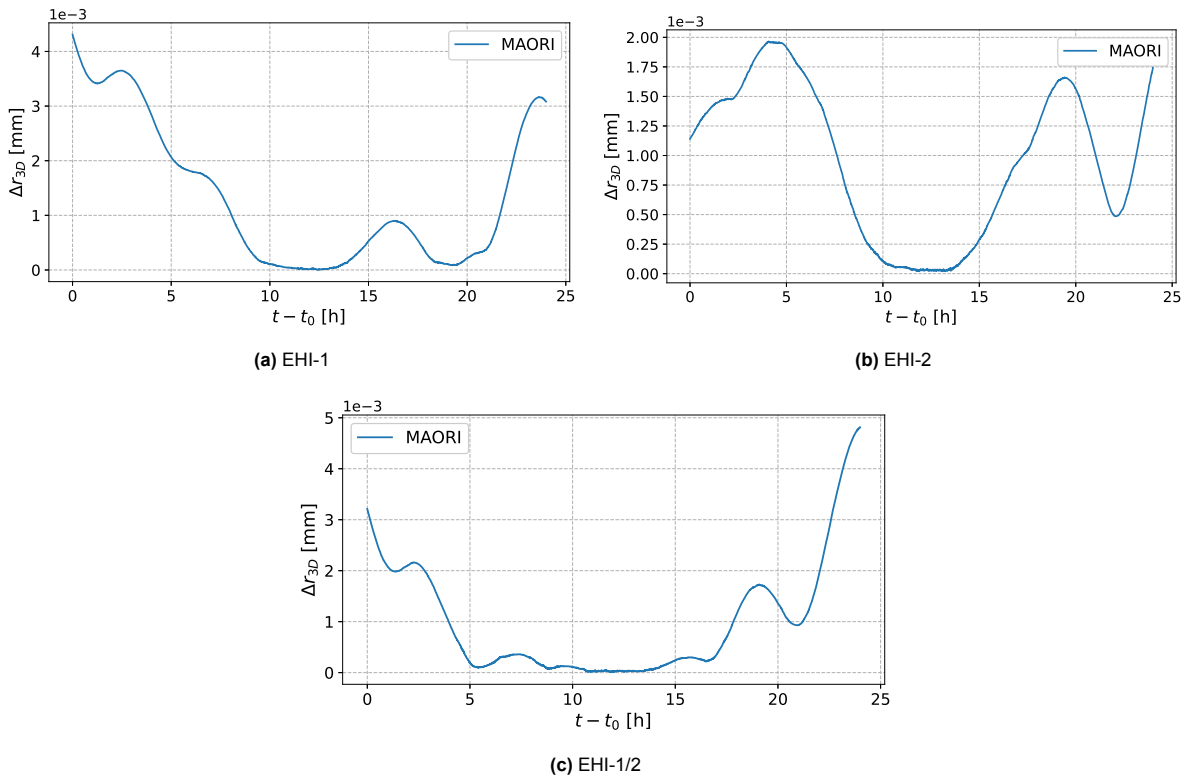


**Figure 6.5:** Comparison between the MAORI-computed GNSS-only POD orbits and the reference orbits for EHI-1, EHI-2 and EHI-1/2 in the CLO scenario. The comparison is done in terms of the three-dimensional position difference.

## 6.4. Results Perfect GNSS+ISL POD

This section presents the results of the perfect GNSS+ISL POD estimation, which is performed with the orbit of EHI-1 kept fixed while re-estimating the orbit of EHI-2. The set of estimated parameters remains the same as in the GNSS-only POD. Once again, to check the correctness of this POD process, a comparison is conducted between the GNSS+ISL POD orbits estimated using MAORI and the orbits estimated by NAPEOS. The comparison revealed the expected agreement between the orbits obtained with the two different software packages, with a fit at the 1 mm-level.

The next step involves comparing the GNSS+ISL POD orbits with the reference orbits computed using both MAORI and NAPEOS. Figures 6.6a and 6.6b present the results of this comparison for EHI-2 and EHI-1/2 in the CLO scenario. These results once again highlight the limitations of NAPEOS in terms of data transfer, which adversely affect the achievable accuracy of the solution. Consequently, MAORI is selected as the preferred software for the remainder of this project due to its absence of this

limitation. The results also demonstrate that the accuracy of the GNSS+ISL POD orbits obtained with MAORI is still at the micrometre level, which indicates that the ISL observations have been implemented correctly.

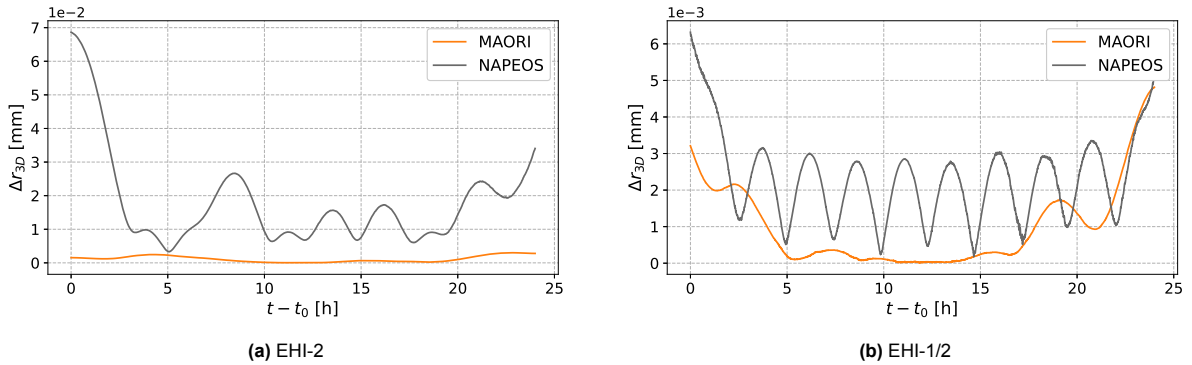


**Figure 6.6:** Comparison between the GNSS+ISL POD orbits and the reference orbits for EHI-2 and EHI-1/2 in the CLO scenario, computed using both MAORI and NAPEOS. The comparison is done in terms of the three-dimensional position difference.

## 6.5. Ambiguity Fixing

The results of the estimation after applying integer ambiguity resolution, which involves fixing the ambiguities to integer values, are now presented. Ambiguity fixing is performed after the GNSS-only POD estimation to resolve the ambiguities in the GNSS observations. Once the ambiguities are fixed, an additional POD process is carried out using these fixed ambiguities, resulting in the GNSS-only fixed solutions for both EHI-1 and EHI-2. These fixed solutions are then used to compute the GNSS-only fixed solution for the relative orbit EHI-1/2. The comparison of these fixed solutions and the float solutions with the reference orbits is shown in Figure 6.7. It can be observed that the accuracy of the fixed solution is similar to that of the float, and any discrepancies between them are primarily attributed to numerical noise.

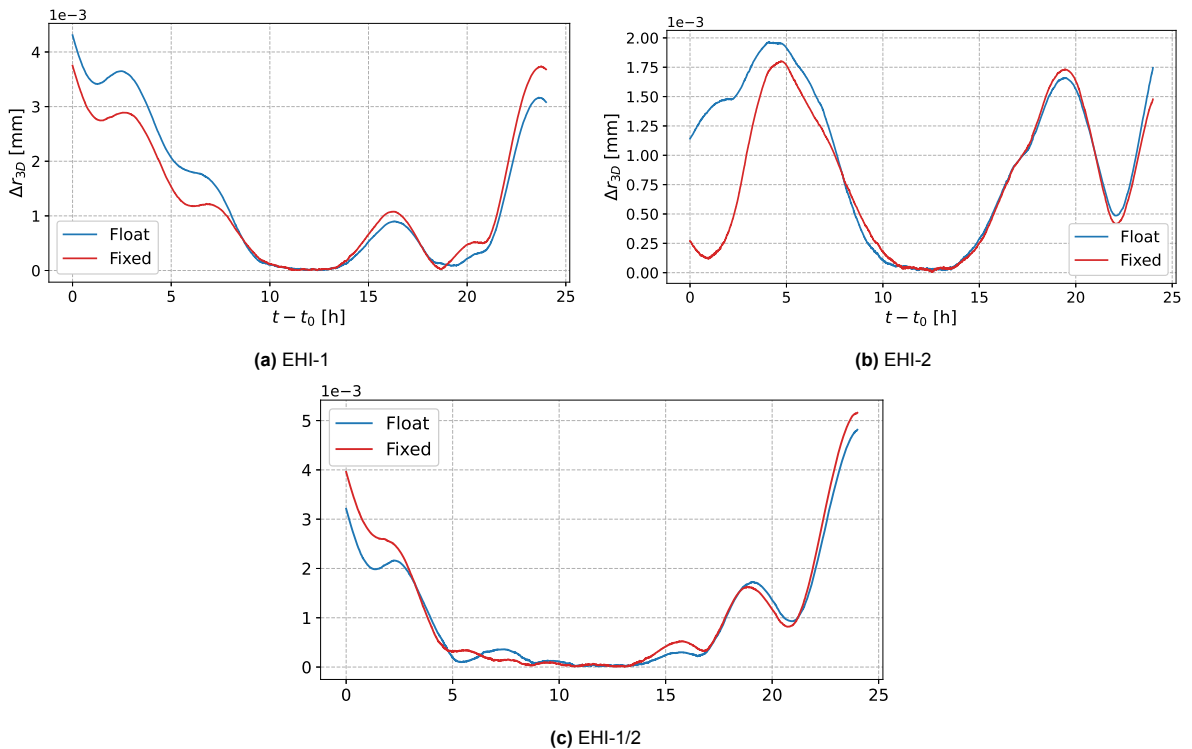


**Figure 6.7:** Comparison of the GNSS-only fixed and float orbits with the reference orbits in the CLO scenario. The comparison is done in terms of the three-dimensional position difference.

Following the GNSS+ISL float estimation process, ambiguity fixing is also performed for this solution. The fixed ambiguities are then used in an additional POD process to obtain the GNSS+ISL fixed solution for EHI-2. The GNSS-only fixed solution for EHI-1 and the GNSS+ISL fixed solution for EHI-2 are combined to compute the GNSS+ISL fixed solution for the relative orbit EHI-1/2. The comparison of these fixed solutions with the reference orbits is illustrated in Figure 6.8, which also includes the comparison of the float solutions with the reference. Once again, it can be seen that the accuracy of the fixed solution is similar to that of the float solution.

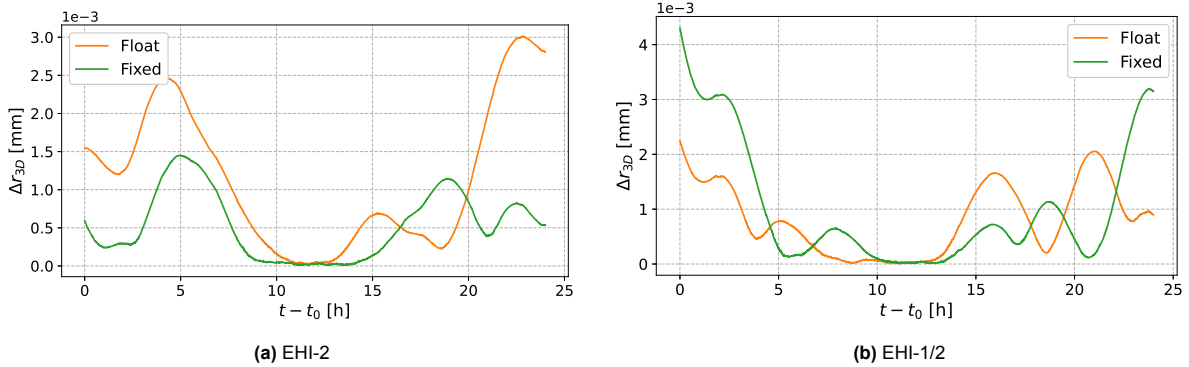


**Figure 6.8:** Comparison of the GNSS+ISL fixed and float solutions with the reference orbits in the CLO scenario. The comparison is done in terms of the three-dimensional position difference.

Based on the analysis conducted with perfect modeling, the impact of integer ambiguity resolution is not clear, as the achieved precision in both float and fixed cases is already close to the level of numerical noise. However, it is important to note that this assessment may change when realistic errors are introduced into the problem. Therefore, further investigation is needed in the next chapter to explore the impact of integer ambiguity resolution and evaluate its effectiveness in the presence of error sources.

One important aspect of the integer ambiguity resolution process is the percentage of ambiguities successfully fixed to an integer value. Table 6.2 presents these percentages for each instrument in both the GNSS-only and GNSS+ISL estimation processes. It can be observed that the percentages are consistently around 93%. Although this value is lower than the typical percentage reported in the literature for other satellites like the Sentinels, which is approximately 99% (Montenbruck et al., 2018), this difference can be attributed to the orbital characteristics and number of GNSS passes. LEO satellites like the Sentinels have a higher number of GNSS passes per day, reducing the impact of not fixing one ambiguity on the overall percentage. In contrast, MEO satellites like the EHIs, with a lower number of passes, experience a more significant impact when an ambiguity is not fixed.

Satellite	Instrument	Percentage of fixed ambiguities	
		GNSS-only POD	GNSS+ISL POD
EHI-1	E1Q1	93.82%	Not applicable
	E1Q2	92.63%	Not applicable
EHI-2	E2Q1	93.20%	92.91%
	E2Q2	93.04%	93.02%

**Table 6.2:** Percentage of ambiguities successfully fixed for each instrument in the ideal GNSS-only and GNSS+ISL POD processes in the CLO scenario.

Lastly, it is worth mentioning that the aforementioned results remained consistent across both the MID and FAR scenarios. This outcome was anticipated since no errors were introduced into the model, indicating that any potential variations in the solution due to the baseline distance were not expected.

## Results: Individual Error Sources

This chapter delves into the investigation of various error sources and their impact on the estimation of the relative orbit between EHI-1 and EHI-2. The error sources include clock biases, thermal noise, instrumental delays, errors in the GNSS orbits and clocks, laser noise, uncertainties in the geopotential model, and uncertainties in the solar radiation pressure model. By isolating each error source, the study aims to unravel their specific influence on the relative orbit estimation, providing valuable insights into the underlying challenges associated with very precise baseline determination of high-dynamic baseline systems.

The presentation of the results primarily focuses on the examination of the CLO scenario. However, when deemed relevant, select findings from the MID and FAR scenarios will be included to provide a broader understanding of the error source effects. Additionally, in certain cases, the results of the GNSS+ISL estimation may not be explicitly showcased, as they manifest similarities with the GNSS-only results. It is also important to remark that for the GNSS+ISL analysis, only the fixed solution of the relative orbit will be presented, as explained in Section 5.4.2.

Furthermore, most of the errors introduced in this study, with the exception of the dynamical model errors, exhibit inherent randomness and are simulated using pseudo-random number generators. These generators require an input known as the seed for initialization. As a consequence, the generated random numbers are dependant on the specific seed value used. All the results presented in this chapter correspond to the use of a unique seed. Exploring multiple seeds would be highly time-consuming and has not been identified as necessary at this stage of the analysis.

In addition, it is important to note that when introducing each individual error source, the percentage of fixed ambiguities remains similar to the ideal scenario, with values of around 93%, except in the case of thermal noise. In the presence of thermal noise, there is a noticeable decrease in the percentage of fixed ambiguities.

### 7.1. Clock Biases

This section presents the results obtained when biases are introduced into the simulated clocks of both the GNSS and EHI satellites. Clock biases, generated based on the model described in 5.3.1, are incorporated into the simulations, allowing for an analysis of their impact on the precise orbit determination process. The introduced biases can range up to a few nanoseconds, mimicking realistic clock errors commonly encountered in satellite systems.

Figure 7.1a presents the three-dimensional position difference between the GNSS-only POD relative orbit and the reference relative orbit. Similarly, Figure 7.1b displays the comparison between the GNSS+ISL POD relative orbit and the reference relative orbit. These figures include the comparison of both the clock bias conditions and the ideal scenario without biases. It can be observed that the introduction of clock biases does not have a significant impact on the results, as the discrepancies with respect to the reference remain within the same order of magnitude as in the ideal problem.

In Figure 7.2, the comparison of the estimated receiver clock biases with respect to the generated receiver clock biases is illustrated. These results correspond to the GNSS-only fixed POD solution, although similar findings were observed for the other solutions as well. Notably, the differences between the estimated and reference biases are extremely small, on the order of numerical noise. This implies that the receiver clock offsets are accurately estimated during the POD process, and confirms that their impact on the estimated orbit solution is negligible when no other sources are introduced.

The same level of consistency between the ideal solution and the clock-biased solution was observed for the absolute orbits of EHI-1 and EHI-2. Moreover, although these results were obtained specifically for the CLO scenario, similar findings were also obtained for the MID and FAR scenarios.

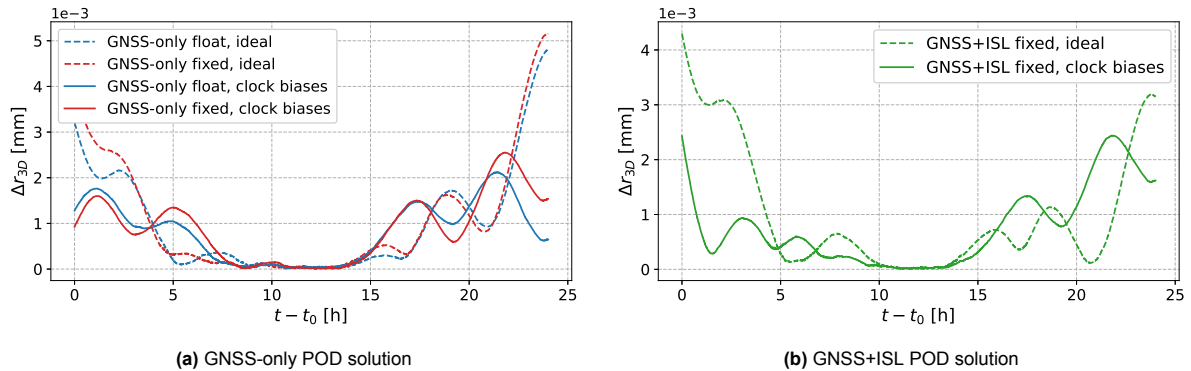


**Figure 7.1:** Comparison of the POD relative EHI-1/2 orbits with respect to the reference relative orbit in terms of the three-dimensional position difference. The figure illustrates the comparison under clock bias conditions and under ideal conditions. On the left, the GNSS-only POD results, and on the right, the GNSS+ISL POD results.

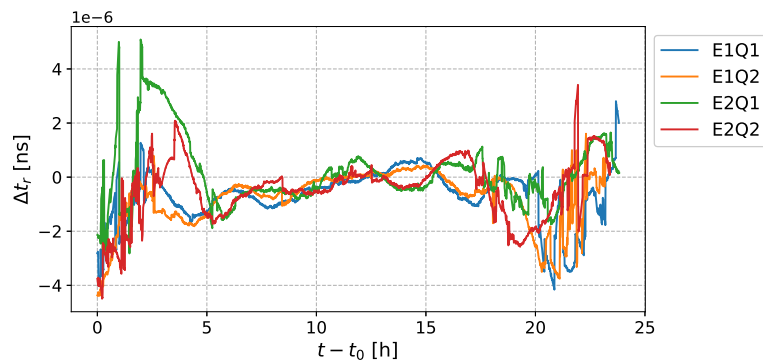


**Figure 7.2:** Comparison of the estimated receiver clock biases with respect to the reference clock biases, for the GNSS-only fixed POD solution in the CLO scenario.

## 7.2. Thermal Noise

The following section presents the results obtained when including only thermal noise in the GNSS observations. Thermal noise introduces errors in the pseudorange and carrier phase measurements. The magnitude of these errors varies depending on the signal-to-noise ratio of the observations. Observations taken at lower elevations, characterized by a lower SNR, present higher levels of thermal noise.

After careful analysis, it was noticed that observations associated with very low SNRs led to incorrect estimation of the satellite passes during the pre-processing of GNSS data. This issue arose due to the erroneous detection of cycle slips at the start and end of passes, where lower elevations and thus noisier observations were present. To mitigate this issue, a filtering mechanism based on SNR was implemented. In particular, a SNR threshold of 30 dB was established, ensuring the proper detection of passes. This value agrees with the thresholds employed by Guindal-Martinez (2020) and GMV (2022), providing consistency in the approach.

Figure 7.3a illustrates the comparison between the GNSS-only POD relative orbit and the reference relative orbit under the presence of thermal noise alone. The depicted results pertain to the CLO scenario. The fixed solution exhibits lower three-dimensional position errors compared to the float solution, thereby indicating that the introduction of ambiguity fixing yields an improved estimation of the relative orbit. The results of the GNSS+ISL POD displayed similar trends and outcomes.

Furthermore, Figures 7.3b and 7.3c present the same comparison as described earlier, but now for the MID and FAR scenarios, respectively. It can be observed that the achieved accuracy is slightly

worse in these scenarios for both the float and fixed solutions. This outcome aligns with expectations since, unlike the CLO scenario, the EHI-1 and EHI-2 satellites are farther apart in the MID and FAR scenarios. As a result, there is a lower number of GNSS satellites in common view, which diminishes the cancellation of the impact of thermal noise when computing the relative distance. The statistics of the orbit comparison of the fixed solution for the three scenarios are summarized in Table 7.1.

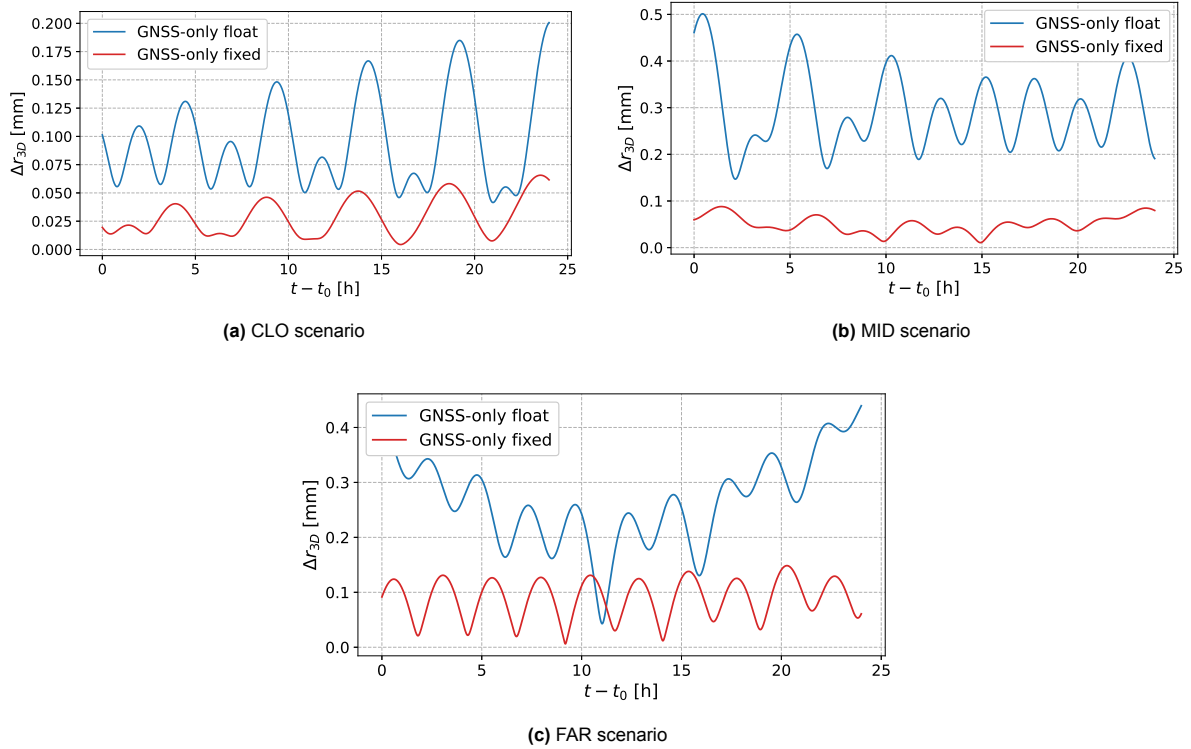


**Figure 7.3:** Comparison of the GNSS-only POD relative orbit with respect to the reference orbit, including only thermal noise for the three reference scenarios. The float and fixed solutions are shown in terms of the three-dimensional position difference.

Scenario	Stat.	3D [mm]
CLO	Mean	0.029
	RMS	0.033
	Max	0.066
MID	Mean	0.050
	RMS	0.053
	Max	0.088
FAR	Mean	0.090
	RMS	0.096
	Max	0.149

**Table 7.1:** Summary of the orbit comparison statistics for the GNSS-only fixed relative solution in the CLO, MID, and FAR scenarios, when introducing thermal noise. The statistics include the mean, RMS, and maximum of the 3D position error of the relative orbit.

It is important to mention that the percentage of fixed ambiguities when introducing thermal noise is lower than in the ideal scenario. Table 7.2 presents the percentage of fixed ambiguities for each instrument for both the GNSS-only and GNSS+ISL solutions when only thermal noise is included in the CLO scenario. Similar values were found for the MID and FAR scenarios. The results indicate that approxi-

mately 90% of the ambiguities are fixed when thermal noise is present, whereas in the ideal scenario, the percentage was 93%. This decrease in the percentage of fixed ambiguities might be attributed to the nature of thermal noise, which introduces a relatively large random error directly into the GNSS observations, making it more challenging to resolve the carrier phase ambiguities. However, despite this decrease, the fixed solutions still provide an improved estimation of the relative orbit compared to the float solutions, highlighting the benefits of ambiguity fixing in mitigating the impact of thermal noise.

Satellite	Instrument	Percentage of fixed ambiguities	
		GNSS-only POD	GNSS+ISL POD
EHI-1	E1Q1	90.27%	Not applicable
	E1Q2	89.87%	Not applicable
EHI-2	E2Q1	90.21%	89.93%
	E2Q2	90.10%	90.06%

**Table 7.2:** Percentage of ambiguities successfully fixed for each instrument in GNSS-only and GNSS+ISL POD processes in the CLO scenario, when only thermal noise is introduced.

### 7.3. Instrumental Delays

This section focuses on the influence of instrumental delays on the accuracy of the relative orbit. Interestingly, when only instrumental delays were introduced, it was observed that the fixed solutions performed worse than the float solutions, contrary to the expected outcome. This suggests that the ambiguity fixing algorithm may not be well-suited to handle constant biases in the observations. In order to address this issue and gain a deeper understanding of the influence of instrumental delays, the combined effect of thermal noise and instrumental delays on relative orbit accuracy is explored instead.

Figure 7.4 shows the comparison between the GNSS-only POD relative orbit and the reference relative orbit in the CLO scenario. The figure includes two cases: one where only thermal noise is introduced, and another where both thermal noise and instrumental delays are considered. Notably, the fixed solution demonstrates superior performance compared to the float solution. This finding remains valid for the GNSS+ISL POD estimation as well, and across the MID and FAR scenarios. Moreover, the percentage of fixed ambiguities remains the same as when only thermal noise is introduced for all scenarios.

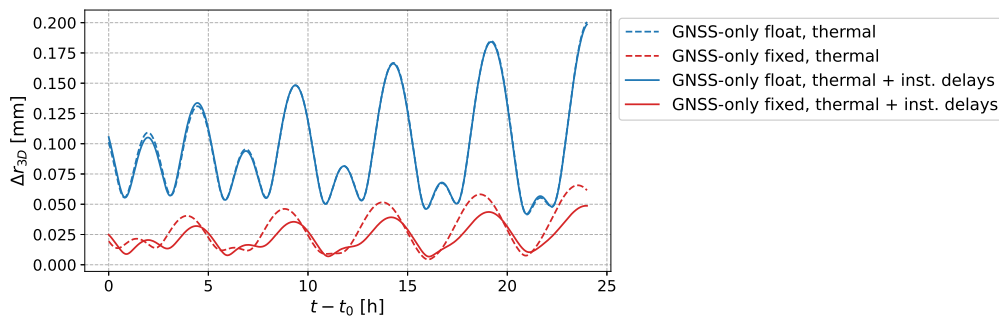


**Figure 7.4:** Comparison of the GNSS-only POD relative orbits with the reference relative orbit in the CLO scenario. The dashed lines represent the results when only thermal noise is introduced, while the solid lines represent the results when both thermal noise and instrumental delays are introduced. The comparison is done in terms of the 3D position difference.

Furthermore, it is noteworthy that the introduction of instrumental biases does not significantly impact the accuracy of the estimated orbit. However, this statement no longer holds true for the MID and FAR scenarios. In these particular scenarios, the inclusion of instrumental delays has a detrimental effect on the performance of the relative orbit estimation. The statistics of the relative orbit comparison, when introducing thermal noise and instrumental delays, are presented in Table 7.3. The 3D RMS of the fixed solution increases by 75% for the MID scenario and 37% for the FAR scenario, compared to the case where only thermal noise is considered and no instrumental delays are introduced. This degradation can be attributed to the reduced number of GNSS satellites in common view for EHI-1 and EHI-2 in these two scenarios.

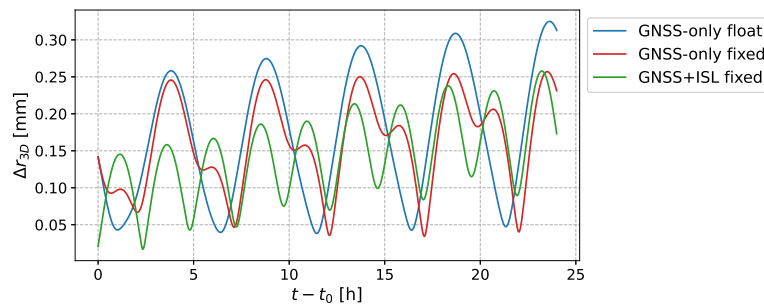
Scenario	Stat.	3D [mm]
CLO	Mean	0.023
	RMS	0.025
	Max	0.049
MID	Mean	0.088
	RMS	0.093
	Max	0.157
FAR	Mean	0.121
	RMS	0.132
	Max	0.201

**Table 7.3:** Summary of the orbit comparison statistics for the GNSS-only fixed relative solution in the CLO, MID, and FAR scenarios, when introducing thermal noise and instrumental delays. The statistics include the mean, RMS, and maximum of the 3D position error of the relative orbit.

## 7.4. Errors in the GNSS Orbits and Clocks

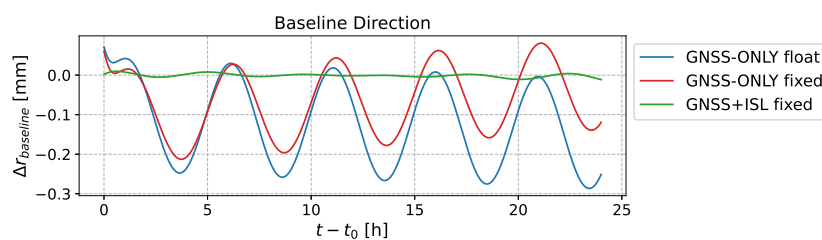
The errors in the GNSS orbits and clocks were simulated following the procedure outlined in Section 5.3.4. In particular, the simulated errors in the GNSS orbits are in the order of 2 cm, while clock errors are in the order of 70 ps. The subsequent analysis investigates the effect of these errors on the relative orbit estimation.

Figure 7.5 presents the comparison of the GNSS-only float, GNSS-only fixed, and GNSS+ISL fixed relative orbits with the reference relative orbit in the CLO scenario. The results indicate that the advantages of ambiguity fixing in this case are not as evident. Additionally, the inclusion of the ISL provides marginal improvements in the estimation of the 3D relative position.



**Figure 7.5:** Comparison of the GNSS-only float, GNSS-only fixed and GNSS+ISL fixed POD relative orbits with the reference relative orbit in the CLO scenario, when introducing errors in the GNSS orbits and clocks. The comparison is done in terms of the 3D position difference.

In Figure 7.6, when projecting the orbit comparison along the axes of the ISL-SGRA frame, it can be observed that the ISL contributes to an improved determination of the baseline in its own direction. Nonetheless, the results show that the other two directions are either similar or even deteriorated when compared to not using the ISL. This suggests that the ISL has a positive impact on the estimation of the baseline in the direction of the ISL observations, but its influence on the other directions is not clear.



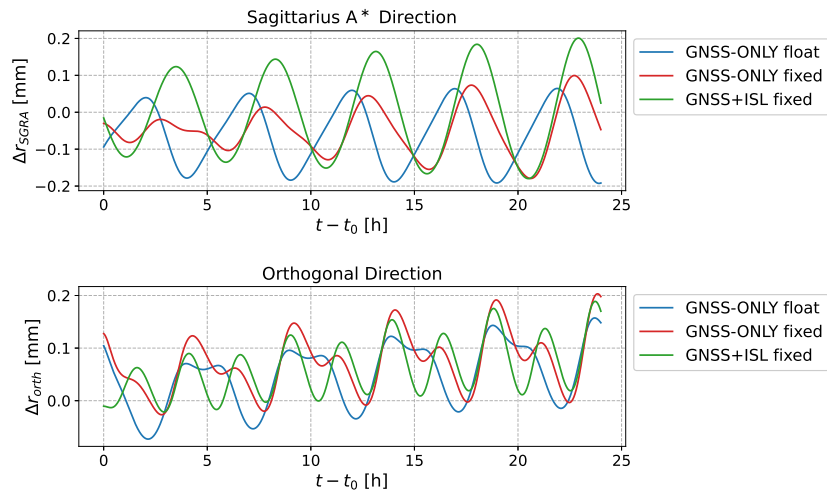


**Figure 7.6:** Comparison projected along the ISL-SGRA frame of the GNSS-only float, GNSS-only fixed and GNSS+ISL fixed POD relative orbits with the reference relative orbit in the CLO scenario, when introducing errors in the GNSS orbits and clocks.

Furthermore, Figure 7.7 shows the comparison of the GNSS-only fixed relative orbits against the reference relative orbit for the MID and FAR scenarios too. Similar results were obtained for the GNSS+ISL solution. According to Figure 7.7, the achieved accuracy of the relative orbit in the MID and FAR scenarios is lower, even if the estimation of the absolute orbits presents a similar level of accuracy across the three scenarios and does not show a clear pattern with intersatellite distance, as depicted in Figure 7.8. This can be explained by the fact that when taking the difference between the two orbits, the cancellation of common errors is more pronounced in the CLO scenario due to the larger number of GNSS satellites in common view.

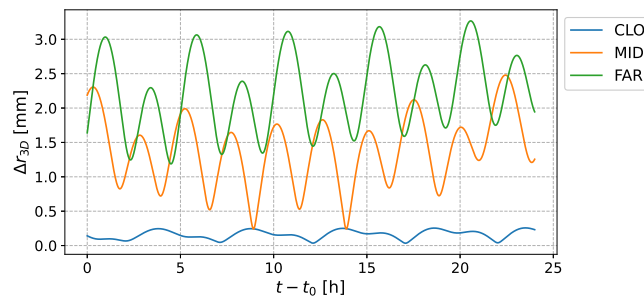


**Figure 7.7:** Comparison of the GNSS-only fixed POD relative orbit with the reference relative orbit in the CLO, MID, and FAR scenarios, when introducing errors in the GNSS orbits and clocks. The comparison is done in terms of the 3D position difference.

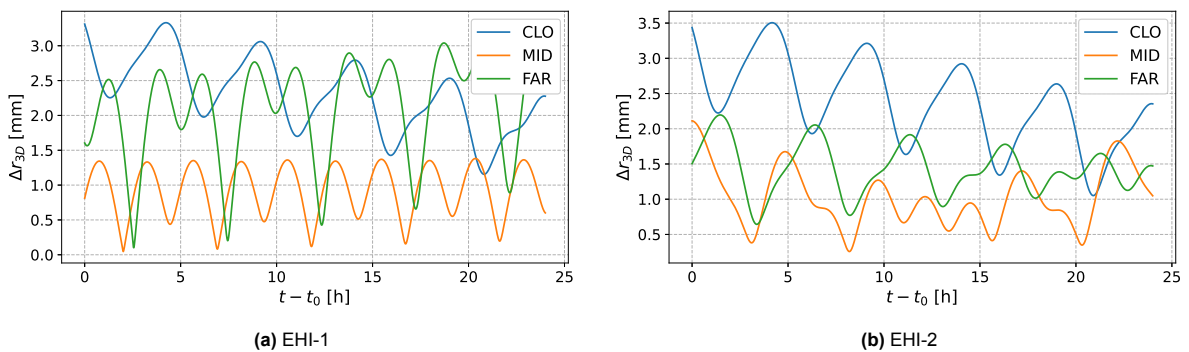


**Figure 7.8:** Comparison of the GNSS-only fixed POD orbits of EHI-1 and EHI-2 with the reference relative orbits in the CLO, MID, and FAR scenarios, when introducing errors in the GNSS orbits and clocks. The comparison is done in terms of the 3D position difference.

For a summary of the orbit comparison statistics, refer to Table 7.4. It is important to emphasize that the incorporation of errors in the GNSS ephemerides and clocks has a higher impact on the relative orbit accuracy compared to the inclusion of thermal noise. In fact, the former results in a three-dimensional position error that is approximately one order of magnitude larger.

Scenario	Stat.	3D [mm]
CLO	Mean	0.16
	RMS	0.17
	Max	0.26
MID	Mean	1.39
	RMS	1.48
	Max	2.48
FAR	Mean	2.23
	RMS	2.29
	Max	3.27

**Table 7.4:** Summary of the orbit comparison statistics for the GNSS-only fixed relative solution in the CLO, MID, and FAR scenarios, when introducing errors in the GNSS orbits and clocks. The statistics include the mean, RMS, and maximum of the 3D position error of the relative orbit.

## 7.5. Laser Noise

The impact of adding noise to the laser observations is explored in this section. Gaussian noise with a standard deviation of  $\sigma = 1$  mm is introduced into the ISL observables. The chosen noise value represents the most pessimistic estimate found in the literature. Figure 7.9 shows the comparison between the GNSS+ISL fixed relative orbit and the reference relative orbit for the CLO scenario. The figure showcases the ideal case, where no noise is added, and the case where a 1 mm Gaussian laser noise is introduced. It can be observed that, despite the presence of noise, the least-squares algorithm is able to accurately estimate the relative orbit as if no noise were present. The results were similar for the MID and FAR scenarios.

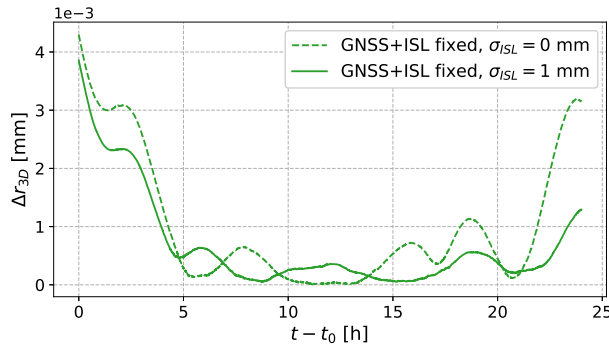


**Figure 7.9:** Comparison between the GNSS+ISL fixed POD relative orbit and the reference relative orbit for the CLO scenario. The dashed line represents the ideal case with no noise, while the solid line represents the results with 1 mm white laser noise introduced. The comparison is done in terms of the 3D position difference.

## 7.6. Uncertainties in the Geopotential Model

The effect of introducing uncertainties in the geopotential model is described in this section. These uncertainties are introduced by using one geopotential model in the generation of the reference orbits and observations, and another geopotential model in the estimation process. Two scenarios are examined: one focused on the year 2017, when the geopotential models exhibit relatively similar characteristics, and another focused on the year 2022, when the geopotential models differ more significantly.

Starting with the worst-case scenario of 2022, the comparisons between the GNSS-only fixed POD absolute and relative orbits with respect to the reference orbits for the CLO, MID, and FAR scenarios

are presented in Figures 7.10a, 7.10b, and 7.10c. The GNSS-only float and GNSS+ISL fixed solutions are not shown as they have a similar behaviour.

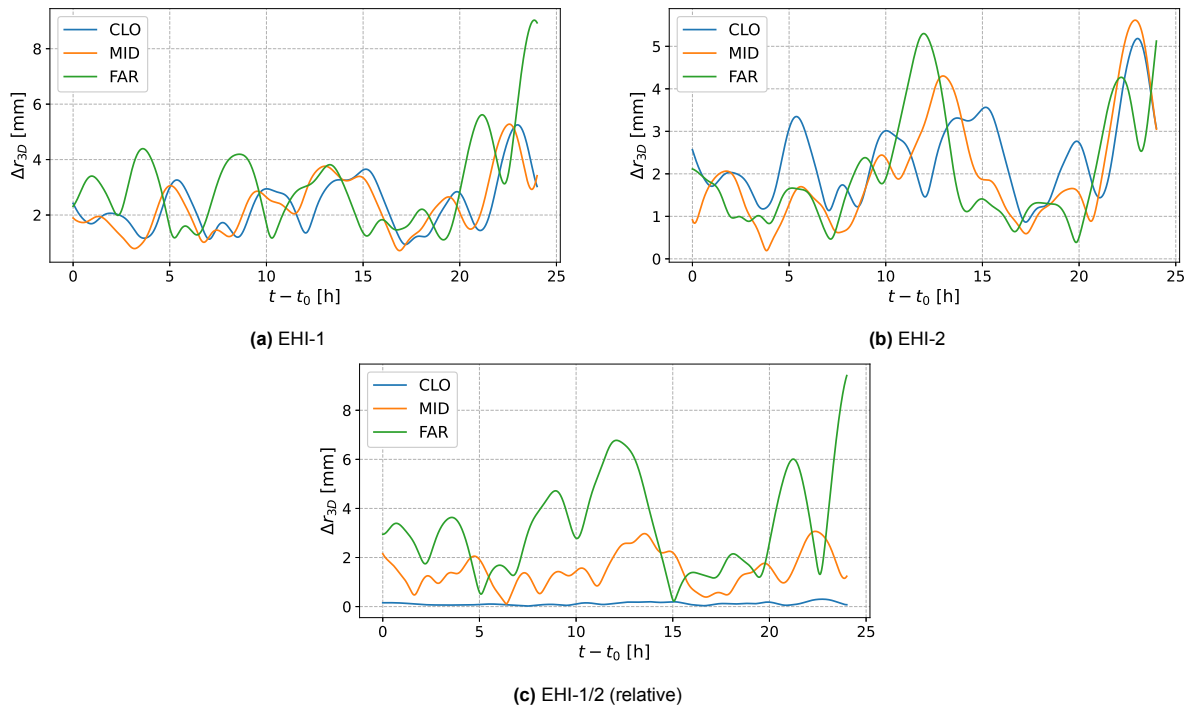


**Figure 7.10:** Comparison of the GNSS-only fixed POD absolute and relative orbits with respect to the reference orbits for the CLO, MID, and FAR scenarios, using a different geopotential model in 2022.

Figures 7.10a and 7.10b reveal that the use of a different geopotential model has a comparable impact on the orbit estimation of EHI-1 and EHI-2 across all three scenarios, resulting in an accuracy of a few millimetres in terms of 3D position. However, Figure 7.10c demonstrates that the accuracy of the relative orbit estimation is influenced by the baseline distance. When EHI-1 and EHI-2 are in close proximity, they encounter similar geopotential effects, causing the errors induced by the incorrect geopotential model to cancel out during the computation of the relative orbit. Conversely, as the satellites drift apart, the cancellation effect diminishes since they are no longer affected by the same geopotential errors.

The statistical outcomes of the relative orbit comparison are summarized in Table 7.5. The 3D errors in the estimated orbits resulting from uncertainties in the geopotential demonstrate a similar order of magnitude to the errors caused by uncertainties in the GNSS orbits and clocks. However, it should be noted that the former errors tend to be slightly worse for larger baselines.

Scenario	Stat.	3D [mm]
CLO	Mean	0.12
	RMS	0.13
	Max	0.30
MID	Mean	1.47
	RMS	1.63
	Max	3.07
FAR	Mean	3.20
	RMS	3.70
	Max	9.41

**Table 7.5:** Summary of orbit comparison statistics for the GNSS-only fixed relative solution in the CLO, MID, and FAR scenarios, when introducing errors in the geopotential model. The statistics include the mean, RMS, and maximum of the 3D relative error.

In the 2017 scenario, as expected, the accuracy of the estimated relative orbit is better. In the CLO scenario, the RMS of the 3D relative position error is 50% lower compared to that found for the 2022 case. However, in the MID and FAR scenarios, this reduction in RMS is only 10%. Therefore, even though the geopotential uncertainty is not as pronounced, the introduced 3D relative errors for the larger baselines still remain at the millimetre level.

## 7.7. Uncertainties in the Solar Radiation Pressure Model

The impact of introducing uncertainties in the solar radiation pressure (SRP) model is investigated in this section. In this analysis, two different SRP models are employed: one for generating the reference orbits and observations, and another for the estimation process. Specifically, a bow-wing model is used in the simulation phase, while an empirical ECOM model is applied during the estimation.

A noteworthy observation in this analysis is that when using a 24-hour arc for estimation, the solution exhibits significant degradation at the beginning and end of the interval. To solve this issue, the orbit determination interval was extended by 5 hours at the beginning and 5 hours at the end, resulting in a total increment of 10 hours. Consequently, 34-hour arc intervals were employed, but only the 24-hour centred solution was considered for further analysis. This choice of 5-hour extensions aligns with the orbital period, which is approximately 5 hours.

The next step is to assess whether the proposed modified ECOM model — that is, ECOM-SGRA — outperforms the standard ECOM model in accurately capturing the impact of solar radiation pressure on the EHI satellites. Moreover, it is crucial to investigate the potential benefits of optimizing the model by tuning the number of estimated parameters and selecting appropriate time intervals.

Figure 7.11a displays the comparison between the GNSS-only fixed relative orbit and the reference relative orbit for various sub-intervals (1, 3, 5, and 7) when utilizing the standard ECOM model in the estimation process. On the other hand, Figure 7.11b presents the same comparison, but employing the ECOM-SGRA model.

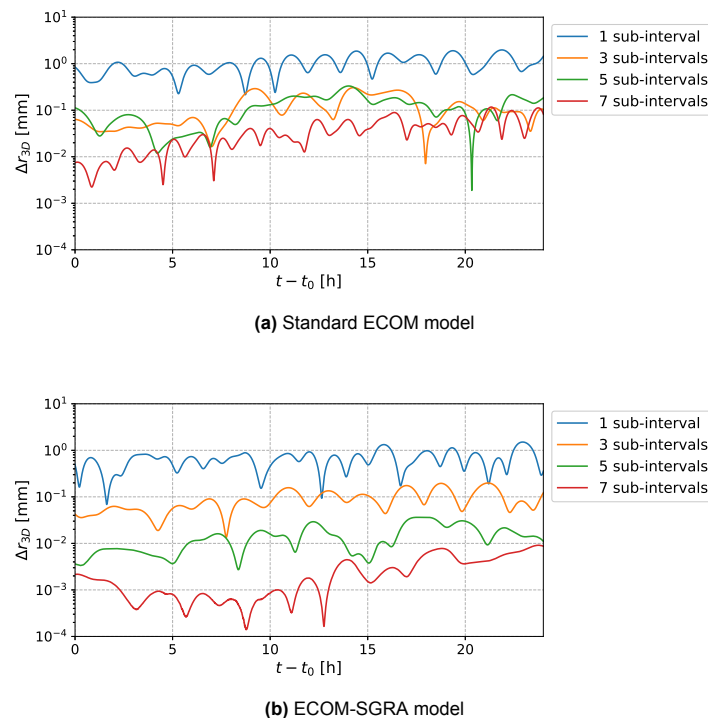


**Figure 7.11:** Comparison between the GNSS-only fixed POD relative orbit and the reference relative orbit for different sub-intervals for the CLO scenario, when using a different SRP model. On the top, the standard ECOM model is used in estimation, while on the bottom the ECOM-SGRA model is employed. The comparison is done in terms of the 3D position difference.

Although both ECOM models exhibit relatively small 3D relative position errors, the ECOM-SGRA model outperforms the standard ECOM model, particularly when employing 5 and 7 sub-intervals. Using the ECOM-SGRA model with 7 sub-intervals yields accuracies that are relatively close to the error-

free scenario. This can be explained by the fact that dividing the 34-hour arc into 7 sub-intervals results in approximately 4.85-hour sub-intervals, which aligns with the orbital period of about 4.9 h. These results pertain to the CLO scenario and are consistent across the GNSS-only float and GNSS+ISL fixed solutions.

The preference for the ECOM-SGRA model over the standard ECOM model can also be justified by examining the estimation of the SRP empirical coefficients. Figure 7.12 presents the estimated  $D$ ,  $Y$ , and  $B$  coefficients for EHI-1 using both ECOM and ECOM-SGRA models. The  $D$  direction represents the satellite-Sun direction and remains the same for both ECOM models, while the  $Y$  and  $B$  directions differ between the two models. The results shown are specific to the GNSS-only fixed solution in the CLO scenario, employing 7 sub-intervals. Similar findings were observed for EHI-2.

In Figure 7.12, it can be observed that  $D_0$  is the largest among the estimated coefficients. This is due to the fact that the majority of the solar radiation pressure acts in this direction. The  $D_0$  coefficient is negative, as the  $D$  axis points opposite to the acceleration caused by solar radiation, and it manifests an increasing trend. The cosine and sine coefficients, denoted as  $D_c$  and  $D_s$ , respectively, are three orders of magnitude lower than  $D_0$ . Both ECOM models provide nearly identical estimates for  $D_0$  as well as similar magnitudes for  $D_c$  and  $D_s$ .

On the other hand, the  $Y$  and  $B$  coefficients present a different behaviour for each model. In the standard ECOM model, the constant coefficients  $Y_0$  and  $B_0$  are two orders of magnitude lower than the cosine and sine terms. Moreover, the sinusoidal terms exhibit an increasing trend. In contrast, the ECOM-SGRA model shows the opposite behaviour. The constant terms are greater than the sinusoidal terms and follow an increasing trend. The behaviour of the ECOM-SGRA model is more reasonable as it allows the constant terms to absorb the majority of the solar radiation pressure.

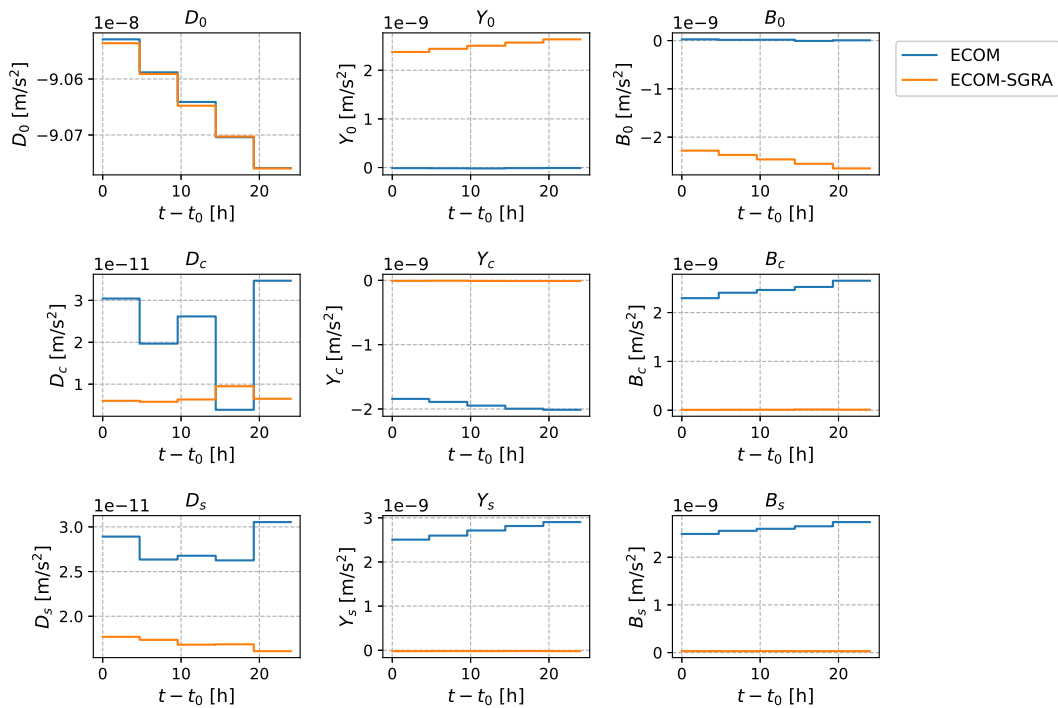


**Figure 7.12:** Estimated empirical coefficients for EHI-1 using a 7 sub-interval arc, comparing the standard ECOM and ECOM-SGRA models. The results correspond to the GNSS-only fixed solution in the CLO scenario.

It is worth noting that an attempt was made to perform the orbit estimation using only the constant ECOM-SGRA coefficients, given their significantly larger magnitude compared to the sinusoidal terms. However, the results proved to be significantly poorer, indicating the necessity of including all nine coefficients in the POD process.

Similarly to the geopotential errors, the MID and FAR scenarios demonstrate lower accuracy in the relative orbit determination compared to the CLO scenario, despite having similar errors in the absolute orbits. This can be attributed to the same underlying reason as explained for the geopotential. When

EHI-1 and EHI-2 are close, they experience a similar solar radiation pressure, leading to the cancellation of errors caused by the inaccurate SRP model during the computation of the relative orbit. However, as the satellites move away from each other, their orientations with respect to the Sun become less similar, resulting in differences in the SRP errors that do not cancel out when computing the relative distance. The results of the relative orbit comparison for all three scenarios can be seen in Figure 7.13 and Table 7.6.

From the results, it can be observed that the remaining SRP modeling errors, when using the ECOM-SGRA model to estimate a box-wing SRP effect, lead to sub-millimetre level 3D relative position errors. These errors are comparable in magnitude to those caused by thermal noise and approximately one order of magnitude smaller than the errors resulting from geopotential uncertainties and uncertainties in the GNSS products. Nonetheless, it remains uncertain whether the use of the ECOM-SGRA model will introduce additional challenges when all error sources are combined.

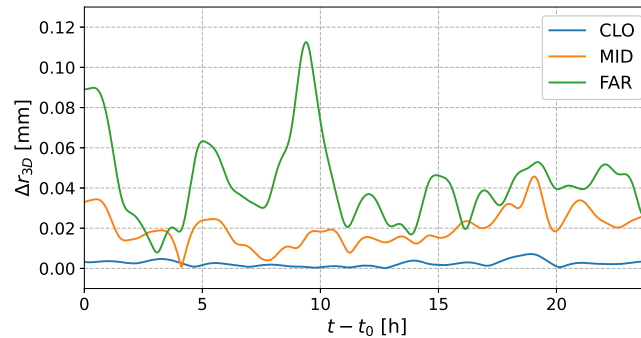


**Figure 7.13:** Comparison of the GNSS-only fixed POD relative orbit with the reference relative orbit for the CLO, MID, and FAR scenarios, when estimating the SRP with a different model than the reference one. The ECOM-SGRA model with 7 sub-intervals is employed in the orbit determination. The comparison is done in terms of the 3D position difference.

Scenario	Stat.	3D [mm]
CLO	Mean	0.003
	RMS	0.004
	Max	0.012
MID	Mean	0.023
	RMS	0.027
	Max	0.136
FAR	Mean	0.045
	RMS	0.055
	Max	0.306

**Table 7.6:** Summary of the orbit comparison statistics for the GNSS-only fixed relative solution in the CLO, MID, and FAR scenarios, when introducing errors in the SRP model. The statistics include the mean, RMS, and maximum of the 3D position error of the relative orbit.

## 7.8. Summary of Impact of Individual Error Sources

In summary, the dominant error sources identified are errors in the geopotential and errors in the GNSS orbits and clocks, resulting in millimetre level 3D relative position errors for large baselines. Following them, thermal noise and errors in the solar radiation pressure model lead to sub-millimetre level 3D relative position errors for large baselines. Additionally, instrumental delays do not have an impact for small baselines, but introduce sub-millimetre errors for longer baselines. The impact of all the previous errors on relative orbit accuracy is magnified for larger baselines due to reduced error sharing between the two satellites. Lastly, clock biases and laser noise have a negligible effect on the relative orbit accuracy.

The analysis of individual error sources has highlighted the potential of ambiguity fixing to enhance orbit determination. The process of integer ambiguity resolution primarily aids in mitigating thermal noise and instrumental delays, while its effectiveness in mitigating other error sources is limited. When it comes to the ISL, its contribution is found to be limited to the baseline direction, while not significantly improving the estimation of the relative distance in the other directions. Nevertheless, it is crucial to acknowledge that this analysis is specifically centred on individual error sources, and thus further investigation is needed combining all errors simultaneously.

# Results: Combined Error Sources

Building upon the knowledge gained from the exploration of individual error sources in the previous chapter, the current chapter aims to understand the cumulative effect of these errors on the estimation of the relative orbit between EHI-1 and EHI-2. By considering a combination of errors in the observations, the GNSS products, and the dynamical model, this investigation seeks to emulate a more realistic scenario.

To thoroughly evaluate the impact of the combined error sources on the estimation of the relative orbit, the analysis in this chapter covers the entire month of April 2022. This extended time frame was chosen because the relationship between baseline and relative orbit accuracy is not straightforward, especially as the satellites move further apart. By considering a longer duration of observations, it is possible to obtain an even better understanding of how the baseline distance influences the results.

It is worth noting that, as mentioned in Chapter 7, the majority of the errors introduced exhibit randomness and require the use of pseudo-random number generators for their simulation. All the results presented in this chapter correspond to the use of a unique seed to initialize the pseudo-random number generator. However, Section 8.4 will explore the use of multiple seeds to generate the results and extract statistics from them. The goal of this analysis is to investigate if the same conclusions hold when different values of the random variables are employed, thus verifying the robustness and generalizability of the findings.

The chapter begins by providing a list of all the considered error sources. Afterwards, the analysis delves into determining the optimal type and quantity of estimated parameters needed for the POD, along with the results of the orbit determination for EHI-1 and EHI-2 satellites. The chapter proceeds with the presentation of the relative orbit estimation results for a single seed, followed by an assessment of the variability of the results through the use of multiple seeds. The chapter also investigates the sensitivity of the estimation to errors in the GNSS orbits and clocks, as well as to uncertainties in the dynamical model, which have been identified as the two dominant error sources impacting the accuracy of the relative orbit determination process.

## 8.1. List of Error Sources

The following errors are considered in the analysis of this chapter:

- Biases in both the GNSS clocks and EHI clocks, simulated with the nominal clock parameter values presented in Table 5.4.
- Thermal noise in the GNSS observations, simulated using the antenna gain patterns presented in Section 5.3.2 and assuming zero hardware losses.
- Instrumental delays in both the GNSS and EHI instruments, simulated using the methodology described in Section 5.2.1.2 and perturbed according to the methodology discussed in Section 5.3.3.
- Errors in the GNSS orbits and clocks, with the nominal values presented in Table 5.9.
- Gaussian noise in the ISL observations, with a standard deviation of 1 mm.
- Uncertainties in the geopotential model, simulated by employing a different model for generating the observations and for estimation, as explained in Section 5.3.6. The worst-case scenario of 2022 is selected.
- Uncertainties in the solar radiation pressure model, simulated by using a different model for generating the observations and for estimation, as discussed in Section 5.3.7. In particular, the ECOM-SGRA model is employed in the estimation.

## 8.2. Results of Absolute Orbit Estimation

Prior to presenting the estimation results of the orbits of satellites EHI-1 and EHI-2, an analysis is conducted to examine the empirical accelerations introduced in the POD process. Next, the results of the POD are illustrated, demonstrating the accuracy achieved in estimating the absolute orbits.

### 8.2.1. Analysis of Empirical Accelerations

In the context of this problem, two specific approaches are explored for incorporating empirical accelerations into the dynamical model. The first method consists of using Cycle-Per-Revolution (CPR) accelerations, which are introduced in both the along-track and cross-track directions. The second approach involves the introduction of ECOM-SGRA accelerations, which are specifically defined within the ECOM-SGRA frame. To optimize the absorption of dynamical errors, it is necessary to carefully analyze how to combine these accelerations and determine which ones should be incorporated, as well as the optimal quantity to be introduced. Additionally, the application of constraints for these empirical accelerations should be explored.

After evaluating the options, it was determined that estimating both the ECOM-SGRA coefficients and the CPRs did not yield any advantages and only resulted in increased computational time, even when constraints were applied to the CPR coefficients. Therefore, the optimal configuration was identified to be the estimation of only the 9 ECOM-SGRA coefficients without incorporating any CPRs. This approach allowed the ECOM-SGRA coefficients to effectively absorb the errors typically handled by CPRs, such as those arising from the geopotential. The constant ECOM-SGRA coefficients were constrained with a standard deviation of  $10^{-6}$  m/s<sup>2</sup>, while the sinusoidal ECOM-SGRA coefficients were constrained with a standard deviation of  $10^{-9}$  m/s<sup>2</sup>.

The optimal setup involved using 34-hour estimation arcs with 7 sub-intervals. Further increasing the number of sub-intervals did not provide a significant improvement of the results but rather increased computational time. These findings align with those presented in Section 7.7, where only uncertainties in the SRP model were considered.

Figure 8.1 provides an overview of the estimated ECOM-SGRA coefficients for EHI-1 throughout the entire month of April, specifically for the GNSS-only fixed solution. Similar coefficient patterns were observed for EHI-2. The observed behaviour is consistent with the case when only uncertainties in the SRP model were introduced, as shown in Figure 7.12. However, the coefficients are now higher because they also absorb other error sources, such as errors in the geopotential model.

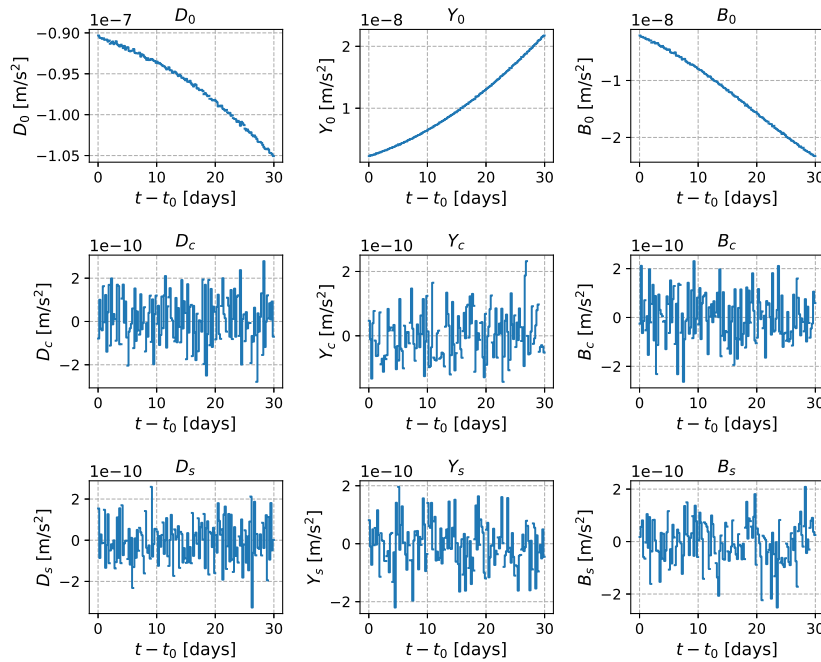


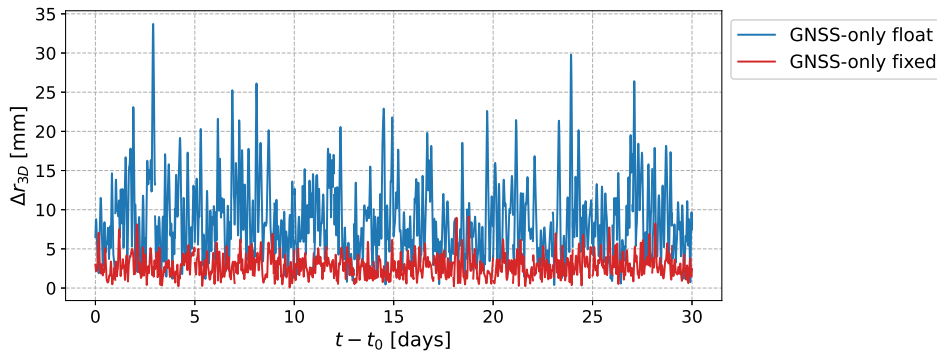
**Figure 8.1:** Evolution of the ECOM-SGRA coefficients for EHI-1 throughout April, corresponding to the GNSS-only fixed solution and including all error sources. The coefficients are estimated using 34-hour arcs with 7 sub-intervals per arc.

### 8.2.2. Analysis of Absolute Orbit Accuracy

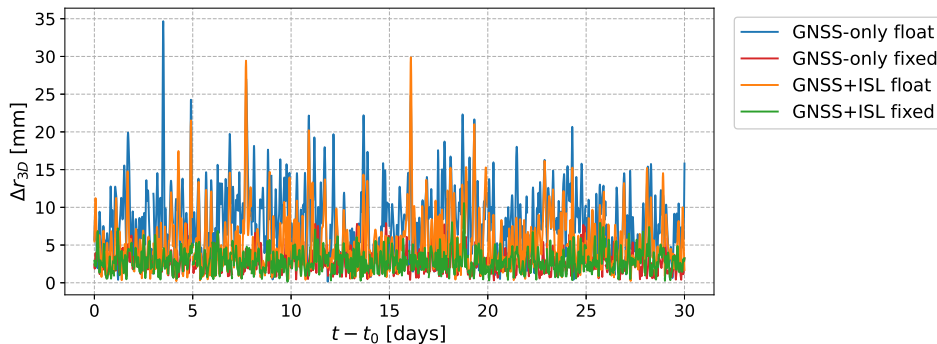
In this section, the results of the estimated absolute orbits of EHI-1 and EHI-2 are presented for the entire month of April 2022. In Figure 8.2, the results for the EHI-1 satellite are depicted, showing both the GNSS-only float and fixed solutions. This figure demonstrates that the fixed solution outperforms the float solution, consistently maintaining position errors below 10 mm throughout the entire month. The fixed solution exhibits a 3D position error with a mean of 2.88 mm and a RMS of 3.18 mm. On the other hand, the float solution shows a mean 3D position error of 8.87 mm and a RMS of 10.07 mm.

Figure 8.3 shows the corresponding results for the EHI-2 satellite. The figure presents the GNSS-only float and fixed solutions, as well as the GNSS+ISL float and fixed solutions. Similar to EHI-1, the fixed solutions exhibit better accuracy than the float solutions. However, in terms of the use of the ISL, there is no clear advantage observed, as both fixed solutions present similar performance. The 3D position error of the GNSS-only fixed solution demonstrates a mean of 2.95 mm and a RMS of 3.29 mm, while the GNSS+ISL fixed solution exhibits the same mean and practically the same RMS at 3.26 mm.

Throughout the entire month of April, it is worth noting that the percentage of fixed ambiguities remains similar to when only thermal noise is introduced. Thus, approximately 90% of the ambiguities are successfully resolved for both the GNSS-only and GNSS+ISL solutions.



**Figure 8.2:** Comparison of the estimated absolute orbit with the reference absolute orbit of EHI-1 for the whole month of April, considering the incorporation of all error sources. Results are shown for the GNSS-only float and GNSS-only fixed solutions in terms of the 3D position difference.



**Figure 8.3:** Comparison of the estimated absolute orbit with the reference absolute orbit of EHI-2 for the whole month of April, considering the incorporation of all error sources. Results are shown for the GNSS-only float, GNSS-only fixed, GNSS+ISL float, and GNSS+ISL fixed solutions in terms of the 3D position difference.

Based on this analysis of the absolute orbits, it is demonstrated that the fixed solutions consistently outperform the float solutions. This emphasizes the importance of integer ambiguity resolution for achieving highly accurate results. Also, when considering the absolute orbit estimation of EHI-2, the use of the ISL does not appear to contribute significantly in terms of total position error.

### 8.3. Results of Relative Orbit Estimation

The primary objective of this section is to present the outcomes obtained from the estimation of the relative orbit throughout the entire month of April 2022, considering the incorporation of all the previously listed error sources. By introducing these errors simultaneously, a more realistic assessment of the baseline determination accuracy can be achieved.

#### 8.3.1. Analysis of Relative Orbit Accuracy

In Figure 8.4, the results of the relative orbit estimation for the entire month of April are presented, comparing the estimated relative orbit with the reference relative orbit. The figure displays the results obtained from three different estimation scenarios: GNSS-only float, GNSS-only fixed, and GNSS+ISL fixed. The evaluation is based on the three-dimensional position error.

Analyzing Figure 8.4, it can be seen that the fixed solutions display a notably superior performance compared to the float solution, highlighting the importance of integer ambiguity resolution in this particular problem. Within the fixed solutions, the GNSS+ISL POD does not appear to yield a significant improvement in terms of 3D relative position accuracy when compared to the GNSS-only POD. These findings suggest that, at least for the considered accuracy metric, the inclusion of the ISL observations does not provide a substantial advantage over a GNSS-only estimation.

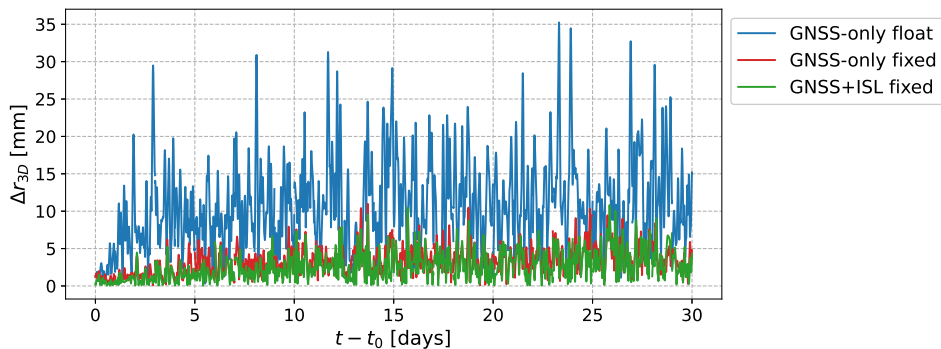


**Figure 8.4:** Comparison of the estimated relative orbit with the reference relative orbit for the whole month of April, considering the incorporation of all error sources. Results are shown for GNSS-only float, GNSS-only fixed, and GNSS+ISL fixed solutions in terms of the 3D position difference.

To gain further insights into the impact of the ISL observations, it is beneficial to project the previous comparison onto the ISL-SGRA frame. Figure 8.5 provides a visual representation of this projection, showcasing the comparison in the three directions of the ISL-SGRA frame for all three solutions. In addition, Figure 8.6 focuses specifically on the fixed solutions, offering a closer examination of the relative orbit comparison within the ISL-SGRA frame.

In Figure 8.5, it can be observed that the fixed solutions consistently demonstrate superior accuracy compared to the float solution across all three directions. Regarding the influence of the ISL, its utilization greatly enhances the determination of the baseline in its own direction. However, for the other two directions, the ISL does not introduce significant improvements in the determination of the relative distance. Focusing on the Sagittarius A\* direction, which holds particular importance for processing the VLBI observations in this project, it is notable that both the GNSS-only fixed and GNSS+ISL fixed solutions maintain errors within the range of -10 mm to 10 mm.

Table 8.1 provides a quantitative summary of the statistics of the comparisons, highlighting the RMS in the direction of Sagittarius A\*. The results indicate that, in this direction, the RMS and maximum relative position error are slightly lower for the GNSS+ISL fixed solution compared to the GNSS-only fixed solution. However, the mean values show the opposite trend. Hence, the impact of the ISL in the direction of the black hole is not clear. It is worth noting that although not directly relevant to this mission, the extremely precise ISL observations enable the achievement of extraordinary sub-millimetre level accuracy in the baseline projection.

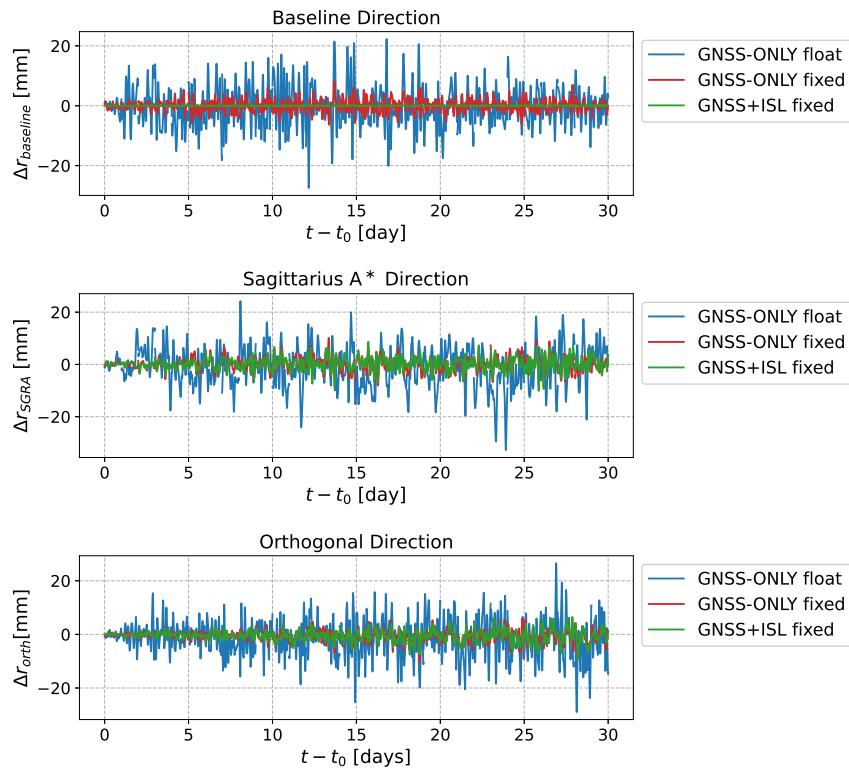


**Figure 8.5:** Comparison of the estimated relative orbit with the reference relative orbit projected in the ISL-SGRA frame for all solutions for the whole month of April, considering the incorporation of all error sources.

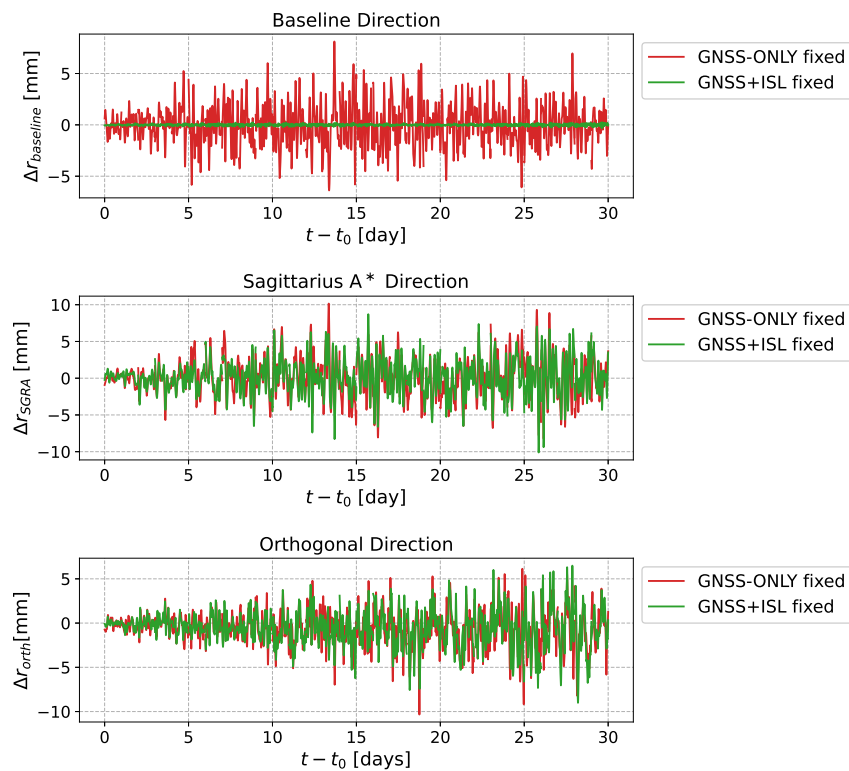


**Figure 8.6:** Comparison of the estimated relative orbit with the reference relative orbit projected in the ISL-SGRA frame for the fixed solutions for the whole month of April, considering the incorporation of all error sources.

Solution	Stat.	Baseline [mm]	Sgr A* [mm]	Ortho. [mm]	3D [mm]
GNSS-only float	Mean	-0.42	-0.88	-1.42	10.93
	RMS	6.57	7.43	6.83	12.39
	Max	22.27	24.21	26.54	35.25
GNSS-only fixed	Mean	-0.01	0.05	-0.63	3.44
	RMS	1.99	2.59	2.13	3.91
	Max	8.12	10.15	6.14	10.98
GNSS+ISL fixed	Mean	-0.004	0.12	-0.56	2.76
	RMS	0.076	2.38	2.08	3.33
	Max	0.250	8.71	6.49	10.81

**Table 8.1:** Summary of the comparison results between estimated relative orbit and reference relative orbit for different solutions, considering the incorporation of all error sources throughout the entire month of April 2022. The RMS in the direction of Sagittarius A\* is highlighted in red.

In addition to the previously discussed observations, it is notable that the relative orbit error tends to increase as the distance between the satellites grows. Nevertheless, an interesting finding is that a larger baseline does not necessarily result in a larger error. There are instances where earlier days exhibit poorer performance compared to later days, despite the latter having larger baselines. The evolution of the baseline distance can be visualized in Figure 6.1 of Chapter 6.

This behaviour can be attributed to the varying influence of SRP and geopotential acceleration as the satellites separate. As the distance between the satellites increases, they experience different SRP and geopotential errors, leading to an increase in the estimation error when computing the relative orbit since the errors are more dissimilar. However, the relationship between baseline length and dynamical errors is not solely determined by the baseline size. Instead, it depends on how the dynamical model has been perturbed and whether both satellites experience a similar dynamical error on a given day. Thus, the error behaviour is influenced by the specific dynamical perturbations affecting the satellites at a particular moment.

Furthermore, as the satellites drift apart, they also have fewer GNSS satellites in common view. Nonetheless, this relationship is not strictly linear, where a longer baseline results in fewer shared GNSS satellites. Figure 8.7 illustrates this behaviour by presenting the average number of GNSS satellites in common view per day, considering both GPS and Galileo. Interestingly, the worst-case scenario does not correspond to the latter days of the month but rather occurs during the middle days. When there are more GNSS satellites in common view, the errors associated with these shared satellites, such as errors in their orbits, tend to partially cancel each other out during the computation of the relative orbit. This cancellation effect contributes to improved accuracy in the relative orbit estimation.

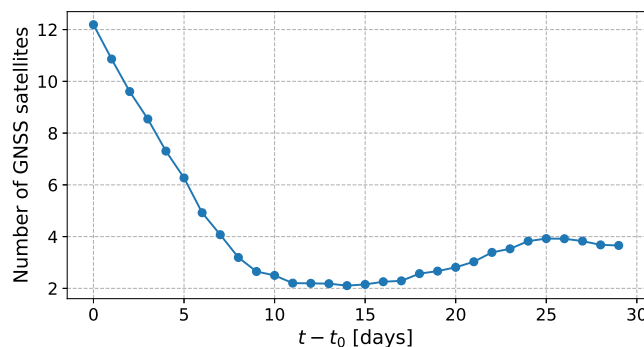


**Figure 8.7:** Mean number of GNSS satellites in common view per day for the whole month of April.

### 8.3.2. Achievement of Accuracy Requirement

The scientific requirements of the mission place particular emphasis on assessing the percentage of observations that meet a specific threshold for relative orbit accuracy. Specifically, the mission requires a 1-dimensional relative position accuracy of 3.5 mm (3-sigma), meaning that 99.7% of the measurements should fall within this accuracy threshold. This is of particular importance in the direction of Sagittarius A\*, as achieving high-quality images of the black hole relies on meeting this requirement. To evaluate the fulfillment of this requirement, it is valuable to examine the percentiles of the relative position errors.

Figure 8.8a displays the percentiles for the GNSS-only fixed solution, while Figure 8.8b presents the corresponding results for the GNSS+ISL fixed solution. To further analyze the performance, Table 8.2 provides the percentiles 68% (1-sigma), 99.5% (2-sigma), and 99.7% (3-sigma) for both solutions.

Figure 8.8 and Table 8.2 demonstrate that the ISL mainly helps improve relative orbit accuracy in the baseline direction. The GNSS+ISL fixed solution meets the required accuracy in this direction. However, in the other two directions, the required accuracy is not achieved even with the use of the ISL. In particular, the 3-sigma value in the direction of Sagittarius A\* is 8.29 mm for the GNSS+ISL fixed solution, which does not meet the required 3.5 mm objective.

Additionally, an interesting percentile to consider is the one associated with the 3.5 mm accuracy requirement in the direction of Sagittarius A\*. For the GNSS-only fixed solution, this percentile is 82.7%, whereas for the GNSS+ISL fixed solution, it increases to 86.3%. This indicates that a slightly larger portion of the observations meets the 3.5 mm requirement in the ISL-enhanced solution.

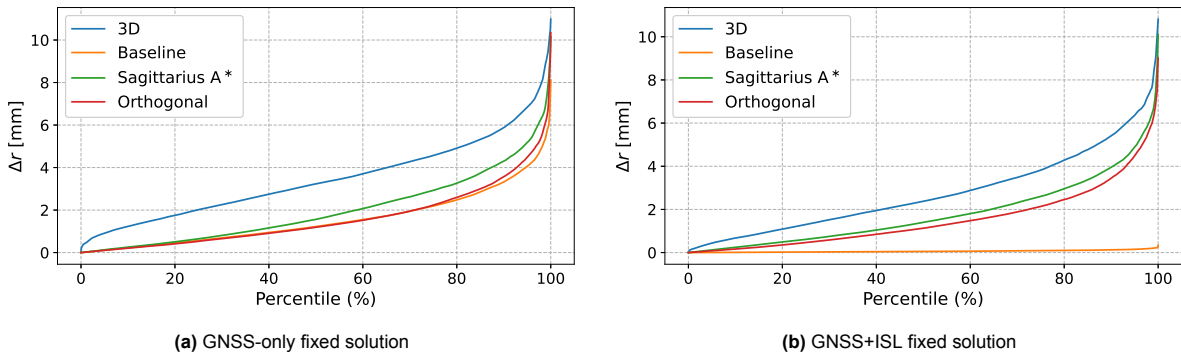


**Figure 8.8:** Percentiles of the relative position errors for the GNSS-only fixed and GNSS+ISL fixed solutions, considering the incorporation of all error sources throughout the entire month of April 2022. The 3D error as well as the error projected in the ISL-SGRA frame in each direction are represented.

Percentile	Solution	Baseline [mm]	Sgr A* [mm]	Ortho. [mm]	3D [mm]
68% ( $1\sigma$ )	GNSS-only fixed	1.85	2.52	1.85	4.16
	GNSS+ISL fixed	0.08	2.19	1.79	3.37
95% ( $2\sigma$ )	GNSS-only fixed	4.06	5.18	4.49	6.83
	GNSS+ISL fixed	0.15	4.90	4.49	6.36
99.7% ( $3\sigma$ )	GNSS-only fixed	6.30	8.70	8.04	10.07
	GNSS+ISL fixed	0.23	8.29	7.33	9.72

**Table 8.2:** Percentiles of the relative position errors of the fixed solutions, considering the incorporation of all error sources throughout the entire month of April 2022. The 3-sigma percentiles in the direction of Sagittarius A\* are highlighted in red.

## 8.4. Result Consistency with Multiple Seeds

The focus is now on exploring the generalizability of the results presented in the previous section, which were obtained using a specific seed for the pseudo-random number generator. To assess the consistency and robustness of these findings, the simulation was repeated six more times, each time

using a different seed while keeping the nominal configuration constant. The objective is to examine the variation of the results, enabling an assessment of the stability and reliability of the outcomes.

To evaluate the variability of the results, the mean and standard deviation of the relative orbit comparisons were computed for each epoch using data from all seven different seeds. Figure 8.9 presents this relative orbit comparison projected in the ISL-SGRA frame. To capture the variability across different seeds, this figure displays an envelope of the orbit comparison. This envelope is constructed by plotting the (mean + standard deviation) and (mean - standard deviation) curves. Only the fixed solutions are depicted in this figure due to their superior performance compared to the float solution.

Figure 8.9 reaffirms that the ISL observations primarily enhance the determination of the baseline in their own direction, while the benefits in the other two directions remain unclear. In the Sagittarius A\* direction, both the GNSS-only fixed and GNSS+ISL fixed solutions present errors within the range of -10 mm to 10 mm, consistent with the findings from the previous section. In contrast, the evolution of the errors appears smoother in this analysis, with fewer pronounced peaks. This smoothing effect occurs because the peaks from individual seeds do not always coincide at the same epochs, reducing their impact when averaging over multiple seeds.

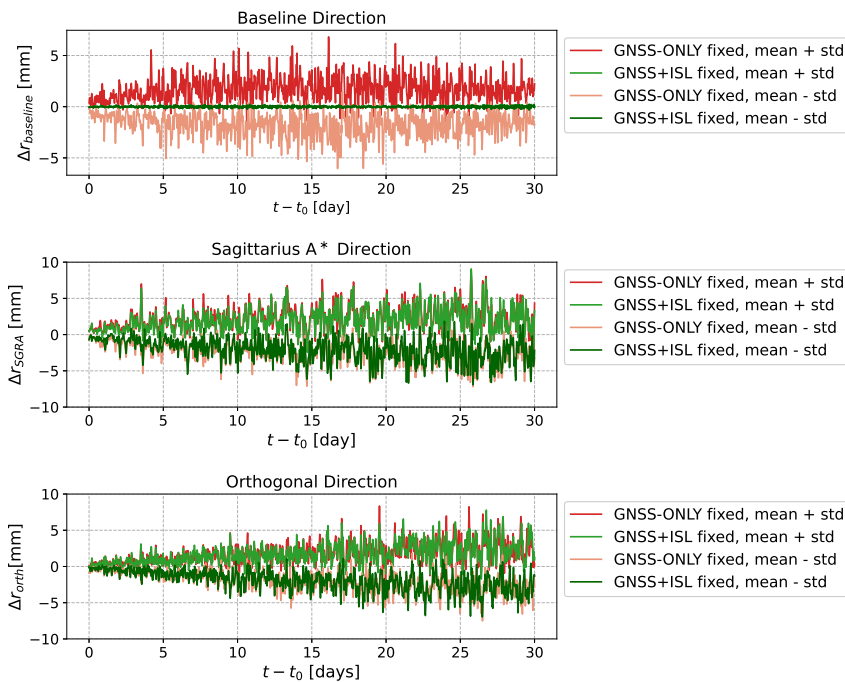


**Figure 8.9:** Envelope of variability for the relative orbit comparison from multiple seeds, projected into the ISL-SGRA frame. The mean + standard deviation and mean - standard deviation curves are depicted for the GNSS-only fixed and GNSS+ISL fixed solutions.

Table 8.3 summarizes the average mean, RMS, and maximum values obtained when averaging over multiple seeds. When comparing these results to the single-seed results in Table 8.1, it is observed that the multiple-seed results show slightly worse statistics. Focusing on the Sagittarius A\* direction, the RMS was previously recorded as 2.59 mm for the GNSS-only fixed solution and 2.28 mm for the GNSS+ISL fixed solution. In the current analysis, the RMS values have increased to 2.76 mm and 2.54 mm, respectively. However, it is worth noting that the GNSS+ISL solution still exhibits a slightly better RMS value compared to the GNSS-only solution.

Solution	Stat.	Baseline [mm]	Sgr A* [mm]	Ortho. [mm]	3D [mm]
GNSS-only float	Mean	-0.03	0.13	-0.35	11.57
	RMS	6.63	8.15	7.12	13.23
	Max	24.24	29.85	27.92	40.91
GNSS-only fixed	Mean	-0.01	-0.04	-0.10	3.68
	RMS	2.08	2.76	2.32	4.21
	Max	8.09	10.01	8.97	12.03
GNSS+ISL fixed	Mean	-0.004	0.07	-0.08	2.97
	RMS	0.076	2.54	2.27	3.60
	Max	0.240	9.72	8.53	11.65

**Table 8.3:** Summary of the average comparison results between estimated relative orbit and reference relative orbit obtained from multiple seeds for different solutions, considering the incorporation of all error sources throughout the entire month of April 2022. The RMS in the direction of Sagittarius A\* is highlighted in red.

To further examine the sensitivity to the selected seed, a percentile analysis was conducted using the multiple-seed setup. In this analysis, the results from all seeds were used, without employing the epoch-wise mean, to ensure that the peaks were not smoothed out. Table 8.4 presents the calculated 68%, 99.5%, and 99.7% values for both fixed solutions.

Compared to the previous single-seed results, the 3-sigma value in the direction of the black hole is slightly higher. For the GNSS+ISL fixed solution, this value was previously recorded as 8.29 mm and has now increased to 8.59 mm in the multiple-seed analysis. Nevertheless, it remains true that the GNSS+ISL solution demonstrates marginally better performance in terms of the 3-sigma values compared to the GNSS-only solution. This observation holds for every single-seed solution as well.

Percentile	Solution	Baseline [mm]	Sgr A* [mm]	Ortho. [mm]	3D [mm]
68% ( $1\sigma$ )	GNSS-only fixed	1.98	2.58	2.05	4.28
	GNSS+ISL fixed	0.08	2.32	1.96	3.62
95% ( $2\sigma$ )	GNSS-only fixed	4.15	5.67	4.88	7.53
	GNSS+ISL fixed	0.15	5.30	4.89	6.95
99.7% ( $3\sigma$ )	GNSS-only fixed	6.69	9.17	8.40	10.98
	GNSS+ISL fixed	0.23	8.59	8.30	10.53

**Table 8.4:** Percentiles of the relative position errors obtained from multiple seeds for the fixed solutions, considering the incorporation of all error sources throughout the entire month of April 2022. The 3-sigma percentiles in the direction of Sagittarius A\* are highlighted in red.

In summary, the results obtained from different seeds demonstrate a consistent overall performance with small variations of the relative position error peak values. The original seed may present a somewhat optimistic scenario, as the RMS and 3-sigma values were found to be slightly lower than the average values. Nonetheless, the general findings remain unchanged. Firstly, the fixed solutions significantly outperform the float solutions, highlighting the importance of ambiguity fixing. Secondly, the ISL observations enhance significantly the determination of the baseline in their own direction, but with modest improvements observed in the Sagittarius A\* direction.

## 8.5. Sensitivity to Errors in the GNSS Orbits and Clocks

The main goal of this section is to investigate the sensitivity of the relative orbit accuracy to errors in the GNSS orbits and clocks. This analysis is crucial as it has been identified in Chapter 7 that errors in the GNSS products are among the most dominant sources of error in the estimation process. The focus will be on presenting the results of the GNSS+ISL fixed estimation.

In this sensitivity analysis, the impact of different values of the standard deviation of the sinusoidal orbit error amplitude ( $\sigma_A$ ) and the Gauss-Markov clock errors ( $\sigma_w$ ) is studied. The correlation time ( $\tau_\delta$ ) of the Gauss-Markov clock errors remains fixed at its nominal value of 30 min for the sake of simplicity. For this analysis, the values of  $\sigma_A$  and  $\sigma_w$  are modified by 25%, 50%, 75%, and 125% from their nominal values, which can be found in Table 5.9. All the different case scenarios considered in this sensitivity analysis are summarized in Table 8.5.

Scenario	$\sigma_A$ [cm]	$\sigma_w$ [ps]
25%NOMINAL	0.5	17.5
50%NOMINAL	1.0	35.0
75%NOMINAL	1.5	52.5
NOMINAL	2.0	70.0
125%NOMINAL	2.5	87.5

**Table 8.5:** Scenarios for sensitivity analysis to errors in the GNSS orbits and clocks. Summarizes different scenarios with varying sinusoidal orbit errors ( $\sigma_A$ ) and Gauss-Markov clock errors ( $\sigma_w$ ), while keeping correlation time fixed.

To investigate the sensitivity of the relative orbit accuracy to errors in the GNSS orbits and clocks, it is important to consider the 3-sigma metric. This metric is particularly relevant because the requirements of the mission are defined based on this measure of uncertainty. In Figure 8.10, the 3-sigma values of the 3D error and the error projected in the ISL-SGRA frame are presented for all five scenarios alongside the requirement threshold. The results exhibit a relatively linear relationship, where increasing errors in the GNSS products corresponds to higher 3-sigma values of the relative orbit error. As expected, the ISL direction yields the most favourable accuracy results.

Figure 8.10 indicates that only the ‘25%NOMINAL’ scenario, where the nominal errors are reduced by 75%, satisfies the requirement of having a 3-sigma value lower than 3.5 mm in the Sagittarius A\* direction. Nevertheless, based on the observed linear trend in this figure, it can be inferred that the requirement could be met if errors are lower than 40% of the nominal errors. These 40% nominal errors correspond to a standard deviation of 8 mm for harmonic orbit errors and a standard deviation of 28 ps for Gauss-Markov clock errors.

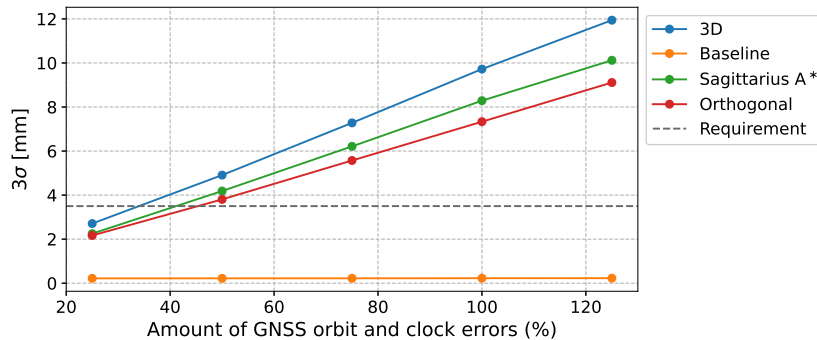


**Figure 8.10:** Sensitivity analysis of 3-sigma values for the GNSS+ISL fixed solution for different scenarios with varying GNSS orbit and clock errors, showing the 3-sigma values of the 3D error and the error projected in ISL-SGRA frame. The requirement of 3.5 mm is illustrated with a dashed line.

## 8.6. Sensitivity to Uncertainties in the Dynamical Model

This section explores the importance of uncertainties in the dynamical model. The approach involves removing errors in the geopotential and SRP models, as well as excluding the estimation of empirical accelerations. This ensures that the same dynamical model is used for both simulating the observations and estimation. The remaining errors, such as those associated with the GNSS clocks and orbits, are introduced at their nominal values.

Figure 8.11 presents the comparison of the estimated relative orbit and the reference relative orbit for the GNSS-only float, GNSS-only fixed, and GNSS+ISL fixed solutions throughout the entire month

of April. Consistent with the findings when dynamical model errors were introduced, the fixed solutions outperform the float solutions, and incorporating the ISL measurements does not appear to provide a significant advantage in terms of the overall relative position error. However, the accuracy of all three solutions is notably improved when no dynamical error errors are introduced. Additionally, the comparison reveals a more oscillatory daily behaviour, which may be attributed to the absence of empirical accelerations that typically mitigate errors associated with the orbital period.

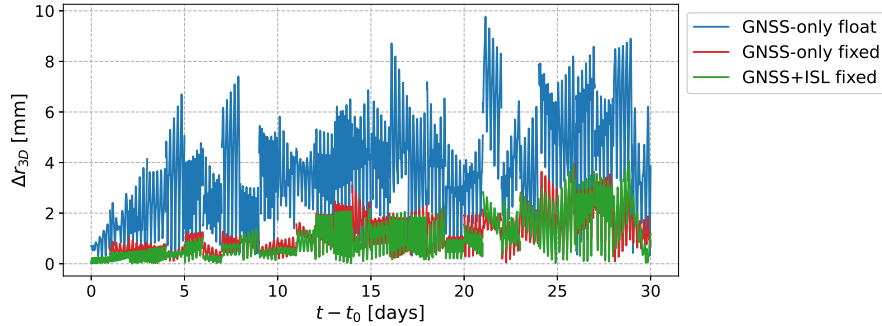


**Figure 8.11:** Comparison of the estimated relative orbit with the reference relative orbit for the whole month of April, when no dynamical model errors are introduced. Results are shown for GNSS-only float, GNSS-only fixed, and GNSS+ISL fixed solutions.

Furthermore, Figure 8.12 presents the same orbit comparison, but now the results are projected in the ISL-SGRA frame, specifically focusing on the fixed solutions. As anticipated, the baseline projection that aligns with the ISL observations exhibits the highest accuracy. In this case, the relative position error in the Sagittarius A\* direction ranges from -3 mm to 3 mm, which contrasts with the broader -10 mm to 10 mm range observed when dynamical errors are present.

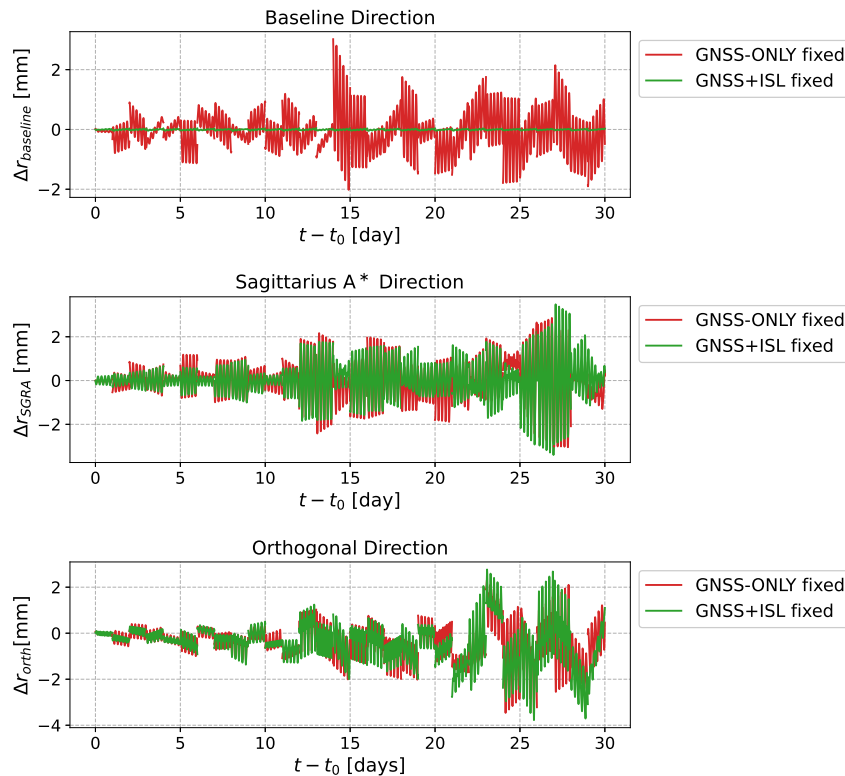


**Figure 8.12:** Comparison of the estimated relative orbit with the reference relative orbit projected in the ISL-SGRA frame for the fixed solutions for the whole month of April, when no dynamical model errors are introduced.

Figure 8.11 and Figure 8.12 also demonstrate that the dependency of the relative orbit accuracy

on the baseline distance is not solely attributed to dynamical errors but is also influenced by errors introduced into the observations. Focusing on the GNSS+ISL fixed results, the RMS of the relative position error in the Sagittarius A\* direction is 0.72 mm. This value contrasts with the 2.38 mm obtained when introducing also the dynamical model errors into the estimation process.

Table 8.6 presents the 3-sigma values in all directions for both fixed solutions. In the direction of the black hole, the GNSS-only solution has a 3-sigma value of 2.53 mm, while the GNSS+ISL solution has a 3-sigma value of 2.44 mm. Both values are below the 3.5 mm threshold, indicating successful fulfillment of the relative navigation requirement in both scenarios. These results emphasize the importance of accurately modeling the dynamics of the problem in order to meet the stringent mission requirements.

Percentile	Solution	Baseline [mm]	Sgr A* [mm]	Ortho. [mm]	3D [mm]
99.7% ( $3\sigma$ )	GNSS-only fixed	2.41	2.53	3.20	3.57
	GNSS+ISL fixed	0.05	2.44	3.07	3.54

**Table 8.6:** 3-sigma values of the relative position errors for the fixed solutions throughout the entire month of April 2022, when no dynamical model errors are introduced. The 3-sigma percentiles in the direction of Sagittarius A\* are highlighted in red.

# Conclusions and Future Work

Throughout the preceding chapters, this thesis has extensively explored the challenges and complexities associated with achieving precise relative positioning in a two-satellite constellation operating in Medium Earth Orbit for the purpose of black hole imaging. This chapter serves as the culmination of this research, summarizing the key findings extracted from the conducted simulations. Moreover, it highlights crucial areas that require further investigation, making suggestions for future work in this field of study.

## 9.1. Conclusions

In this thesis, the focus was on investigating the use of Global Navigation Satellite Systems (GNSS) observations together with optical Intersatellite Link (ISL) observations in a two-satellite constellation operating in Medium Earth Orbit. The primary objective was to evaluate the feasibility of meeting the demanding relative navigation requirements necessary for the imaging of black holes, specifically targeting the precise baseline determination in the direction of the black hole of interest, Sagittarius A\*. The thesis aimed to provide insights into the limitations of precise relative positioning in high-dynamic constellations with significant intersatellite distances. The following paragraphs summarize the key conclusions derived from this research.

One of the key findings of this thesis is the crucial role of integer ambiguity resolution in achieving the demanding relative navigation requirements of the mission. It was determined that fixing the ambiguities to an integer value leads to a significant enhancement in the accuracy of the relative orbit determination. This improvement is evident not only in the three-dimensional relative position error but also when examining its projection along the Sagittarius A\* direction. For instance, in the black hole direction, the GNSS-only float solution has a root-mean-square (RMS) of the relative position error of 7.43 mm, whereas it drops to 2.59 mm for the GNSS-only fixed solution. These numbers highlight the substantial improvement achieved by resolving the integer ambiguities, emphasizing the importance of this step.

Interestingly, previous studies conducted on this mission by Guindal-Martinez (2020) and GMV (2022) primarily focused on float ambiguities and did not explore the full potential of ambiguity fixing. Thus, this thesis makes a novel contribution by demonstrating the substantial performance improvement achieved through the application of integer ambiguity resolution techniques. This finding emphasizes the importance of incorporating ambiguity fixing methods into the navigation algorithms of future space-based systems, particularly those with stringent accuracy requirements and challenging mission objectives.

In terms of employing the ISL for improving relative orbit accuracy, the analysis revealed that the ISL primarily contributed to a more precise estimation of the baseline in the direction corresponding to the ISL observations. In this specific direction, the RMS of the relative orbit error was below 0.1 mm, while it reached 1.99 mm when relying solely on GNSS observations. Although the exceptional accuracies achieved in this direction may not be necessary for the mission examined in this thesis, they hold great promise for other mission scenarios where this direction plays a prominent role, which is indeed a common phenomenon in various mission types.

However, when examining the baseline projection along the Sagittarius A\* direction, the introduction of the ISL observations resulted in only a modest enhancement. The performance improvement in this critical direction was observed to be relatively minor, with an approximate 8% improvement in the RMS and a 5% improvement in the 3-sigma variables when compared to the results obtained using GNSS observations alone. Despite this, it is worth noting that the achieved relative accuracy in this direction

remains relatively accurate, with the maximum relative error for the GNSS+ISL fixed solution being 8.71 mm.

Therefore, it can be concluded that the utilization of the ISL observations does not significantly contribute to meeting the specific relative navigation requirements of this mission. While a slight improvement can be observed, it is important to acknowledge that several assumptions were made in the modeling of the ISL observations. For instance, the assumption of Gaussian noise may not accurately represent the true noise characteristics, and neglecting clock bias errors may oversimplify the analysis. If these assumptions are relaxed, it is possible that the ISL would provide even less benefit in determining the baseline distance in the direction of the black hole.

During the analysis, it was observed that the accuracy of the relative orbit was influenced by the baseline distance between the satellites. This effect can be attributed to two main factors. Firstly, when the satellites are in close proximity, they experience relatively similar dynamical model errors, leading to the cancellation of these common errors when computing the relative orbit. However, as the satellites drift apart, they are subject to different dynamical model errors, which do not cancel out during the computation of the relative orbit.

Secondly, the number of common GNSS satellites in view also plays a role. When the satellites are closer together, they have a larger overlap in terms of visible GNSS satellites. As a result, the errors associated with these common satellites tend to be reduced during the computation of the relative distance. Nevertheless, as the satellites move further apart, the number of common satellites in view decreases, resulting in a limited reduction of these shared errors when computing the relative orbit.

However, it was observed that the relationship between relative orbit accuracy and baseline distance is non-linear. Some error peaks were identified at medium baselines that exceeded the magnitude of peaks observed at longer baselines. This non-linear behaviour arises because the relationship between baseline length and relative dynamical model errors is not solely determined by the size of the baseline. Rather, when the satellites are significantly away from each other, the error behaviour is influenced by how different the specific dynamical perturbation introduced in each satellite is. Similarly, the relationship between baseline distance and the number of GNSS satellites in common view is also non-linear and exhibits a more complex pattern. Surprisingly, it was found that the number of common satellites reaches a minimum during the middle of the mission time frame.

As a result of this baseline dependency, the relative position errors escalate as the satellites progressively separate from each other. Consequently, the objective of attaining a 1-dimensional relative position accuracy of 3.5 mm (3-sigma) along the Sagittarius A\* direction is not met. The obtained 3-sigma value is around 8 mm, and a mere 86.3% of the observations meet this requirement, falling significantly short of the desired 99.7% threshold (3-sigma).

To fulfill the aforementioned requirement, it is advisable to focus on mitigating the most significant sources of error. The analysis identified that errors in the GNSS orbits and clocks, along with errors in the geopotential model, had a considerably greater impact on the accuracy of the relative position compared to other types of errors such as thermal noise in the GNSS observations. These dominant error sources exhibited an influence that was one to two orders of magnitude higher than the impact of other error sources, particularly as the satellites progressively separated and the baseline distance increased. Thus, it is strongly recommended to implement mitigation strategies specifically targeting these two error sources.

Achieving the mission requirements necessitates exceptionally precise GNSS orbits and clocks. Only by reducing the nominal considered errors by more than 60% was it feasible to meet the relative navigation requirement. Specifically, the orbital harmonic errors should have a standard deviation of less than 8 mm, while the Gauss-Markov clock errors should have a standard deviation of less than 28 ps. Moreover, errors in the geopotential model play a dominant role in achieving the required accuracy. Meticulously modeling the dynamics of the problem, including the accurate representation of geopotential effects, is vital for meeting the stringent mission requirements.

Lastly, it is important to highlight that the proposed modified ECOM empirical model, known as ECOM-SGRA, which takes into account the specific attitude law of the EHI satellites, proved to be highly effective in capturing the influence of solar radiation pressure. In comparison to the standard ECOM model, ECOM-SGRA provided more accurate results for this particular mission. It was determined that the 9 ECOM-SGRA coefficients, which include the constant, sine, and cosine parameters in each direction of the ECOM-SGRA frame, gave the best results. Considering that the orbital period of the EHIs is approximately 5 hours, the 34-hour estimation arc for these satellites should be divided into 7

sub-intervals to estimate a set of ECOM-SGRA coefficients for each orbital revolution.

Furthermore, it was observed that no additional empirical accelerations, such as Cycle-Per-Revolution (CPR) accelerations, need to be introduced as the ECOM-SGRA model already absorbs the effects typically accounted for by CPRs. Introducing additional empirical accelerations results in an overparameterization of the problem, causing difficulties for the least-square algorithm in handling the highly precise ISL observations. For this reason, it is recommended to rely solely on the ECOM-SGRA model without introducing additional empirical accelerations for optimal results in terms of accuracy and computational efficiency.

In summary, this thesis has provided valuable insights into the challenges associated with achieving very precise relative positioning in a two-satellite constellation operating in MEO. The findings demonstrate the important role of integer ambiguity resolution, the limited benefits of employing the ISL for this particular mission, and the non-linear relationship between relative orbit accuracy and baseline distance. Although the current configuration is not able to meet the demanding relative navigation requirement, mitigating errors in the GNSS orbits and clocks along with accurately modeling the dynamics of the problem are key to fulfilling this requirement. In this way, the mission's ultimate objective of imaging black holes with exceptional resolution might be realized, paving the way for groundbreaking advancements in the field of astrophysics.

## 9.2. Future Work

This section identifies the research directions that remain open for further investigation. Throughout this study, certain assumptions were made regarding the simulation of the GNSS and ISL observations, which may need reconsideration in future research. Furthermore, it was observed that the use of the ISL did not significantly contribute to meeting the relative positioning requirements of the EHI mission. Therefore, alternative approaches should be explored to address this challenge.

### 9.2.1. Assumptions Reconsideration

First of all, it is important to remark the relevance of correctly modeling the solar radiation pressure effect in this study, given that it is the main non-gravitational perturbing acceleration. Although the ECOM-SGRA model was successfully validated and utilized in this thesis, its definition is closely linked to the attitude law of the satellite. Currently, the attitude law employed is a simple inertial pointing law, but it is expected to undergo refinement in the future to not only point towards the black hole but also optimize solar panel illumination. In such cases, redefining the ECOM model would be necessary. Also, considering a hybrid SRP model that combines an empirical model with an a priori analytical model could be another alternative to capture SRP effects.

Moreover, it should be noted that multipath effects were neglected in the simulation of the GNSS observations. This assumption was grounded in the fact that space-borne receivers are less susceptible to multipath compared to their ground-based counterparts. It was also assumed that the estimated Phase Centre Variation (PCV) maps would largely absorb multipath errors if there are no moving parts in the satellite. However, if a more sophisticated attitude law is implemented, leading to the rotation of the solar panels or the satellite body, the impact of multipath effects could become significant and thus need to be taken into account.

The simulation of the GNSS instrumental delays should also be reconsidered, taking into account their coupling with the simulation of GNSS clocks. The current approach oversimplifies the modeling process by treating instrumental delays and clock simulation independently, while in reality, they are interconnected. In practice, analysis centres of the International GNSS Service (IGS) simultaneously compute instrumental delays and clocks, reflecting their mutual influence. The neglected intersystem bias between the clocks of the GPS and Galileo constellations should also be considered in the simulations. This integrated approach would probably improve the realism of the simulation of the GNSS products.

Furthermore, it was assumed that the position of the centre of mass of the spacecraft and the location of the GNSS and ISL phase centers are perfectly known. However, in reality, these parameters are subject to uncertainty. It would be valuable to explore the impact of deviations in these parameters on the accuracy of relative orbit determination. This investigation would provide valuable insights into the practical challenges associated with the imprecise knowledge of these variables.

To improve the understanding of the impact of the ISL observations on orbit determination, several

aspects related to their modeling can be explored. One potential approach is conducting a sensitivity analysis of the ISL noise by adjusting the level of white noise introduced into the ISL observations. This would provide a better understanding of the system performance under different laser precision levels. Although this analysis may not directly benefit the specific mission studied in this thesis, it can optimize the characterization of ISL noise in other mission scenarios.

The current ISL model relies also on a simplistic Gaussian noise assumption, which may not fully capture the complexities of the link. It would be advisable to incorporate a more complex noise model that takes into account the characteristics of the optical instrument and factors such as the baseline distance. Implementing this noise model requires a better definition of the ISL instruments, particularly in terms of gain and power properties. Additionally, further investigation is needed to understand potential errors related to the synchronization of the ISL clocks with the GNSS clocks, even when employing two-way ranging.

### 9.2.2. Exploring Alternative Approaches

In addition to the previous considerations, there are several alternative approaches that can be explored to enhance the accuracy of baseline determination in the direction of the black hole. One possibility would be to adjust the GPS tracking channel allocation to favour satellites that are in common view. By doing so, the number of common observations can be increased, which in turn enables the removal of more shared errors when calculating the relative distance. This approach is expected to be even more effective when incorporating additional GNSS constellations, such as BeiDou, as it provides a larger pool of satellites to choose from for common observations.

Another approach worth investigating is a network processing scheme, where the orbits and clocks of both GNSS satellites and receivers are simultaneously estimated. This processing scheme offers the opportunity to not only estimate the GNSS products but also other parameters such as ground station coordinates. By integrating all these variables into the estimation process, improved consistency within the problem might be achieved. A network approach has the potential to mitigate the impact of errors in the GNSS products and may be particularly effective in eliminating instrumental delays.

Additionally, exploring the potential synergies between the ground-based VLBI telescopes of the Event Horizon Telescope (EHT) array and the EHI mission presents an intriguing opportunity. By combining the strengths of both systems, it might be possible to obtain higher resolution images of the target black holes while potentially reducing the requirement for precise baseline determination.

Lastly, the analysis conducted in this thesis has focused on post-processing relative navigation. Nevertheless, an interesting line for future research would be to explore real-time relative navigation, which is particularly relevant for implementing onboard processing of the VLBI observations. Real-time navigation presents an additional challenge, as real-time GNSS products have higher error levels compared to final products. Although the impact of these errors is typically mitigated by employing double-differenced observables, this approach may not be feasible for the mission at hand due to the limited number of satellites in common view as the intersatellite distance increases. Hence, alternative strategies might need to be investigated to handle the unique constraints of real-time relative navigation in this mission context.

By addressing the previously mentioned aspects in future research, notable progress can be made in the field of precise relative navigation using MEO constellations. The inclusion of more realistic noise models will enhance the fidelity of the simulations, enabling a better representation of real-world conditions. Furthermore, the exploration of alternative approaches, such as network processing schemes, shows potential for improving baseline determination accuracy. Continued efforts in these areas will contribute to the continuous development of the relative navigation field, ultimately benefiting not just the EHI mission but also other missions with demanding relative accuracy requirements.

# References

- Abich, K., et al. (2019). In-Orbit Performance of the GRACE Follow-on Laser Ranging Interferometer. *Physical Review Letters*, 123. <https://doi.org/10.1103/PhysRevLett.123.031101>
- Akiyama, K., Alberdi, A., Alef, W., Asada, K., Azulay, R., Baczko, A.-K., Ball, D., Baloković, M., Barrett, J., Bintley, D., Blackburn, L., Boland, W., Bouman, K. L., Bower, G. C., Bremer, M., Brinkerink, C. D., Brissenden, R., Britzen, S., Broderick, A. E., ... Ziurys, L. (2019). First M87 Event Horizon Telescope Results. I. The Shadow of the Supermassive Black Hole. *The Astrophysical Journal Letters*, 875(1). <https://doi.org/10.3847/2041-8213/ab0ec7>
- Alawieh, M., Hadaschik, N., Franke, N., & Mutschler, C. (2016). Inter-Satellite Ranging in the Low Earth Orbit. *10th International Symposium on Communication Systems, Networks and Digital Signal Processing*. <https://doi.org/10.1109/CSNDSP.2016.7573920>
- Allende-Alba, G., Montenbruck, O., Hackel, S., & Tossaint, M. (2018). Relative positioning of formation-flying spacecraft using single-receiver GPS carrier phase ambiguity fixing. *GPS Solutions*, 22(68). <https://doi.org/10.1007/s10291-018-0734-x>
- Amaro-Seoane, P., et al. (2019). Laser Interferometer Space Antenna: LISA. Albert Einstein Institute Hannover. <https://doi.org/10.48550/arXiv.1702.00786>
- Armano, M., et al. (2022). Sensor noise in LISA Pathfinder: An extensive in-flight review of the angular and longitudinal interferometric measurement system. *Physical Review*, 106. <https://doi.org/10.1103/PhysRevD.106.082001>
- Arnold, D., Meindl, M., Beutler, G., Dach, R., Schaer, S., Lutz, S., Prange, L., Sosnica, K., Mervart, L., & Jäggi, A. (2015). CODE's new solar radiation pressure model for GNSS orbit determination. *Journal of Geodesy*, 89, 775–791. <https://doi.org/10.1007/s00190-015-0814-4>
- Astrium GmbH. (n.d.). Artist's impression of the CHAMP-Satellite [Online; accessed February 20, 2023]. [https://www.dlr.de/rd/en/desktopdefault.aspx/tabid-2440/3586\\_read-5330/gallery-1/gallery\\_read-Image.28.20172/](https://www.dlr.de/rd/en/desktopdefault.aspx/tabid-2440/3586_read-5330/gallery-1/gallery_read-Image.28.20172/)
- Ávila-Rodríguez, J. (2018). *On Generalized Signal Waveforms for Satellite Navigation* (Doctoral dissertation). University of Munich. <https://d-nb.info/1066345600/34>
- Bai, Y., Guo, Y., Wang, X., & Lu, X. (2020). Satellite-Ground Two-Way Measuring Method and Performance Evaluation of BDS-3 Inter-Satellite Link System. *IEEE Access*, 8. <https://doi.org/10.1109/ACCESS.2020.3019607>
- Balakrishnan, K. (2013). Inter-satellite ranging for geodesy, formation flying, and fundamental physics in space. Department of Aeronautics and Astronautics: Stanford University.
- Bancroft, S. (1985). An Algebraic Solution of the GPS Equations. *IEEE Transactions on Aerospace and Electronic Systems*, 21(1), 56–59. <https://doi.org/10.1109/TAES.1985.310538>
- Bauer, F. (2015). GPS Space Service Volume (SSV) Ensuring Consistent Utility Across GPS Design Builds for Space Users. *5th Space-Based Positioning, Navigation & Timing Advisory Board Meeting*.
- Bouridah, A., Andres, Y., & Montenbruck, O. (2021). Sentinel-6A - PODRIX Overview. *10th Copernicus Operational Service Quality Working Group meeting*.
- Bury, G., Sosnica, K., Zajdel, R., & Strugarek, D. (2020). Toward the 1-cm Galileo orbits: challenges in modeling of perturbing forces. *Journal of Geodesy*, 94(16). <https://doi.org/10.1007/s00190-020-01342-2>
- Capitaine, N., Guinot, B., & McCarthy, D. (2000). Definition of the Celestial Ephemeris Origin and of UT1 in the International Celestial Reference Frame. *Astronomy and Astrophysics*, 355, 398–405.
- Chen, L., Bai, X.-Z., Liang, Y.-G., & Li, K.-B. (2017). Orbital Prediction Error Propagation of Space Objects. In *Orbital data applications for space objects: Conjunction assessment and situation analysis* (pp. 23–75). Springer Singapore. [https://doi.org/10.1007/978-981-10-2963-9\\_2](https://doi.org/10.1007/978-981-10-2963-9_2)
- Colombo, O. (1989). The dynamics of Global Positioning System orbits and the determination of precise ephemerides. *Journal of Geophysical Research Atmospheres*, 94. <https://doi.org/10.1029/JB094iB07p09167>
- Conrad, A., Axelrad, P., Haines, B., Zuffada, C., & O'Brien, A. (2023). Improved GPS-Based Single-Frequency Orbit Determination for the CYGNSS Spacecraft Using GipsyX. *Journal of the Institute of Navigation*, 70(1). <https://doi.org/10.33012/navi.565>

- Curtis, H. (2014). *Orbital mechanics for engineering students* (Third). Elsevier Ltd. <https://doi.org/10.1016/C2011-0-69685-1>
- Dornier Satellitensysteme GmbH. (2000). *Study of Laser Interferometer Space Antenna: Final Technical Report* (tech. rep. LI-RP-DS-009).
- EHT Collaboration. (2022). Astronomers Reveal First Image of the Black Hole at the Heart of Our Galaxy [Online; accessed May 14, 2023]. <https://eventhorizontelescope.org/blog/astronomers-reveal-first-image-black-hole-heart-our-galaxy>
- Fernandez, J. (2022). *MAORI design principles* (tech. rep. GMV-MAORI-MEM-0001). GMV.
- Friis-Christensen, E., Lühr, H., & Hulot, G. (2006). Swarm: A constellation to study the Earth's magnetic field. *Earth Planets and Space*, *58*, 351–358. <https://doi.org/10.1186/BF03351933>
- Galleani, L., Sacerdote, L., Tavella, P., & Zucca, C. (2003). A mathematical model for the atomic clock error. *Metrologia*, *40*(3). <https://doi.org/10.1088/0026-1394/40/3/305>
- Gao, P., & You, Z. (2006). Present Status and Perspectives about Measurement Technology of Inter-Satellite Relative Position and Relative Attitude. *Proceedings of International Conference on Space Information Technology*. <https://doi.org/10.1117/12.658359>
- Ge, M., Gendt, G., Dick, G., & Zhang, F. P. (2005). Improving carrier-phase ambiguity resolution in global GPS network solutions. *Journal of Geodesy*, *79*, 103–110. <https://doi.org/10.1007/s00190-005-0447-0>
- Giorgi, G., Schmidt, T., Trainotti, C., Mata-Calvo, R., Fuchs, C., Hoque, M., Berdermann, J., Furthner, J., Günther, C., Schuldt, T., Sanjuan, J., Gohlke, M., Oswald, M., Braxmaier, C., Balidakis, K., Dick, G., Flechtner, F., Ge, M., Glaser, S., ... Schuh, H. (2019a). Advanced technologies for satellite navigation and geodesy. *Advances in Space Research*, *64*(6), 1256–1273. <https://doi.org/10.1016/j.asr.2019.06.010>
- Giorgi, G., Kroese, B., & Michalak, G. (2019b). Future GNSS constellations with optical inter-satellite links. Preliminary space segment analyses. *2019 IEEE Aerospace Conference*, 1–13. <https://doi.org/10.1109/AERO.2019.8742105>
- GMV. (2013). Precise orbit determination for ESA's Sentinel missions [Accessed: 01/05/2023]. <https://www.gmv.com/en-es/communication/news/precise-orbit-determination-esas-sentinel-missions>
- GMV. (2020). *PRP-MEO: Inter Satellite Link / Inter-Satellite Link Reference Centre Model* (tech. rep. NAVISP1-TN-GMV-024-04).
- GMV. (2022). *PRP-MEO: Final Report* (tech. rep. NAVISP1-TN-GMV-024-17).
- Guindal-Martinez, A. (2020). *Precise absolute and relative navigation in Medium-Earth Orbits by means of Global Navigation Satellite Systems and Inter-Satellite Links* (Master's thesis). Delft University of Technology.
- Guo, J., Qi, L., Liu, X., Chang, X., Ji, B., & Zhang, F. (2023). High-order ionospheric delay correction of GNSS data for precise reduced-dynamic determination of LEO satellite orbits: cases of GOCE, GRACE, and SWARM. *GPS Solutions*, *27*(13). <https://doi.org/10.1007/s10291-022-01349-6>
- Guo, X., Geng, J., Chen, X., & Zhao, Q. (2020). Enhanced orbit determination for formation-flying satellites through integrated single- and double-difference GPS ambiguity resolution. *GPS Solutions*, *24*(14). <https://doi.org/10.1007/s10291-019-0932-1>
- Hauschild, A., & Montenbruck, O. (2021). Precise real-time navigation of LEO satellites using GNSS broadcast ephemerides. *Journal of the Institute of Navigation*, *68*(2), 419–432. <https://doi.org/10.1002/navi.416>
- Jalabert, E., & Mercier, F. (2018). Analysis of South Atlantic Anomaly perturbations on Sentinel-3A Ultra Stable Oscillator. Impact on DORIS phase measurement and DORIS station positioning. *Advances in Space Research*, *62*, 174–190. <https://doi.org/10.1016/j.asr.2018.04.005>
- Jeganathan, M., & Dubovitsky, S. (2000). Demonstration of nanometer-level active metrology for long-range interferometric displacement measurements. *Proceedings of SPIE - The International Society of Optical Engineering*. <https://doi.org/10.1117/12.390165>
- Kaplan, E., & Hegarty, C. (2006). *Understanding GPS Principles and Applications*. Artech House.
- Kaushal, H., & Kaddoum, G. (2017). Optical Communication in Space: Challenges and Mitigation Techniques. *IEEE Communications Surveys & Tutorials*, *19*, 57–96. <https://doi.org/10.1109/COMST.2016.2603518>

- Kornfeld, R., Arnold, B., Gross, M., Dahya, N., Klipstein, W., Gath, P., & Bettadpur, S. (2019). GRACE-FO: The Gravity Recovery and Climate Experiment Follow-On Mission. *Journal of Spacecraft and Rockets*, 56. <https://doi.org/10.2514/1.A34326>
- Kroes, R., Montenbruck, O., Bertiger, W., & Visser, P. (2005). Precise GRACE baseline determination using GPS. *GPS Solutions*, 9, 21–31. <https://doi.org/10.1007/s10291-004-0123-5>
- Kudriashov, V., Martin-Neira, M., Roelofs, F., Falcke, H., Brinkerink, C., Baryshev, A., Hogerheijde, M., Young, A., Pourshaghghi, H., Klein-Wolt, M., Moscibrodzka, M., Davelaar, J., Barat, I., Duesmann, B., Valenta, V., Perdigues-Armengol, J. M., De Wilde, D., Martin-Iglesias, P., Alagha, N., & Van Der Vorst, M. (2021). An Event Horizon Imager (EHI) Mission Concept Utilizing Medium Earth Orbit Sub-mm Interferometry. *Chinese Journal of Space Science*, 41(2), 211. <https://doi.org/10.11728/cjss2021.02.211>
- Laaraiedh, M., Avrillon, S., & Uguen, B. (2011). Cramer–Rao lower bounds for nonhybrid and hybrid-localisation techniques in wireless networks. *European Transactions on Telecommunications*, 23. <https://doi.org/10.1002/ett.1530>
- Laurichesse, D., Mercier, F., Berthias, J.-P., Broca, P., & Cerri, L. (2009). Integer Ambiguity Resolution on Undifferenced GPS Phase Measurements and Its Application to PPP and Satellite Precise Orbit Determination. *Journal of the Institute of Navigation*, 56(2), 135–149. <https://doi.org/10.1002/j.2161-4296.2009.tb01750.x>
- Loscher, A. (2010). Atmospheric influence on a laser beam observed on the OICETS – ARTEMIS communication demonstration link. *Atmospheric Measuring Techniques*, 3, 1233–1239. <https://doi.org/10.5194/amt-3-1233-2010>
- Mao, X., Visser, P., & van den IJssel, J. (2019a). Absolute and relative orbit determination for the CHAMP/GRACE constellation. *Advances in Space Research*, 63, 3816–3834. <https://doi.org/10.1016/j.asr.2019.02.030>
- Mao, X., Visser, P., & van den IJssel, J. (2019b). High-dynamic baseline determination for the Swarm constellation. *Aerospace Science and Technology*, 88, 329–339. <https://doi.org/10.1016/j.ast.2019.03.031>
- Martin-Neira, M., M. Paquay, Kudriashov, V., de Wilde, D., & Perdigues-Armengol, J. (2020). Spacecraft Configuration for EHI.
- Mata-Calvo, R., Poliak, J., Surof, J., & Wolf, R. (2020). Evaluation of optical ranging and frequency transfer for the Kepler system: preliminary laboratory tests. *2020 European Navigation Conference (ENC)*, 1–9. <https://doi.org/10.23919/ENC48637.2020.9317374>
- Michalak, G., Glaser, S., Neumayer, K., & König, R. (2021). Precise orbit and Earth parameter determination supported by LEO satellites, inter-satellite links and synchronized clocks of a future GNSS. *Advances in Space Research*, 68(12), 4753–4782. <https://doi.org/10.1016/j.asr.2021.03.008>
- Michalak, G., Neumayer, K. H., & König, R. (2020). Precise Orbit Determination of the Kepler Navigation System - a Simulation Study. *2020 European Navigation Conference (ENC)*, 1–10. <https://doi.org/10.23919/ENC48637.2020.9317467>
- Montenbruck, O., Hackel, S., & Jäggi, A. (2018). Precise orbit determination of the Sentinel-3A altimetry satellite using ambiguity-fixed GPS carrier phase observations. *Journal of Geodesy*, 92, 711–726. <https://doi.org/10.1007/s00190-017-1090-2>
- Montenbruck, O., S., H., Wermuth, M., & Zangerl, F. (2021). Sentinel-6A precise orbit determination using a combined GPS/Galileo receiver. *Journal of Geodesy*, 95(109). <https://doi.org/10.1016/j.asr.2018.04.005>
- Montenbruck, O., Wermuth, M., & Kahle, R. (2011). GPS Based Relative Navigation for the TanDEM-X Mission - First Flight Results. *Journal of the Institute of Navigation*, 58, 293–304. <https://doi.org/10.1002/j.2161-4296.2011.tb02587.x>
- Montenbruck, O., & Gill, E. (2000). *Satellite Orbits: Models, Methods and Applications*. Springer. <https://doi.org/10.1007/978-3-642-58351-3>
- NASA/JPL. (n.d.). Artist's concept of Gravity Recovery and Climate Experiment [Online; accessed February 20, 2023]. [https://www.nasa.gov/mission\\_pages/Grace/multimedia/gallery-index.html#lowerAccordion-set1-slide6](https://www.nasa.gov/mission_pages/Grace/multimedia/gallery-index.html#lowerAccordion-set1-slide6)
- Olsen, N., Haagmans, R., Sabaka, T., Kuvshinov, A., Maus, S., Purucker, M., Rother, M., Lesur, V., & Manda, M. (2006). The Swarm End-to-End mission simulator study: A demonstration of sep-

- arating the various contributions to Earth's magnetic field using synthetic data. *Earth Planets and Space*, 58, 359–370. <https://doi.org/10.1186/BF03351934>
- Olynik, M., Petovello, M., Cannon, M., & Lachapelle, G. (2002). Temporal impact of selected GPS errors on point positioning. *GPS Solutions*, 6, 47–57. <https://doi.org/10.1007/s10291-002-0011-9>
- Pan, L., Zhang, Z., Yu, W., & Dai, W. (2021). Intersystem Bias in GPS, GLONASS, Galileo, BDS-3, and BDS-2 Integrated SPP: Characteristics and Performance Enhancement as a Priori Constraints. *Remote Sensing*, 13(22). <https://doi.org/10.3390/rs13224650>
- Perello-Gisbert, J., & Garcia, A. (2010). *Global Navigation Satellite Systems navigation on the Moon* (tech. rep. TEC-ETN/2010.110/JVPG). European Space Agency.
- Petit, G., & Luzum, B. (2010). *IERS Conventions (2010)* (tech. rep. IERS Technical Note No. 36). IERS.
- Petovello, M., O'Keefe, K., Lachapelle, G., & Cannon, M. (2009). Consideration of time-correlated errors in a Kalman filter applicable to GNSS. *Journal of Geodesy*, 83, 52–56. <https://doi.org/10.1007/s00190-008-0231-z>
- Poncet, D., Glynn, S., & Heine, F. (2017). Hosting the first EDRS payload. *International Conference on Space Optics — ICSSO 2014*. <https://doi.org/10.1117/12.2304091>
- Prange, L., Orliac, E., Dach, R., Arnold, D., Beutler, G., Schaer, S., & Jäggi, A. (2017). CODE's five-system orbit and clock solution—the challenges of multi-GNSS data analysis. *Journal of Geodesy*, 91, 345–360. <https://doi.org/10.1007/s00190-016-0968-8>
- Prange, L., Beutler, G., Dach, R., Arnold, D., Schaer, S., & Jäggi, A. (2020). An empirical solar radiation pressure model for satellites moving in the orbit-normal mode. *Advances in Space Research*, 65(1), 235–250. <https://doi.org/10.1016/j.asr.2019.07.031>
- Racca, G., & McNamara, P. (2010). The LISA Pathfinder Mission: Tracing Einstein's Geodesics in Space. *Space Science Reviews*, 151, 159–181. <https://doi.org/10.1007/s11214-009-9602-x>
- Ripoll, A. (2017). *GNSSSIM Software Report* (tech. rep. GMV-GNSSSIM-SWR-001). GMV.
- Rodriguez-Solano, C., Hugentobler, U., & Steigenberger, P. (2012). Adjustable box-wing model for solar radiation pressure impacting GPS satellites. *Advances in Space Research*, 49(7), 1113–1128. <https://doi.org/10.1016/j.asr.2012.01.016>
- Sanz-Subirana, J., Juan-Zornoza, J., & Hernández-Pajarez, M. (2013). *GNSS Data processing. Volume I: Fundamentals and Algorithms*. ESA Communications.
- Schaer, S., Villiger, A., Arnold, D., Dach, R., Prange, L., & Jäggi, A. (2021). The CODE ambiguity-fixed clock and phase bias analysis products: generation, properties, and performance. *Journal of Geodesy*, 95(81). <https://doi.org/10.1007/s00190-021-01521-9>
- Schlicht, A., Marz, S., Stetter, M., Hugentobler, U., & Schäfer, W. (2020). Galileo POD using optical inter-satellite links: A simulation study. *Advances in Space Research*, 66(7), 1558–1570. <https://doi.org/10.1016/j.asr.2020.06.028>
- Senior, K., Ray, J., & Beard, R. (2008). Characterization of periodic variations in the GPS satellite clocks. *GPS Solutions*, 12, 211–225. <https://doi.org/10.1007/s10291-008-0089-9>
- Sheard, B., Heinzl, G., Danzmann, K., Shaddock, D., Klipstein, W., & Folkner, W. (2012). Intersatellite laser ranging instrument for the GRACE follow-on mission. *Journal of Geodesy*, 86, 1083–1095. <https://doi.org/10.1007/s00190-012-0566-3>
- Sosnica, K., Thaller, D., Dach, R., Steigenberger, P., Beutler, G., Arnold, D., & Jäggi, A. (2015). Satellite laser ranging to GPS and GLONASS. *Journal of Geodesy*, 89, 725–742. <https://doi.org/10.1007/s00190-015-0810-8>
- Sun, R., Guo, J., Maessen, D., & Gill, E. (2010). Enabling inter-satellite communication and ranging for small satellites. *Proceedings of the 4S Symposium: Small Satellites, Systems and Services*, 1–15. <https://research.tudelft.nl/en/publications/enabling-inter-satellite-communication-and-ranging-for-small-sate>
- Tang, C., Hu, X., Zhou, S., Liu, L., Pan, J., Chen, L., Guo, L., R. anf Zhu, Hu, G., Li, X., He, F., & Chang, Z. (2018). Initial results of centralized autonomous orbit determination of the new-generation BDS satellites with inter-satellite link measurement. *Journal of Geodesy*, 92, 1155–1169. <https://doi.org/10.1007/s00190-018-1113-7>
- Tapley, B., Schutz, B., & Born, G. (2004). *Statistical Orbit Determination*. Elsevier Inc. <https://doi.org/10.1016/B978-0-12-683630-1.X5019-X>
- Teunissen, P., & Montenbruck, O. (2017). *Springer Handbook of Global Navigation Satellite Systems*. Springer.

- United Nations. (2021). *The Interoperable Global Navigation Satellite Systems Space Service Volume*. [https://www.unoosa.org/res/oosadoc/data/documents/2021/stspace/stspace75rev\\_1\\_0\\_html/st\\_space\\_75rev01E.pdf](https://www.unoosa.org/res/oosadoc/data/documents/2021/stspace/stspace75rev_1_0_html/st_space_75rev01E.pdf)
- Urschl, C., Beutler, G., Gurtner, W., Hugentobler, U., & Schaer, S. (2007). Contribution of SLR tracking data to GNSS orbit determination. *Advances in Space Research*, 39(10), 1515–1523. <https://doi.org/10.1016/j.asr.2007.01.038>
- Vallado, D. (2001). *Fundamentals of Astrodynamics and Applications*. Springer.
- Wakker, K. (2015). *Fundamentals of Astrodynamics*. TU Delft Library. <http://resolver.tudelft.nl/uuid:3fc91471-8e47-4215-af43-718740e6694e>
- Wanner, G. (2019). Space-based gravitational wave detection and how LISA Pathfinder successfully paved the way. *Nature Physics*, 15, 200–202. <https://doi.org/10.1038/s41567-019-0462-3>
- Wu, S. C., Yunck, T. P., & Thornton, C. L. (1991). Reduced-dynamic technique for precise orbit determination of low earth satellites. *Journal of Guidance, Control, and Dynamics*, 14, 24–30. <https://doi.org/10.2514/3.20600>
- Wuchenich, D., Mahrtdt, C., Sheard, B., Francis, S., Spero, R., Miller, J., Mow-Lowry, C., Ward, R., Klipstein, W., Heinzel, G., Danzmann, K., McClelland, D., & Shaddock, D. (2014). Laser link acquisition demonstration for the GRACE Follow-On mission. *Optics Express*, 22. <https://doi.org/10.1364/OE.22.011351>
- Xiaochun, L. (2022). BeiDou Navigation Satellite System Application Cases Sharing. *Proceedings of UN 65th Committee on the Peaceful Uses of Outer Space*.
- Yang, Y., Yang, Y., Hu, X., Chen, J., Guo, R., Tang, C., Zhou, S., Zhao, L., & Xu, J. (2020). Inter-Satellite Link Enhanced Orbit Determination for BeiDou-3. *The Journal of Navigation*, 73, 115–130. <https://doi.org/10.1017/S0373463319000523>
- Yang, Y., Yong, L., Rizos, C., Dempster, A., & Yue, X. (2014). Inter-satellite Ranging Augmented GPS Relative Navigation for Satellite Formation Flying. *The Journal of Navigation*, 67, 437–449. <https://doi.org/10.1017/S0373463313000763>
- Zackrisson, J., & Öhgren, M. (2011). GNSS Receive Antennas on Satellites for Precision Orbit Determination. *Small Satellite Conference*.
- Zangerl, F. (2017). *PODRIX: Performance Analysis* (tech. rep. P-11284-ANA-0022-RSA). RUAG Space.
- Zech, H., Heine, F., Tröndle, D., Seel, S., Motzigemba, M., Meyer, R., & Philipp-May, S. (2015). LCT for EDRS: LEO to GEO optical communications at 1,8 Gbps between Alphasat and Sentinel 1a. *Unmanned/Unattended Sensors and Sensor Networks XI; and Advanced Free-Space Optical Communication Techniques and Applications*. <https://doi.org/10.1117/12.2196273>
- Zhang, K., Li, X., Wu, J., Yuan, Y., Li, X., Zhang, X., & Zhang, W. (2021). Precise Orbit Determination for LEO Satellites With Ambiguity Resolution: Improvement and Comparison. *Journal of Geophysical Research: Solid Earth*, 126(9). <https://doi.org/10.1029/2021JB022491>
- Zhao, Q., Guo, J., Wang, C., Lyu, Y., Xu, X., Yang, C., & Li, J. (2022). Precise orbit determination for BDS satellites. *Satellite Navigation*, 3. <https://doi.org/10.1186/s43020-021-00062-y>
- Zhu, J., Li, H., Li, J., Ruan, R., & Zhai, M. (2022). Performance of dual one-way measurements and precise orbit determination for BDS via inter-satellite link. *Open Astronomy*, 31, 276–286. <https://doi.org/10.1515/astro-2022-0034>

# A

## Least Squares Algorithm

The least-squares algorithm is a widely used approach in orbit determination that aims to find the trajectory and model parameters that minimize the difference between the modeled observations and actual measurements. Specifically, it seeks to minimize the sum of squares of the observation residuals. In this appendix, the mathematical formulation presented by Montenbruck and Gill (2000) will be followed to derive the least-squares solution.

The set of parameters to be estimated, denoted as  $\mathbf{y}$ , includes the initial position and velocity of the satellite, as well as parameters that influence the dynamical (e.g., drag coefficients) and observation model (e.g., clock biases). These additional parameters are typically denoted as  $p$ .

$$\mathbf{y} = \begin{bmatrix} \mathbf{x}_0 \\ \mathbf{p} \end{bmatrix} \quad (\text{A.1})$$

The evolution of the  $m$ -dimensional vector  $\mathbf{y}$  with respect to time can be described by an ordinary differential equation with initial value  $\mathbf{y}(t_0) = \mathbf{y}_0$  and expressed in the following form:

$$\dot{\mathbf{y}} = \mathbf{f}(t, \mathbf{y}) \quad (\text{A.2})$$

Additionally,  $\mathbf{z}$  denotes the  $n$ -dimensional vector that contains the measured observations.

$$\mathbf{z} = \begin{bmatrix} z_1 \\ \vdots \\ z_n \end{bmatrix} \quad (\text{A.3})$$

These observations are described by the observation equation

$$\mathbf{z} = \mathbf{h}(\mathbf{y}_0) + \boldsymbol{\epsilon} \quad (\text{A.4})$$

where  $\mathbf{h}$  represents the model value of the observations as a function of the state  $\mathbf{y}_0$  at the reference epoch  $t_0$ , and  $\boldsymbol{\epsilon}$  are the difference between the actual and modeled observations, i.e. the residuals.

Therefore, the least-squares problem can be redefined as finding the state  $\mathbf{y}_0^{lsq}$  that minimizes the loss function  $J$ :

$$J(\mathbf{y}_0) = \boldsymbol{\epsilon}^T \boldsymbol{\epsilon} = (\mathbf{z} - \mathbf{h}(\mathbf{y}_0))^T (\mathbf{z} - \mathbf{h}(\mathbf{y}_0)) \quad (\text{A.5})$$

### A.1. Linearization

A key challenge in least-squares orbit determination is that the function  $\mathbf{h}$  is highly non-linear, which can be seen from the observation models discussed in Chapters 2 and 3. As a result, to solve the least-squares problem, it is necessary to linearize the observation equation. The solution will be an approximate value of the non-linear solution.

Linearizing Equation A.4 around a reference state  $\mathbf{y}_0^{ref}$ , which is initially guessed as  $\mathbf{y}_0^{apr}$ , the residual vector can now be expressed as:

$$\boldsymbol{\epsilon} = \mathbf{z} - \mathbf{h}(\mathbf{y}_0) \approx \mathbf{z} - \mathbf{h}(\mathbf{y}_0^{ref}) - \frac{\partial \mathbf{h}}{\partial \mathbf{y}_0} (\mathbf{y}_0 - \mathbf{y}_0^{ref}) = \Delta \mathbf{z} - \mathbf{H} \Delta \mathbf{y}_0 \quad (\text{A.6})$$

where  $\Delta \mathbf{z}$  is the difference between the actual observations and the observations predicted by the dynamical model,  $\Delta \mathbf{y}_0$  is the difference between  $\mathbf{y}_0$  and the reference state, and  $\mathbf{H}$  is the Jacobian. The next subsection gives more information on how to compute the Jacobian matrix.

The loss function of the linear least-squares problem is:

$$J(\Delta \mathbf{y}_0) = (\Delta \mathbf{z} - \mathbf{H} \Delta \mathbf{y}_0)^T (\Delta \mathbf{z} - \mathbf{H} \Delta \mathbf{y}_0) \quad (\text{A.7})$$

The minimum of the loss function is determined by the condition  $\partial J / \partial \Delta \mathbf{x}_0 = \mathbf{0}$ . In this way, the solution to the linear least-squares problem can be written as:

$$\Delta \mathbf{y}_0^{lsq} = (\mathbf{H}^T \mathbf{H})^{-1} (\mathbf{H}^T \Delta \mathbf{z}) \quad (\text{A.8})$$

It is important to remark that the matrix  $\mathbf{H}^T \mathbf{H}$  is the so-called normal equations matrix.

The solution obtained from the simplified linear loss method differs slightly from the non-linear solution, and thus the value of  $\mathbf{y}_0^{lsq}$  is not the exact solution of the orbit determination problem. However, this limitation can be addressed by employing an iterative approach. In this approach, the computed  $\mathbf{y}_0^{lsq}$  is used as the reference value  $\mathbf{y}_0^{ref}$  for the next iteration. This iterative procedure is repeated until the relative change in the loss function between two successive iterations falls below a certain threshold.

## A.2. Decomposition of the Jacobian

The computation of the Jacobian matrix  $\mathbf{H}$  involves the computation of three matrices: the partial design matrix  $\mathbf{A}$ , the state transition matrix  $\phi$ , and the sensitivity matrix  $\mathbf{S}$ .

$$\mathbf{H} = \frac{\partial \mathbf{h}}{\partial \mathbf{y}_0} = \frac{\partial \mathbf{h}}{\partial \mathbf{x}} \frac{\partial \mathbf{x}}{\partial \mathbf{y}_0} = \frac{\partial \mathbf{h}}{\partial \mathbf{x}} \begin{bmatrix} \frac{\partial \mathbf{x}}{\partial x_0} & \frac{\partial \mathbf{x}}{\partial \mathbf{p}} \end{bmatrix} = \mathbf{A} [\phi, \mathbf{S}] \quad (\text{A.9})$$

Matrix  $\mathbf{A}$  contains the partials of the modeled observations with respect to the position and velocity, and it can be expanded as:

$$\mathbf{A} = \frac{\partial \mathbf{h}}{\partial \mathbf{x}} = \begin{bmatrix} \frac{x - x_s}{R} & \frac{y - y_s}{R} & \frac{z - z_s}{R} & 0 & 0 & 0 \end{bmatrix} \quad (\text{A.10})$$

where  $x$ ,  $y$  and  $z$  are the coordinates of the receiver satellite and  $x_s$ ,  $y_s$  and  $z_s$  the coordinates of the GNSS satellite.

The state transition matrix  $\phi$  is computed as the partial derivatives of the position and velocity at a specific epoch with respect to the initial position and velocity.

$$\phi = \frac{\partial \mathbf{x}}{\partial \mathbf{x}_0} = \begin{bmatrix} \frac{\partial \mathbf{r}}{\partial \mathbf{r}_0} & \frac{\partial \mathbf{r}}{\partial \mathbf{v}_0} \\ \frac{\partial \mathbf{v}}{\partial \mathbf{r}_0} & \frac{\partial \mathbf{v}}{\partial \mathbf{v}_0} \end{bmatrix} \quad (\text{A.11})$$

This matrix  $\phi$  is obtained by numerically solving the following first-order differential equation:

$$\dot{\phi} = \frac{\partial \mathbf{f}}{\partial \mathbf{x}} \phi \quad (\text{A.12})$$

In this expression, the right-hand side term can be further expanded as:

$$\frac{\partial \mathbf{f}}{\partial \mathbf{x}} = \begin{bmatrix} \frac{\partial \mathbf{v}}{\partial \mathbf{r}} & \frac{\partial \mathbf{v}}{\partial \mathbf{v}} \\ \frac{\partial \mathbf{r}}{\partial \mathbf{a}} & \frac{\partial \mathbf{r}}{\partial \mathbf{v}} \end{bmatrix} = \begin{bmatrix} \mathbf{0}_{3 \times 3} & \mathbf{I}_{3 \times 3} \\ \frac{\partial \mathbf{a}}{\partial \mathbf{r}} & \frac{\partial \mathbf{a}}{\partial \mathbf{v}} \end{bmatrix} \quad (\text{A.13})$$

where  $\mathbf{0}_{3 \times 3}$  is the  $3 \times 3$  zero matrix,  $\mathbf{I}_{3 \times 3}$  the  $3 \times 3$  identity matrix, and  $\mathbf{a}$  is the total acceleration of the satellite.

Finally, the sensitivity matrix  $\mathbf{S}$  is composed of the partial derivatives of the position and velocity with respect to the model parameters. For  $k$  parameters,  $\mathbf{S}$  may be expressed as:

$$\mathbf{S} = \frac{\partial \mathbf{x}}{\partial \mathbf{p}} = \begin{bmatrix} \frac{\partial \mathbf{x}}{\partial p_1} \\ \vdots \\ \frac{\partial \mathbf{x}}{\partial p_k} \end{bmatrix} \quad (\text{A.14})$$

Similar to the state transition matrix,  $S$  is computed by numerically solving a first-order differential equation that involves the partial derivatives of acceleration with respect to position and velocity, as well as the partial derivatives of acceleration with respect to the model parameters.

$$\dot{S} = \frac{\partial f}{\partial x} S + \frac{\partial f}{\partial p} \quad (\text{A.15})$$

### A.3. Weighting

The least-square algorithm discussed earlier assumes that all observations in the vector  $z$  have equal importance in the solution, regardless of the type and quality of the measurement. However, in practice, different observations may have different units or levels of accuracy. As a result, it is often necessary to apply a weighting factor to each observation that reflects its relative importance.

In general, each observation is weighted with the inverse of its mean measurement error  $\sigma_i$ , such that observations with smaller errors are given higher weight than those with larger errors.

$$W = \begin{bmatrix} \sigma_1^{-2} & & 0 \\ & \ddots & \\ 0 & & \sigma_n^{-2} \end{bmatrix} \quad (\text{A.16})$$

The solution to the weighted least-squares problem can be expressed as follows:

$$\Delta y_0^{lsq} = (H^T W H)^{-1} (H^T W \Delta z) \quad (\text{A.17})$$

### A.4. A priori Information

An initial guess of the state vector  $y_0^{apr}$  is required to start the least-squares orbit determination process. In general, some information about the accuracy of this state vector is available, which can be quantified by the a priori covariance matrix  $P_0^{apr}$ . The matrix  $P_0^{apr}$  is a  $m \times m$  symmetric matrix, where  $\sigma_{ii}^2$  represents the a priori variance of parameter  $i$  and  $\sigma_{ij}^2$  represents the a priori covariance between parameters  $i$  and  $j$ .

$$P_0^{apr} = \begin{bmatrix} \sigma_{11}^2 & \sigma_{12}^2 & \cdots & \sigma_{1m}^2 \\ \sigma_{21}^2 & \sigma_{22}^2 & \cdots & \sigma_{2m}^2 \\ \vdots & \vdots & \ddots & \vdots \\ \sigma_{n1}^2 & \sigma_{n2}^2 & \cdots & \sigma_{nm}^2 \end{bmatrix} \quad (\text{A.18})$$

Incorporating this information into the least-squares algorithm formulation results in a redefinition of the weighted least-squares solution, given by the following equation:

$$\Delta y_0^{lsq} = (\Lambda + H^T W H)^{-1} (\Lambda \Delta y_0^{apr} + H^T W \Delta z) \quad (\text{A.19})$$

where  $\Lambda$  is the information matrix, defined as the inverse of the a priori covariance matrix  $\Lambda = (P_0^{apr})^{-1}$ .